Commissioning of Silicon Detectors for the COMPASS Experiment at CERN

Robert Marcus Wagner
Diplomarbeit

December 2001

Physik-Department E18
Technische Universität München

TECHNISCHE
UNIVERSITÄT
MÜNCHEN

Contents

List of Figures

Chapter 1

Introduction

"Non sunt multiplicanda entia praeter necessitatem."
(William of Ockham)

A great amount of understanding of the fundamental forces has been gained over the last thirty years. Still, many fundamental questions, in particular concerning mesonic and baryonic structure and decays remain unanswered, owing to the special properties of strong interaction and QCD.

A promising approach for obtaining a more detailed insight into hadron physics is the observation of leptonic and semi-leptonic charm hadron decays. They provide clean final state channels and take place at a scale where theoretical predictions of QCD are already possible and at which effects are still big enough to be observed more easily than in beauty physics. Measurements can be done by observing the decay of charmed mesons, like D_s^+ or D^+. Such mesons have short lifetimes of the order of 10^{-12} sec and travel only about $c\tau = 150$ μm before decaying.

To precisely determine decay kinematics of such mesons with sufficiently high statistics, detectors with high spatial resolution have to be used in high-intensity hadron beams, as planned in COMPASS a fixed target experiment at CERN. Such high-intensity experiments set new requirements in many fields, for example the amount of collected data, development of readout electronics, and radiation hardness of detectors.

In COMPASS, Silicon microstrip detectors will be used for beam definition, as charm decay detectors in the target region, and as tracking detectors in the very beam vicinity in the spectrometer. To enable the detectors to stand hadron beam intensities as high as those planned in COMPASS, they will be operated at Nitrogen temperature to exploit the Lazarus effect.

After an overview of the physics objectives and the experimental apparatus of COMPASS in chapter 2, the main features of Silicon microstrip detectors are discussed in chapter 3. Mechanisms of radiation damages and the principles of the Lazarus effect, which allows to operate detectors in high-radiation environment, are described.

Chapter 4 is dedicated to the specific realization of Silicon microstrip detectors in the COMPASS experiment, including a survey of the detector design and the readout electronics. Production and tests done in the lab with a software developed within the framework of this thesis are discussed in chapter 5. Here, emphasis is placed on the noise performance of the detectors. In chapter 6, the analysis of readout and performance tests in the T11 test beam at CERN in March 2001 is presented. Finally commissioning, debugging and first tests of the detectors and of the readout system on the COMPASS beam line from August to October 2001 are presented in chapter 7.

Chapter 2

The COMPASS experiment

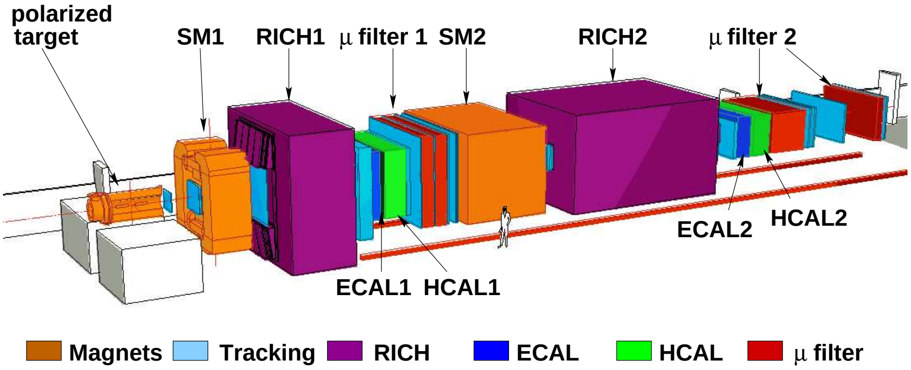

Figure 2.1: Artist's view of the COMPASS spectrometer

COMPASS[1] is a high-luminosity fixed target experiment at the CERN[2] Super Proton Synchrotron (SPS). With the help of a conversion target, muons with energies up to 190 GeV and pions, kaons and protons with energies up to 300 GeV are used to elucidate a variety of physics in the mid to high energy range [CO96]. COMPASS started taking data in 2001.

Being a merger of the HMC[3] and CHEOPS[4] projects, COMPASS is designed to be a multipurpose experiment which can investigate spin structure functions as well as study many properties of hadronic systems. Main issues of the two physics programs, the muon and the hadron program, are summarized in this chapter. A brief overview of the detector itself is given. The COMPASS tracking detectors as well as the setup in the target region are discussed in detail.

---

[1] **Co**mmon **M**uon and **P**roton **A**pparatus for **S**tructure and **S**pectroscopy

[2] Conseil **E**uropéenne pour la **R**echerche **N**ucléaire

[3] **H**adron **M**uon **C**ollaboration [Nap95]

[4] **Ch**arm **E**xperiment with **O**mni-**P**urpose **S**etup [Ale95]

2.1 COMPASS physics

2.1.1 Muon program

Gluon polarization $\Delta G/G$. As results from EMC [Ash88, Ell88] and SMC [Ada97] as well as from experiments at SLAC [Ant96] and DESY [Air98] have shown, a substantial amount of the spin content of the nucleon is not carried by the quark spins as the Ellis-Jaffe sum rule suggests [Tho01]. In the gluon interpretation polarized glue ΔG lowers the quarks' contribution to the total spin. As a major goal, COMPASS aims at a direct measurement of the gluon helicity distribution $\Delta G(x)$ by using deep inelastic scattering of a polarized muon beam of 100–190 GeV off a polarized target.

A study of the cross section asymmetry for open charm leptoproduction [Glu88] is considered the best option for experiments with a muon beam. In leading order, open charm will be produced in the photon-gluon fusion (PGF) process shown in fig. 2.2.A main tool to reconstruct open charm events is the identification of D^0 mesons from their hadronic decay products. The background of charmed hadrons produced in other reactions is expected to be low as the charm quark mass is rather large.

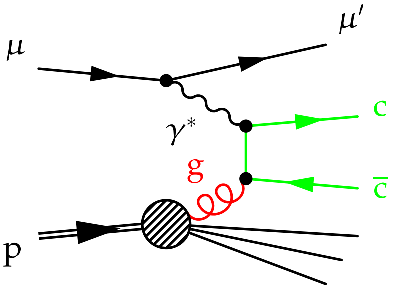

Figure 2.2: Photon-gluon fusion. The incident muon interacts with a gluon in the nucleon through the exchange of a virtual photon.

Additional determination of $\Delta G/G$. The most promising additional way to measure ΔG in COMPASS uses its capability of identifying all particles produced in muon-nucleon scattering. Here, the asymmetry of oppositely charged hadron pairs in high p_t particle production events in deep-inelastic scattering is measured [Bra98]. The basic diagram still is PGF, the hardness of the process is guaranteed by the large p_t. Developed for COMPASS, this method has recently been applied to HERMES data [Air00].

Lambda polarization. Another possible contribution to the spin of the nucleon is the existence of negatively polarized strange quarks. Measuring the polarization of $\Lambda/\overline{\Lambda}$ hyperons from the target fragmentation, one gets a handle on complementary information on the polarization of the strange sea-quarks. Using a polarized beam in combination with an unpolarized target, reactions with quarks oriented anti-parallel to the virtual photon's helicity can be selected. One should expect Λs carrying negative polarization, hence the spin of the strange quarks should be predominantly oriented anti-parallel to that of the proton (assuming negatively polarized muons).

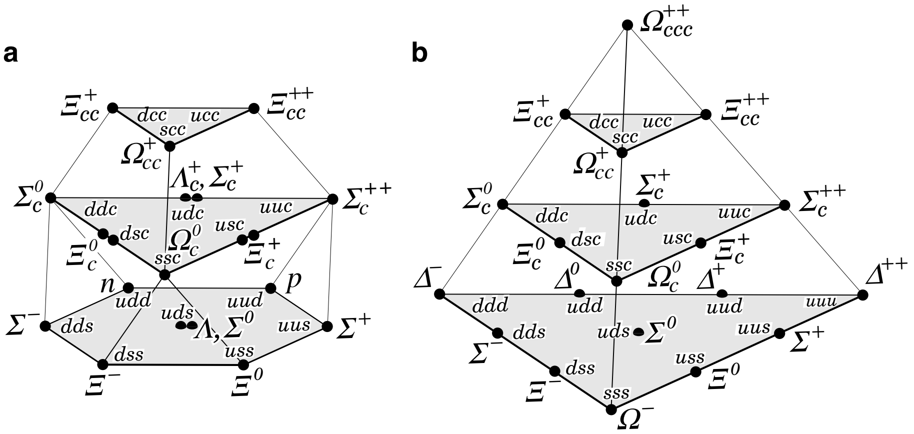

Figure 2.3: SU(4) representation of the ground state baryons. a) $J = 1/2$, b) $J = 3/2$ [PDG00]

After one year of running at 160 GeV/c, COMPASS should be able to obtain $\Delta G/G$ within an error of 0.11 for the open charm program and within 0.05 by using high p_t methods, with higher systematic errors from model interpretations in case of high p_t hadrons.

Longitudinal and transverse spin distribution functions. Apart from ΔG, COMPASS will measure helicity distributions Δq and transverse spin distribution functions $\Delta_\mathrm{t} q$ from the relevant identified hadron asymmetries, in semi-inclusive double-polarized muon-nucleon deep inelastic scattering.

2.1.2 Hadron program

Charm physics. Charm physics in general is interesting, as it allows to study the influence of strong interactions on the weak decay of hadrons at a scale where QCD predictions are already possible, unlike in the light quark sector [Sch99, Ric95]. In addition, still little is known about the properties of charmed baryons. Not even all $1/2^+$ ground states (fig. 2.3) have been observed: $\Xi_\mathrm{c}^{0\prime}$ and the $\Xi_\mathrm{c}^{+\prime}$ of the SU(4) anti-quartet still need confirmation [PDG00]; of the $3/2^+$ baryons, up to now only Ξ_c^{0*} has been observed.

To get a handle on charmed baryons, semi-leptonic decays of charmed hadrons will be studied. Knowledge of their decay widths proves to be the best test of our understanding of charmed baryon decays, since precise theoretical predictions are available within the framework of Heavy Quark Effective Theory (HQET). Transitions like $\Sigma_\mathrm{c}^0 \to \Lambda_\mathrm{c}^+$ can be used for tagging and thus for background reduction.

Furthermore, investigation of the lifetimes of charmed baryons helps to understand the effects of the hadronic environment on the decay of the naked charm quark; non-leptonic decays will be studied to obtain and compare decay rates of these decays. Up to now, only (and still incompatible) data on the Λ_c^+ exist.

Apart from charmed baryons, leptonic decays of the charmed D and D_s mesons will be studied. Their decay constants F_D and F_{D_s} contain all non-perturbative aspects of charm decays. By accessing them with charm decays, QCD effects are limited to the initial state, as in the final state only leptons are observed [Ric95]. Tagging the D-mesons in processes like $D_s^{+*} \to D_s^+\gamma$ or $D^{+*} \to D^+\pi^0$ facilitates background reduction. COMPASS is able to pin down F_{D_s} and F_D to statistical errors of ±10% and ±20%, respectively, within one year of running.

As so far no studies on doubly-charmed baryons have been done, this is one of the issues of the hadron program: Such baryons may reveal a heavy cc-diquark in the center surrounded by a third light quark, bearing dynamics similar to heavy mesons. Such states are expected in a mass range from 3.6 GeV/c^2 (ccu, ccd) to 3.8 GeV/c^2 (ccs). Despite COMPASS being a high-rate experiment, only about $30 - 300$ fully reconstructed events are expected, because production cross sections and branching ratios are very low.

Exotics and gluonic systems. Since gluons carry color charge, the construction of bound states with valence gluons or consisting only of gluons is predicted within QCD. If consisting of gluons only, those states are called *glueballs*, if they consist of valence quarks and valence gluons, we speak of *hybrids*. To provide a gluon-rich environment, COMPASS will use the double pomeron exchange mechanism [Mey98, God99] in central collisions of a proton beam on a proton target.

The identification of e. g. glueballs is challenging. Since they are expected in a wide mass region starting at 1.5–1.8 GeV, there are many meson resonances which mix with glueballs with identical quantum numbers. The so far best candidate for a scalar glueball ground state 0^{++} comes from the Crystal Barrel experiment at LEAR, the $f_0(1500)$ [Ams95]. High statistics as well as a good understanding of glueball production mechanisms and decay patterns are necessary to clearly identify glueballs. COMPASS will be able to detect many decay modes and several different production mechanisms. The $f_0(1500)$ will be investigated, and a systematic scan of the mass region up to 2.5 GeVwill be done, in which e. g. the first excited state, the tensor glueball 2^{++}, is predicted around 2.3 GeV by lattice QCD [Sch99, Bra99].

Another issue is the search for charmed exotics, i. e. particles not composed of $q\bar{q}$ or qqq quark content. An experiment like COMPASS should have sufficiently high statistics to show $q\bar{q}g$ or five-quark systems like $uud\bar{c}s$ or $udd\bar{c}s$, if only their binding energy is high enough for a bound state.

To cross-check results obtained with central production, the Coulomb excitation process with a high Z target can be used. Glueball candidates should be absent in the final states produced in that process.

Primakoff scattering reactions. To study mesonic structure, Compton scattering with virtual photons in inverse kinematics, the *Primakoff mechanism*, is used. In such reactions, a pion scatters off a heavy target nucleus via a quasi-real photon from the electric field of the nucleon, producing a real photon, as illustrated in fig. 2.4. Access to several quantities such as polarizabilities of the pion is gained. Using kaon or sigma beams, similar studies can be performed on these particles as well.

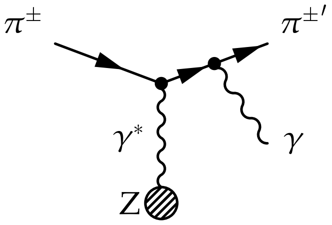

Figure 2.4: The Primakoff mechanism: Compton scattering in inverse kinematics

2.2 The COMPASS detector

2.2.1 The spectrometer

To provide a large angular acceptance of about 180 mrad and a large dynamical range of up to 150 GeV, the global structure of the COMPASS experiment comprises a high-rate, two-stage forward magnetic spectrometer. The two stages use conventional magnets with 1.0 Tm and 5.2 Tm bending power. Each of the two spectrometer stages will be equipped with complete tracking, particle identification, electronic and hadronic calorimeters and muon detection systems in the final setup. For the 2001 run, a reduced setup (fig. 2.5) was used, which is fully adequate to start muon and spin physics [Bra99].

Due to their different angular acceptances, the spectrometer stages cover different momentum regions. The small angle (second stage) spectrometer is to a large extent common for both programs and all experimental configurations, while in the first spectrometer some detector types are used only in the muon and the hadron program, respectively. In addition, the target region is equipped differently for the muon and the hadron program.

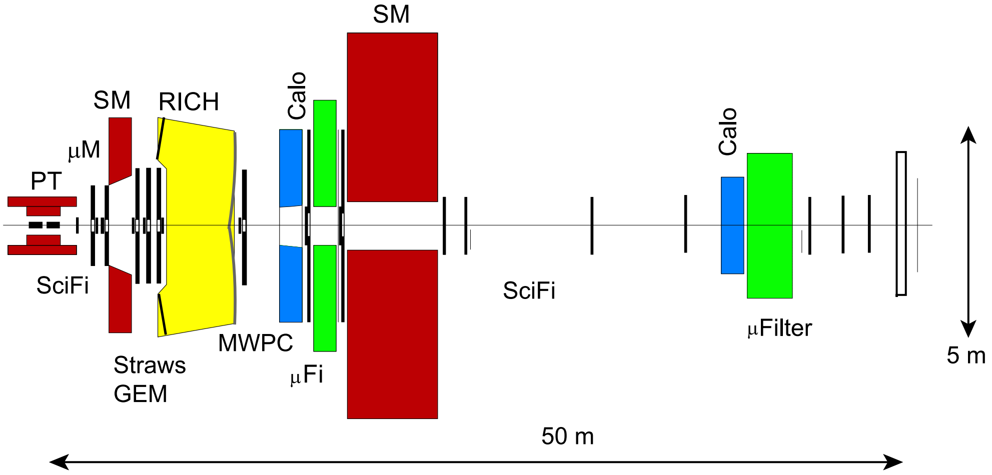

Figure 2.5: The COMPASS spectrometer in its initial setup

Because of the size of the muon target magnet, there is not much space for small angle trackers between the target itself and the first spectrometer magnet (SM1). Therefore, tracking is restricted to two Silicon stations and two stations of scintillating fibers upstream of the target, as well as two Micromega tracking stations in front of SM1. Details of the setup of the target region in the hadron program are discussed later in this chapter.

The tracking stations downstream of the target are composed of different detector systems, which provide good spatial resolution near the beam axis as well as coverage of a large area leading to a large angular acceptance. Tracking detectors are distributed over the whole length of the experiment and are described in more detail in section 2.2.3.

In both stages, a RICH[5] will be used to identify pions, kaons and protons. Presently RICH1, located between SM1 and SM2, is installed and provides particle separation in the momentum range between 3 and 55 GeV/c. RICH2 is planned for later installation and will be located downstream of SM2. It will allow particle separation up to 120 GeV/c and provide additional information in the momentum range from 30 to 65 GeV/c, where in RICH1 the particle identification is challenging.

At the end of each spectrometer stage, both an electronic and a hadronic calorimeter detect the energies of produced hadrons, photons and electrons. A muon wall measures the positions of passing muons. In order to allow particles with higher energy to enter the second spectrometer stage, the calorimetric detectors in the first stage have a hole of $1.4 \times 0.7\,\mathrm{m}^2$.

---

[5] **R**ing **I**maging **Ch**erenkov detector

2.2.2 The target region

Muon program. In general, for measuring spin-dependent quantities, polarized targets have to be used. Two different target materials are needed in order to measure the proton's as well as the neutron's spin structure: NH_3 and ^{6}LiD with maximum polarizations of 85% and 50%, respectively. The material is polarized by dynamical nuclear polarization. For polarizing the muon target, a superconducting solenoidal magnet and a dilution refrigerator are used to reach the necessary low temperatures of the order of mK. As muon target in the 2001 run the existing SMC target magnet is used.

Hadron program. In the hadron program, different target types will be used: For central production of mesons and gluon-rich states, a liquid hydrogen target is needed, whereas to produce charm hadrons, a thin Copper plate will be used. For Primakoff reactions, a thin target with a high Z material is needed [Kuh01].

Trackers in hadron setup. In the hadron setup only a comparatively small solid state target with a recoil detector is present. Therefore, more space for tracking detectors is available between the target and SM1, which will be used for two more Silicon tracking stations (figure 2.6). Furthermore, the gap of SM1 is planned to be reduced in order to get smaller fringe fields. The installation of Silicon microstrip detectors is planned up- and downstream in the vicinity of SM1 as well.

The charm vertex detector. In the hadron setup, a spatial resolution as high as possible is needed to ensure high charm tagging efficiency even for short-lived mesons as well as a highly efficient triggering on secondary vertices.

Downstream of the copper target, trigger detectors as well as a tracking detector similar to that of WA92 [Adi93] will be used, consisting of 10 planes of Silicon

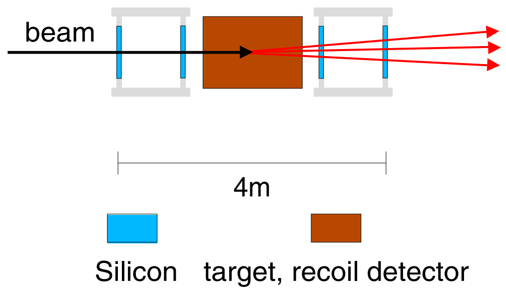

Figure 2.6: Tracking stations in the target region: Two stations in front of the target are used for beam definition. The two stations behind the target will only be present in the hadron setup.

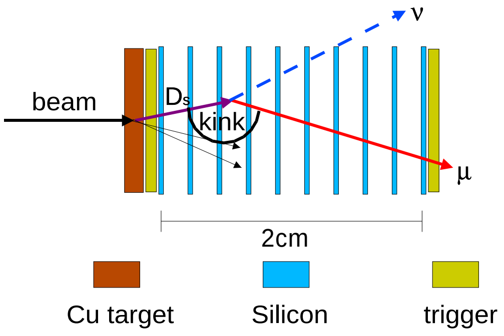

Figure 2.7: The charm vertex detector: Behind the Copper target, 10 planes of Silicon detectors are sandwiched between two trigger detectors. [Sch00]

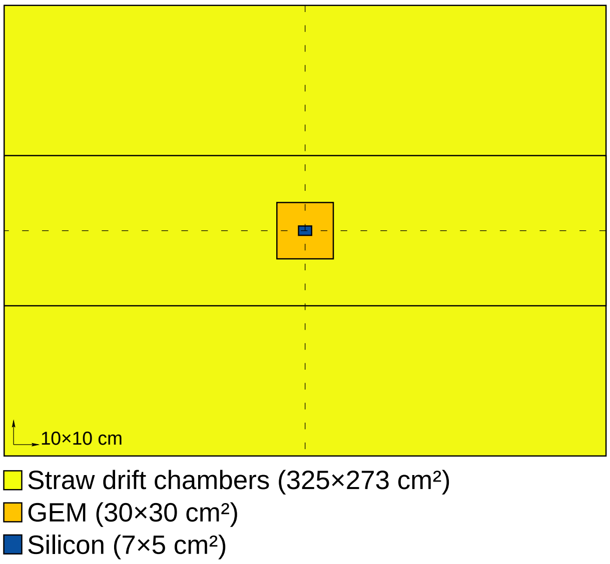

Figure 2.8: Hybrid tracker concept: Sizes and coverage provided by a Straw station as large area tracker and one GEM and one Silicon station for the small area tracking

strip detectors with an extremely fine pitch of 12 µm (fig. 2.7). With a distance of only 2 mm from one detector to the next, this setup will allow to fully reconstruct semi-leptonic and leptonic charm decays, including the charmed particle's track. Hence, complete kinematical reconstruction of the decay is possible [Sch00].

2.2.3 Tracking in the COMPASS spectrometer

In general, in the spectrometer region of COMPASS hybrid tracking stations suitable for both large and small area tracking are used. The detectors operated closer to the beam feature increased precision and radiation hardness. To prevent radiation damage and to withstand the high beam intensities, all tracking detectors except for the Silicon detectors have a deactivated central area. With the staggered tracking concept, the number of events per readout channel is approximately constant. Figure 2.8 shows a typical combination of different detector types.

Straw chambers, drift chambers and well established multi-wire proportional chambers (MWPCs) serve as large-area trackers, while newly-developed Gas Electron Multipliers (GEMs), and Micromegas do the small area tracking. To obtain high precision tracking in the very vicinity of the beam, the central regions of the small area trackers will be covered by Silicon microstrip detectors in the future. Table 2.1 summarizes properties of the different trackers used within COMPASS.

Detector type	Active area	Spatial resolution	Time resolution	Reference
Scintillating fibers (target region)	$52.5 \times 52.5\,\mathrm{mm}^2$	$120\,\mu\mathrm{m}$	430 ps	[Hor99]
Scintillating fibers (spectrometer)	$123 \times 123\,\mathrm{mm}^2$	$410\,\mu\mathrm{m}$	440 ps	[Zie01]
Silicon microstrip detectors	$7 \times 5\,\mathrm{cm}^2$	$< 14\,\mu\mathrm{m}$	5 ns	[Wie00]
Gas electron multipliers	$30 \times 30\,\mathrm{cm}^2$	$46 \pm 3\,\mu\mathrm{m}$	15 ns	[Sim01]
Micromegas	$38 \times 38\,\mathrm{cm}^2$	$70\,\mu\mathrm{m}$	9.5 ns	[Bed01]
Straw drift tubes	$325 \times 273\,\mathrm{cm}^2$	$150\,\mu\mathrm{m}$	(70 ns)	[San99]
Drift chamber	$140 \times 124\,\mathrm{cm}^2$	$175\,\mu\mathrm{m}$	(80 ns)	[Per01]
Multi-wire proportional chamber	$150 \times 120\,\mathrm{cm}^2$	$500\,\mu\mathrm{m}$		[Sau77]

Table 2.1: Tracking detectors in COMPASS

For the central beam region, Silicon detectors provide the best spatial resolution for the detector types given, which is needed for finding tracks with very low inclination with regard to the beam. Another reason for Silicon detectors is that the created electron-hole pairs are drained off the depletion zone in less than 25 ns (cf. section 3.4.1), while detectors using gas amplification have much larger regeneration times.

Upstream of the target, tracking detectors are needed for beam definition. For this, two stations of Silicon microstrip trackers as well as two stations of scintillating fibers are used. Between the target and SM1, scintillating fibers and Micromegas are used for small area tracking, while drift chambers do the large area tracking. The tracking immediately behind SM1 is done with straw trackers for large angles and GEM detectors for small angles, respectively. Downstream of RICH1, tracking stations consist of MWPCs for large angles and GEMs for small angles.

2.2.4 A glance at selected tracking detectors

Silicon microstrip detectors. What we refer to as one station of Silicon detectors consists of two $7 \times 5\,\mathrm{cm}^2$ double-sided Silicon wafers (detectors), mounted 10 mm apart. One of these stations provides four readout planes. The two detectors are rotated by 5° with respect to each other for separating multiple hits. The spatial resolution is better than $14\,\mu\mathrm{m}$ (cf. section 3.4.1) and the time resolution is better than 5 ns.

Scintillating fibers. These detectors provide a spatial resolution of at least $500\,\mu\mathrm{m}$. With a very good time resolution of about 300 ps they are used for precise track timing. Detectors with active areas from $39.4 \times 39.4\,\mathrm{mm}^2$ up to $123 \times 123\,\mathrm{mm}^2$ are distributed over the experimental apparatus, using fiber diameters of 0.5 mm and 1.0 mm.

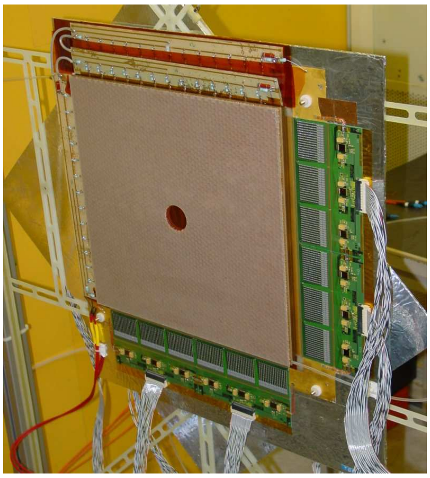

Figure 2.9: GEM detector in the lab

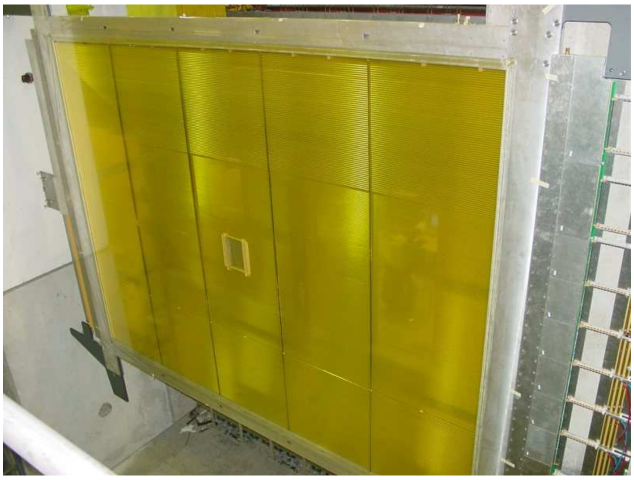

Figure 2.10: Straw drift chamber DL4. Note the central beam hole.

Small area trackers. Gas Electron Multiplier (GEM) and Micromesh Gaseous Detector (Micromegas) stations each consist of two detectors mounted back-to-back. GEMs are made of three copper-clad amplification foils. These foils have a fine perforation of 120 μm pitch to provide electron multiplication due to the high electric field in the holes. GEMs provide a spatial resolution of 46 ± 3 μm and a time resolution of about 15 ns. Details are discussed in [Sim01]. Micromegas utilize a fine metal mesh instead of amplification foils. They reach a spatial resolution of 70 ns and a time resolution of 9.5 ns [The01]. In 2001, the small area tracking is done with 7 stations of 30×30 cm^2 GEM detectors in the spectrometer and 2 Micromega stations covering an area of 38×38 cm^2 each in front of SM1.

Straw chambers. Covering an active area of 273×325 cm^2, Straw chambers (fig. 2.10) are made of copper coated Kapton or mylar tubes with an anode wire in the center. In the middle region, tubes with a diameter of 6 mm are used, in the outer region the tubes have a diameter of 10 mm. Centered around the beam, they have a 20×20 cm^2 beam hole. The straws are arranged in double layers, which are displaced by half a tube diameter with respect to each other. Straws equipped with vertical or horizontal tubes are used to gain different projections within one station. One double layer reaches a spatial resolution of about 150 μm.

Chapter 3

Silicon microstrip detectors

Since J. Kemmer [Kem80] introduced planar technology to produce Silicon detectors in 1980, which made it possible to read out position information with great precision by dividing the detector's surface into fine strips, such devices have become a common tool in particle physics.

This chapter gives a summary on Silicon detectors and their principle of operation. Radiation damage and annealing mechanisms are discussed. Thorough descriptions of double-sided Silicon microstrip detectors and production techniques are given in [Pei92, Kem88].

3.1 Basic principle of operation

In a semiconductor device, a fast charged particle will create electron-hole pairs along its track by Coulomb interaction. The charge carriers created are separated by an electric field applied over the detector and are read out with position-sensitive electrodes along the detector volume.

Unlike in gaseous detectors, there is no multiplication of the primary charge, so that the collected charge is only a function of the detector thickness, yielding about 390 eV/ μm equivalent to about 108 electron-hole pairs per μm for Silicon [Pei92]. The advantage of semiconductor devices is that the average energy required to create an electron-hole pair is some 10 times smaller than that required for gas ionization. The energy required for the production of one electron-hole pair is 3.6 eV [PDG00] in Silicon. This energy is larger than the band gap in Silicon because of momentum conservation. Thus the amount of ionization produced for a given energy is an order of magnitude larger.

Typically, Silicon detectors are required in environments where the amount of material used should be as small as possible to avoid multiple Coulomb scattering and to minimize the impact on the particle tracks. Owing to its high density, a high energy loss can already be obtained with comparatively thin Silicon detectors. Since the detector thickness determines the signal amplitude, the commonly used compromise are detectors of 300 μm thickness, resulting in an average of $3.2{\cdot}10^4$ electron-hole pairs generated per MIP[1], a signal requiring low-noise electronics. Background noise arises from the semiconductor's intrinsic carrier density and from design issues like interstrip and load capacitances.

3.2 Ionization energy loss by heavy particles

3.2.1 The Bethe-Bloch formula

Charged particles other than electrons mainly lose energy in matter by ionization or equivalent processes, like the creation of electron-hole pairs. The *stopping power* or mean rate of energy loss is given by the *Bethe-Bloch formula* [PDG00, Leo87],

$$-\frac{\mathrm{d}E}{\mathrm{d}x} = \kappa\rho\left[\ln\left(\frac{2m_\mathrm{e}\gamma^2 v^2 W_\mathrm{max}}{I^2}\right) - 2\beta^2 - \delta - 2\frac{C}{Z}\right] \tag{3.1}$$

with the material density ρ, the electron mass m_e, the velocity of the incident particles v given in terms of β and γ, the maximum energy transfer in a single collision $W_\mathrm{max} \approx 2m_\mathrm{e}c^2\beta\gamma$ [Gru93],

$$\kappa = 2\pi N_a r_\mathrm{e}^2 m_\mathrm{e} c^2 \frac{Z}{A}\frac{z^2}{\beta^2} = 0.1535\frac{\mathrm{MeV\,cm^2}}{\mathrm{g}}\frac{Z}{A}\frac{z^2}{\beta^2}, \tag{3.2}$$

and charge of the incident particle z, The atomic number and the mass of the detector material is denoted by Z and A, respectively. The mean ionization energy of Silicon is $I = 13.5\ \mathrm{eV}{\cdot}Z$ [Ste84].

This formula holds for relativistic particles with not too high energy. Inelastic scattering of the incident particles off the atomic shells of the detector atoms is assumed, which creates electron-hole pairs along the particles' tracks.

---

[1] **M**inimum **i**onizing **p**article, for definition see section 3.2.1

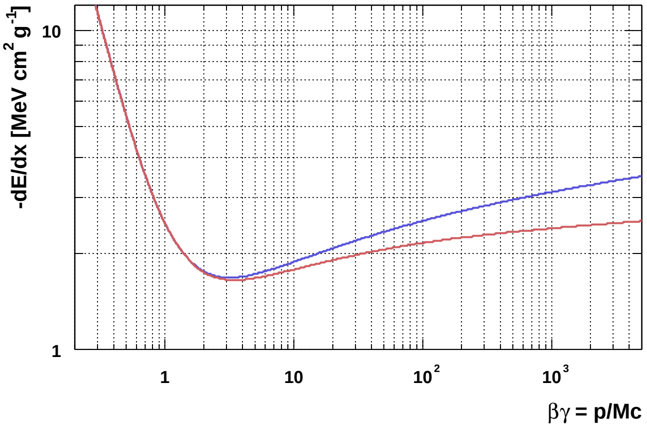

Figure 3.1: Energy loss rate for muons with (red curve) and without (blue curve) density and shell correction applied. The relativistic rise is nearly cancelled by the density correction.

Energy dependence. Figure 3.1 shows a Bethe-Bloch curve. At non-relativistic energies, the energy loss is dependent on the particles' velocity and charge but not on their mass, leading to the characteristic $1/\beta^2$ dependence given in (3.2). A minimum is reached at about $\beta \approx 0.96$. Particles with an energy loss close to this minimum are known as *minimum ionizing particles*, MIPs. Most relativistic particles can be treated as MIPs as well, since from the minimum of the curve on, its *relativistic rise* due to the logarithmic dependence in (3.1) is cancelled by the *density correction* to a good approximation.

In (3.1), two corrections, the *density effect correction* δ and the *shell correction* C, have been added. These corrections cause an 32% effect for muons at 160 GeV beam energy, which corresponds to $\beta\gamma \approx 1500$ and is typical for the particle energies in COMPASS.

Density effect. This effect arises from the fact that the electric field of the particle tends to polarize the atoms along its path. Due to this polarization, electrons far from the path of the particle will be shielded from the full electric field intensity. Collisions with such electrons will therefore contribute less to the total energy loss than predicted by the Bethe-Bloch formula without corrections. Hence, the logarithmic rise of (3.1) will be truncated at high energies. The density correction δ is usually given by Sternheimer's parameterization [Ste84], which involves the material's plasma frequency in its high-energy limit

$$\delta/2 \to \ln(\hbar\omega_P/I) + \ln\beta\gamma - 1/2. \tag{3.3}$$

While negligible when dealing with gases with low densities, this effect has to be taken into account in the case of solid-state materials (fig. 3.1). It also becomes important for higher energies ($\beta\gamma \gtrsim 100$).

Shell correction. C/Z is a low-energy correction that takes atomic binding effects into account, which have partially been neglected in the Bethe-Bloch formula. The original assumption of a stationary electron with respect to the incident particle nevertheless is a rather good one for $\beta\gamma \gtrsim 0.3$, the correction decreasing very rapidly with energy.

3.2.2 Energy loss distribution

Statistical fluctuations. Up to now, we considered the *mean energy loss* of a particle passing the detector. For any given particle, however, we will not find an energy loss equal to this calculated value, because we deal with the number of collisions and the energy loss in every such collision as statistical quantities.

It can be shown that for thick absorbers with a large number of collisions, the energy loss distribution takes a Gaussian form. This follows directly from the central limit theorem [Fli99, Leo87].

Landau distribution. With thin absorbers, where the number of collisions is too small for the central limit theorem to hold, large deviations from the mean energy loss given by (3.1) are observed. The general shape of this distribution can be described by the *Landau distribution*, which to a good approximation is given by [Gru93]

$$L(\lambda) = \frac{1}{\sqrt{2\pi}} e^{-\frac{1}{2}\left(\lambda + e^{-\lambda}\right)}, \qquad \lambda = \frac{\Delta E - \Delta E_{\mathrm{mp}}}{\xi} \tag{3.4}$$

with the most probable energy loss ΔE_{mp}. The deviation of the energy loss from the ΔE_{mp} is denoted by λ. The mean energy loss is usually approximated by taking the first multiplicative term of the Bethe-Bloch formula, $\xi = \kappa\rho x$, which also acts as normalization in the denominator of λ. κ is given in (3.2), x is the absorber thickness and ρ is the material's density.

A Landau distribution is shown in figure 3.2. Due to its asymmetry, the average energy loss is significantly higher than the most probable energy loss E_{mp}. The distribution is widened towards high energies due to the rare possibility of large one-shot energy transfers in single collisions, which result in high energy electrons. For MIPs the most probable energy loss is 26 keV in a 100 μm Silicon layer, scaling within 10% between 20 μm and 300 μm. The average differential energy loss $\mathrm{d}E/\mathrm{d}x$ is 1.66 MeV/ g cm^2.

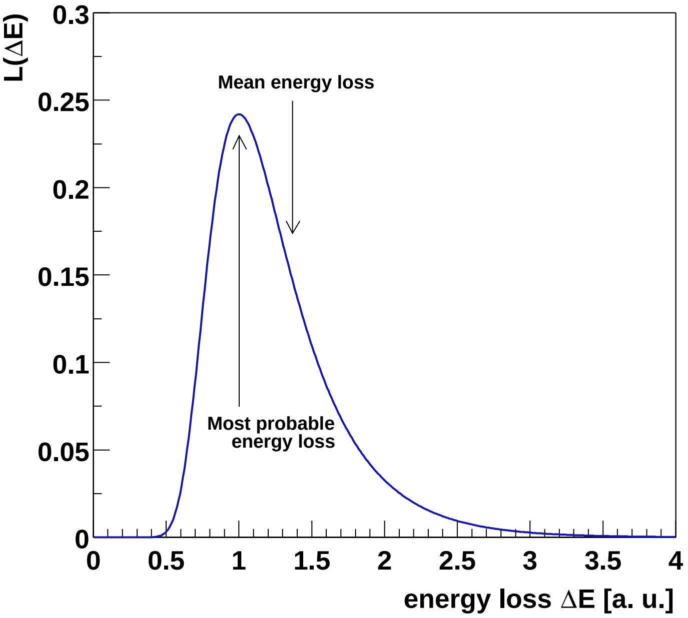

Figure 3.2: Typical Landau distribution of the energy loss in a thin absorber. The mean energy loss is shifted towards higher energies due to high-energetic electrons.

δ-electrons. Although the probability for the generation of very high-energy electrons is small, their energy range can be quite large. δ-electrons are able to create electron-hole pairs themselves and hence increase the errors in spatial resolution. A 50 keV δ-electron drifting perpendicularly to the original track creates $1.4 \cdot 10^4$ electrons along its own track, and causes a displacement of 3.3 µm of the measured track with respect to the real particle track [Pei92].

Corrections to Landau's theory. While Landau assumed thin, gaseous absorbers and a free electron cross section, with Silicon detectors we observe a broadening of the distribution caused by the binding energy of the electrons in the Silicon atoms [Hal84, Dam86]. This effect is corrected by a number of modifications calculated by Blunck and Leisegang [Mat80] and not discussed further in this thesis.

3.3 p-n junctions

In intrinsic Silicon, electron-hole pairs are created by thermal excitation. Since they are produced pairwise, the density of holes and electrons is equal. At room temperature, the *intrinsic charge carrier density* is about $n_{\mathrm{i}} = 1.45 \cdot 10^{10}\ \mathrm{cm}^{-3}$. This number is about four orders of magnitude larger than the expected signal. To lower the number of free charge carriers, a Silicon detector has to be depleted of the free charge carriers.

3.3.1 Depletion zone

To influence the properties of semiconductors, impurity atoms are introduced, which either donate or accept electrons. These impurities are integrated into the crystal lattice and create what is called *doped* or *extrinsic* semiconductors.

The amount of dopants is big in comparison to the intrinsic charge carrier density, but very small if compared to the total number of atoms in the crystal. n regions are doped with electron donors, usually elements of the fifth group. As the fifth valence electrons of such atoms have a very low binding energy, basically all these electrons are lifted to the conduction band at room temperature and become *majority charge carriers*. Likewise, p regions are doped with electron acceptors, usually elements of the third group. There, holes become the majority charge carriers.

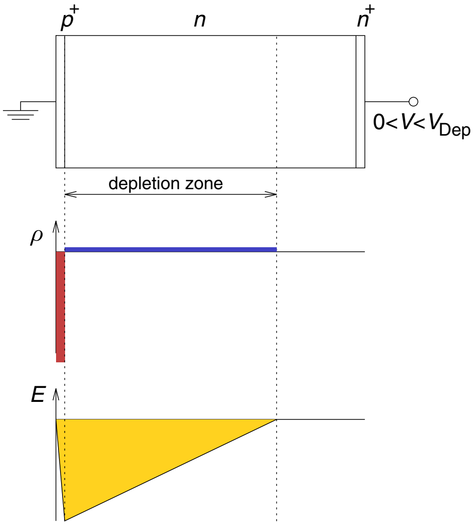

Figure 3.3: Double-sided Silicon detector with p-n junction: geometry, space charge density ρ and electric field E distribution in the depletion zone [Rie94]

A Silicon detector with double-side readout consists of a moderately n-doped substrate sandwiched between highly-doped layers. These layers are called n and p side, and we denote their dopant concentration with n^+ and p^+, respectively. The interface between the p^+ layer and the substrate is called *p-n junction*. Occasionally, the two sides of the detector are referred to as ohmic (Ω) and junction side (J). Typical dopant concentrations are $5 \cdot 10^{12}\,\mathrm{cm}^{-3}$ for donors in the Silicon bulk and $5 \cdot 10^{15}\,\mathrm{cm}^{-3}$ for acceptors in the p^+ layer.

Due to the different electron and hole densities in the n and p^+ zones, the majority charge carriers will diffuse over the junction, until a new equilibrium is formed. This equilibrium is characterized by net positive and negative charges on the n and p^+ regions, created by the immobile acceptor and donor ions in the lattice, the *space charge*. Consequently, a zone depleted of free charge carriers is created and thus an insulating region is formed. An illustration providing geometrical setup, charge density and electric field distribution is given in figure 3.3.

It can be shown that the width of the depletion zone is inversely proportional to the dopant concentration. With a high concentration of acceptors in the p layer, the depletion zone extends widely into the Silicon bulk, while for depleting the comparatively small p layer only a small concentration of donors in the n bulk material is necessary.

3.3.2 External bias voltage

Electron-hole pairs created in the depletion zone are separated by the electric field caused by the space charge. Charge created in the neutral zone of the silicon bulk, however, will be lost for readout as it can recombine with the free charge carriers there. To extend the depletion zone across the whole Silicon detector, an external bias voltage across the Silicon bulk is applied. The depletion zone grows from the p side with increasing bias voltage. As soon as the n-side is reached, we speak of a fully-depleted Silicon.

With the effective charge carrier density $N_{\text{eff}} = (n_{\text{D}} - n_{\text{A}})$, the thickness of the detector D and the dielectric constant of Silicon ϵ [PDG00], we can solve the one-dimensional Poisson equation

$$\frac{\partial^2 \phi(z)}{\partial z^2} = -\frac{q N_{\text{eff}}(z)}{\epsilon_0 \epsilon} \tag{3.5}$$

with the electric potential ϕ and find the full depletion voltage [Kle86] to be

$$V_{\text{dep}}^{(\text{full})} = N_{\text{D}} \frac{q D^2}{\epsilon_0 \epsilon} \tag{3.6}$$

with the dopant concentration in the Silicon bulk N_{D}. In contrast to unbiased Silicon with its intrinsic carrier density, depleted Silicon behaves very much like a resistor, drawing no current under the applied voltage except for the leakage current, determined by the detector's resistivity

$$\rho = \frac{1}{q \mu N_{\text{D}}}, \tag{3.7}$$

where the mobility is denoted by μ, defined as the charge carriers' drift velocity divided by the electric field applied. N_{D} is the donor concentration in the bulk (assuming $n_{\text{D}} \gg n_{\text{A}}$ for n-type Silicon). The width of the depletion zone in the Silicon bulk can be expressed by [Pei92]

$$d = \sqrt{2\epsilon\epsilon_0\rho\mu V_{\mathrm{bias}}} = \sqrt{\frac{2\epsilon\epsilon_0 V_{\mathrm{bias}}}{qN_{\mathrm{D}}}}. \tag{3.8}$$

Resistivity. Obviously, the higher the resistivity ρ of the material, the lower the bias voltage has to be in order to deplete a detector completely. Therefore, Silicon detectors usually are made of high resistivity material. Up to 10 kΩ cm have been reached exploiting special procedures [Dam86].

Leakage current. The depleted region is free from majority charge carriers. Still, under equilibrium conditions electron-hole pairs are generated continuously everywhere in the volume of the crystal. The noise in Silicon detectors arises from such thermally generated minority charge carriers. Without electric field present, they would simply recombine, but with bias voltage applied they have little chance to recombine and drift under the influence of the electric field, giving rise to what is called the *generation current*

$$j_{\mathrm{gen}} = \frac{1}{2}q\frac{n_{\mathrm{i}}}{\tau_0}d, \tag{3.9}$$

dependent on the width of the depletion zone but not explicitly on the temperature.[2] The temperature dependence comes in through given by $n_{\mathrm{i}} \sim \exp(-E_{\mathrm{gap}}/k_{\mathrm{B}}T)$. The lifetime of the minority charge carriers is denoted by τ_0. With (3.8) and (3.9) we find

$$I_{\mathrm{leak}} \approx j_{\mathrm{gen}} \sim \sqrt{V_{\mathrm{bias}}}. \tag{3.10}$$

3.4 Particle detection

As a charged particle traverses the depleted detector volume, free charge in form of electron-hole pairs is liberated along its track. For a 100 μm thick layer the average energy loss is about 39 keV. Speaking in electron-hole pairs, one obtains 72 pairs per μm for the most probable and 108 pairs per μm for the average energy loss. For commonly used detectors of 300 μm thickness, this is equivalent to a most probable number of $2.2 \cdot 10^4$ and an average number of $3.2 \cdot 10^4$ electron-hole pairs.

---

[2] For a fully depleted detector, the leakage current can be identified with the generation current alone. The *diffusion current* j_{diff}—caused by charge generated in the neutral Silicon and then diffusing to the space charge region—would contribute for non-depleted regions.

Collection time. Due to the bias voltage applied, the charge clouds created in the depletion zone are separated and drift to the readout electrodes. The collection time for electrons in Silicon can be estimated to be [Kle86]

$$t_{\mathrm{drift}} = \frac{D}{\mu_{\mathrm{e}} E} \approx 10\,\mathrm{ns} \tag{3.11}$$

for an average electric field of $3 \cdot 10^5$ V/ m, a detector thickness of $D = 300\,\mu\mathrm{m}$ and an electron mobility of $\mu_{\mathrm{e}} = 1400\,\mathrm{cm}^2\,\mathrm{V}^{-1}\,\mathrm{sec}^{-1}$. Holes have a smaller mobility of $\mu_{\mathrm{h}} = 450\,\mathrm{cm}^2\,\mathrm{V}^{-1}\,\mathrm{sec}^{-1}$, leading to a collection time of about 25 ns. To reduce the collection time, Silicon detectors may be overbiased, i. e. operated with a bias voltage exceeding the value required for fully depleting the detector.

Readout strips. Since the implanted p^+ and n^+ layers are separated into single strips with a width comparable to the width of the charge cloud, the device is sensitive to the position of the charge cloud.

The Aluminum readout strips on the detector are separated from the implanted strips by a $\mathrm{SiO_2}$ layer, acting as an insulator. The charge cloud arriving at the strips induces a signal in this metallized layer, which can be read out and amplified. By this *capacitive coupling*, readout electronics are separated from the detector current. The separation prevents dark and leakage currents from being drained off by the readout electronics.

CCE. The ratio of collected charge to charge originally generated is called *charge collection efficiency*. *CCE* is a combined effect of the semiconductor and the properties of the readout electronics. It can be shown [Bea98], that the *CCE* for MIPs shows linear behavior with $\zeta = \sqrt{V_{\mathrm{bias}}/V_{\mathrm{dep}}}$ and saturates for $\zeta > 1$, i. e. when reaching full depletion voltage, provided that all charge carriers reach the readout strips within the collecting time.

3.4.1 Spatial resolution

The accuracy in spatial resolution depends on many effects, which can be divided into *physical processes* like statistical fluctuations of the energy loss or diffusion of charge carriers during the drift and *external (design) parameters* like strip and readout pitch and detector noise. Given all such constraints, a spatial resolution of typically 5 µm for a detector thickness of 300 µm can be obtained. It is possible to design detectors with a localization precision of up to 2.6 µm.

Drift and diffusion. The charge generation by traversing particles is mostly confined in a tube of a diameter of about 1 µm around the track, drifting under the influence of the electric field applied. Assuming n-type Silicon, holes drift to the p-n junction and to the readout strips there, whereas the electrons go to the n^+ strips on the ohmic side. During drift, the charge carriers diffuse by multiple collisions, their distributions following the Gaussian law

$$\frac{\mathrm{d}N}{N} = \frac{1}{\sqrt{4\pi D t}} \exp\left(-\frac{x^2}{4Dt}\right) \mathrm{d}x \tag{3.12}$$

with $\mathrm{d}N/N$ the fraction of charge found in the element $\mathrm{d}x$ at a distance x from the origin after a time t. Here, D denotes the diffusion coefficient, related to the mobility (3.7) by

$$D = \frac{k_\mathrm{B} T}{q} \mu. \tag{3.13}$$

The width of the charge cloud is determined by transverse diffusion during the drift, following a Gaussian distribution with a full width below 20 µm and a FWHM of about 10 µm, depending on the drift field. As charge carriers generated at locations with different distances to the strips have different drift times, we obtain a superposition of different Gaussian distributions.

The wider the charge distribution at the readout strips, the more events we get with charge distributed over a *cluster* of adjacent strips. In such events, position is not only given by a single strip number, but can be measured to a much better precision by either calculating the center of gravity of the charge cloud (assuming a boxed form of the charge distribution) or using algorithms which take into account the real (Gaussian) shape of the charge distribution.

Bias voltage and spatial resolution. A low bias voltage results in a low drift field and thus the charge cloud generated has more time to diffuse. Hence, a wider charge distribution is achieved. Increasing the bias voltage on the other hand leads to narrower distributions, thus decreasing resolution.

For best spatial resolution, a bias voltage as low as necessary for full depletion is advisable. Of course, one has to make sure that the signals on the individual strips are well above strip noise, otherwise accuracy is lost. It is advisable to use high resistivity material for particle detectors, since such material depletes at lower voltages.

Strip pitch and readout pitch. With a FWHM of the charge distribution of 10 µm, it is practically impossible to collect charge on more than one strip, especially if the readout density is reduced to a readout pitch of 50 µm or more. Track positions are given by the strip number and resolution is determined by the readout strip width.

As realized in the COMPASS Silicon detectors, between every two readout strips (which are 15 µm wide and pitched 50 µm), intermediate strips are present which are not read out. Charge collected on these strips is transferred by capacitive coupling to the neighboring readout strips. Employing charge division methods, one-track resolution is enhanced substantially, although two-track resolution may decrease [Boc98b].

Theoretical spatial resolution. Assuming an ideal detector, no charge sharing, and charge being deposited exactly on one readout strip, a maximum resolution can be calculated. With the readout pitch δx, the distribution function of particle positions is 1 in the range from $-\delta x/2$ to $+\delta x/2$, and 0 otherwise (fig. 3.4).

While the expectation value of the hit position trivially equals 0, the variance is given by

$$\sigma_x^2 = \frac{1}{\delta x}\int_{-\delta x/2}^{+\delta x/2} x^2 dx = \frac{1}{\delta x}\left[\frac{x^3}{3}\right]_{-\delta x/2}^{+\delta x/2} = \frac{\delta x^2}{12} \quad (3.14)$$

For the resolution, we obtain $\sigma_x = \delta x/\sqrt{12}$. Commonly used Silicon detectors with a readout pitch of $\delta x = 50.0$ µm reach a spatial resolution of $\sigma_x = 14.4$ µm.

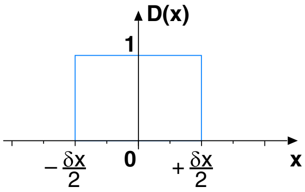

Figure 3.4: Calculation of theoretical resolution. δx is the readout pitch.

3.4.2 Noise

Since there is no primary signal amplification like e. g. in gas detectors, noise performance is a very important issue for Silicon detectors. Usually, noise is given as an *equivalent noise charge* ENC in units of electrons for comparison with the number of electrons in the charge cloud. Electronics and detector itself contribute to noise in different ways.

The electronics noise comprises of a constant part and a part dependent on detector parameters. The detector mainly contributes by the capacitance of the readout strip to the neighboring channels and to the readout of the other side. It causes signal loss and acts as a load capacitance of the preamplifier. These two effects can be minimized by choosing a small interstrip capacitance and a high coupling capacitance to the opposite detector side. For most electronics, the load capacitance gives the main contribution to the electronics noise, which usually sums up to about 300 electrons and is given by $ENC_{\mathrm{el}} = A + B \cdot C$ with constants A and B and the detector capacitance C.

Apart from electronics, the leakage current through the detector gives rise to noise, with $ENC_{\mathrm{I}} \propto \sqrt{I_{\mathrm{leak}}}$. Another source of noise are the biasing resistors, where we find $ENC_{\mathrm{R}} \propto \sqrt{T/R}$.

With the Silicon used in COMPASS, the leakage current should contribute about 70 electrons to the noise and the bias resistors about 480 electrons. With a total detector ENC of 850 electrons, a signal/noise ratio (S/N) of 25:1 can be reached, assuming a number of $2.2 \cdot 10^4$ electron-hole pairs are created.[3]

For detectors with two-side readout, the pulse heights on the two sides can be correlated to disentangle multi-hit events. For such analyses, the noise performance of the detector is essential of course.

3.5 Radiation damages

In COMPASS, the silicon detectors will be directly exposed to a hadron beam with rates of up to $6 \cdot 10^{14}$ particles/cm^2 per year, equal to an absorbed dose[4] of 0.15 MGy. Such high rates lead to radiation damages in the material up to a point where the detectors will not give reasonable signal/noise performance and cannot be used any more. The mechanisms of *radiation damages* are discussed in this section.

Fluence. A key quantity connected to radiation damages is the fluence Φ, defined as the time-integrated flux ϕ of incident particles. ϕ is the number of incident particles per time and area.

$$\Phi = \kappa \int \phi \mathrm{d}t. \tag{3.15}$$

Any particle fluence can be reduced to an equivalent flux of 1 MeV neutrons producing the same bulk damage. The choice of this normalization is (partly)

---

[3] For the definition of the signal/noise ratio, the peak of the Landau distribution is used, characterized by the most probable number of created charge carriers.

[4] Energy deposition usually is given as a dose, which measures the total energy absorbed per unit mass, $D = \mathrm{d}E/\rho \mathrm{d}V$, with $1\ \mathrm{Gy} = 6.241 \cdot 10^9\ \mathrm{MeV/\ g}$.

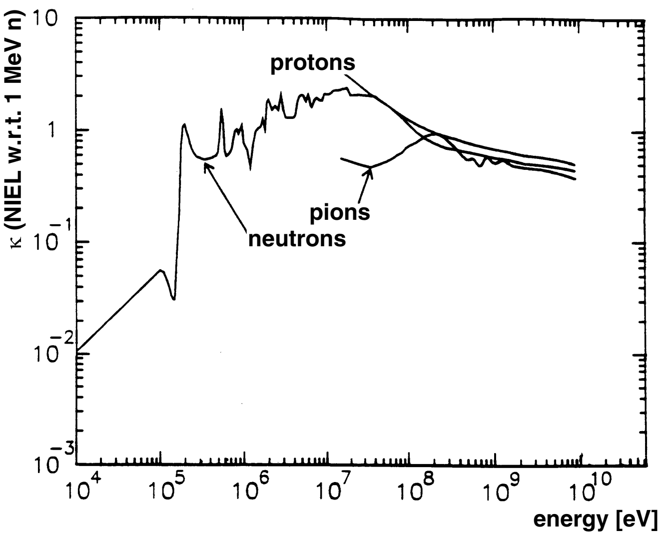

Figure 3.5: The hardness parameter κ, a scaling factor for the radiation damage relative to 1 MeV neutrons. For pions and protons in the COMPASS energy range, we find $\kappa \approx 0.8$ [Huh93].

due to historical reasons. For other particles and energies, the *hardness parameter* κ is a scaling factor giving the relative strength of irradiation (fig. 3.5).

In general, the properties of a semiconductor device exposed to irradiation are mainly modified by two processes, ionizing and non-ionizing energy loss of particles crossing the detector.

Ionizing energy loss. Ionization is caused by charged particles deposing part of their kinetic energy in the crystal lattice. Electron-hole pairs produced due to ionizing energy loss recombine or are collected by the guard rings[5]. This type of energy loss is utilized to detect particles and causes no permanent damage to the detector material. However, damages can occur in interfaces and insulating layers at the detector surface: Holes trapped in the oxide layer or states created near the oxide-semiconductor junction may result in unwanted increased charge sharing between adjacent readout strips and increase noise due to interstrip capacitance. Influence on the detector performance takes place after heavy irradiation of the order of an absorbed dose of 10 kGy and can be reduced by dedicated radiation hard design.

NIEL hypothesis. *Non-ionizing energy loss* for charged particles is mainly due to takes Rutherford scattering. Collisions of incident particles with lattice atoms cause displacement of these atoms or, more generally speaking, lattice defects. The liberated atoms leave vacancies in the lattice, which can move through the crystal. Doing so, they liberate more atoms until they have spent all their kinetic

---

[5] a feature of radiation hard Silicon detectors, discussed in more detail in section 4.1.2

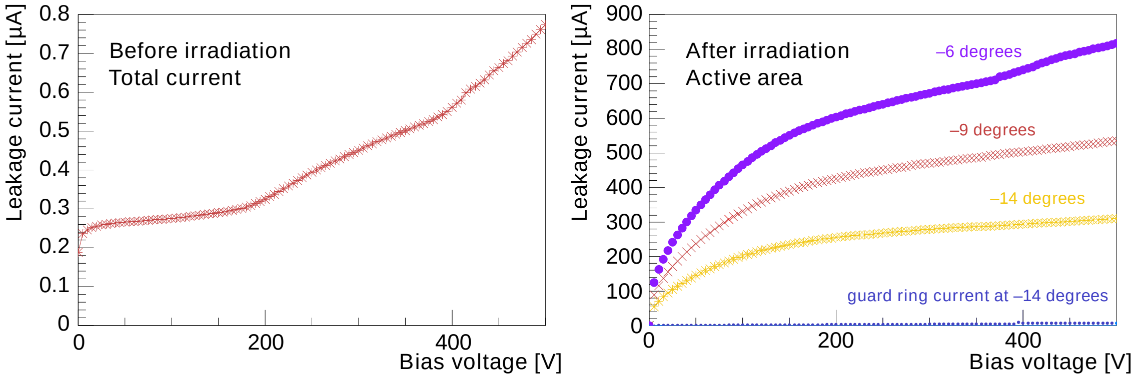

Figure 3.6: Leakage current before and after irradiation of a double-sided detector. The measurements were done with a silicon wafer design also used for COMPASS. The detector was exposed to a fluence of $3 \cdot 10^{14}$ protons/cm^2 [Abt99]

energy and come to rest as interstitials. A cascade of lattice defects is formed. Such defects predominantly act as acceptors, i. e. they neutralize the existing donors. The concentration of donors decreases exponentially with fluence, while the number of created acceptors increases linearly with it,

$$N_{\mathrm{eff}} = n_{\mathrm{D}} \cdot \exp(-c\Phi) - n_{\mathrm{A}} - \beta\Phi. \tag{3.16}$$

Both effects combined make the semiconductor behave more and more acceptor-like. Consequences for semiconductors are manifold. Detector noise will increase with growing leakage current

$$\Delta I = \alpha\Phi, \tag{3.17}$$

with a material constant α. This increased leakage current originates from additional thermal generation of electron-hole pairs at lattice defects. Figure 3.6 shows the evolution of the leakage current for detectors developed for HERA-B before and after irradiation.

When measuring the energy loss in a semiconductor device, all charge carriers arriving at the readout strips in a certain time are collected. Thus, carriers which recombine at defects or are trapped in metastable states for sufficiently longer times are lost for readout and contribute to a decreased *charge collection efficiency*. Signal amplitudes will decrease together with the charge collection efficiency. This effect increases with fluence, but can be countered by overbiasing the detector.

With increasing fluence, donor removal and acceptor creation lead to what is called *type inversion* (fig. 3.7): The weakly n-doped Silicon bulk becomes p-doped. From then on, the depletion zone will grow starting from the n-side, resulting in shortcut p strips as long as the detector bulk is not fully depleted. Type inversion occurs at a neutron fluence of approximately 10^{12} cm^{-2}.

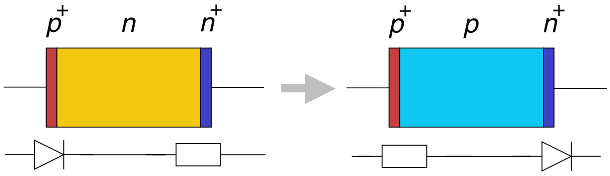

Figure 3.7: Type inversion: The originally moderately n-doped Silicon bulk gets p-doped by irradiation. This is caused by donor removal and acceptor creation in the bulk material. As soon as type inversion occurs, the bias voltage applied on the detector has to be reversed.

Up to the point of type inversion, the voltage necessary to fully deplete the Silicon bulk will decrease to 0 V, whereas from then it will increase with growing fluence up to values of well above 200 V. Effective doping against total flux is plotted in figure 3.8. From a fluence of $2 \cdot 10^{13}$ cm^{-2} on, the voltage necessary for fully depleting the detector will exceed the detector's maximum bias voltage. The active volume at this maximum voltage will then decrease until the signals get to weak to be disentangled from the detector noise.

Annealing. Certain defects are able to *anneal*, i. e. they diminish exponentially with time. Time constants vary over a wide range from minutes to months and are temperature-dependent as well.

Annealing only applies to acceptor-like defects, while donor-like defects need temperatures well above 100°C to anneal [Fre93]. Another important mechanism is *reverse annealing*: Inactive defects may be activated by irradiation and start acting like additional acceptors. As time constants for anti-annealing are rather large, this effect may take place long after irradiation and thus becomes important during long periods of irradiation. Reverse annealing is supported by high temperatures, which makes cooling necessary throughout the complete annealing time, i. e. even after exposure to high fluences.

3.6 The Lazarus effect

Radiation damages cause Silicon detectors to change their properties drastically with increasing fluence, up to a point where operation at room temperature is not possible any more. The RD39 collaboration at CERN has shown [Pal98] that charge collection efficiency (CCE) recovers when detectors are operated at cryogenic temperatures. This phenomenon often is referred to as *Lazarus effect*. A review is given in [Bor00].

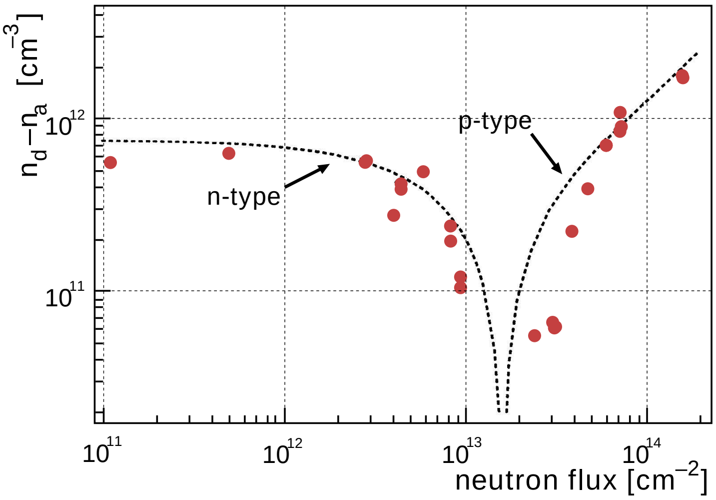

Figure 3.8: Effective doping as a function of (neutron) fluence for high-resistive n-doped silicon [Sot94]

3.6.1 Phenomenology

The Lazarus effect shows distinctive temperature dependence. At temperatures below 180 K, the CCE of irradiated detectors is increasing rapidly up to a maximum value at about 130 K common for all samples, as figure 3.9 shows. The detector efficiency is still dependent on the irradiation dose, but signals at cryogenic temperatures are considerably larger than ones at room temperature and big enough for operation.

Together with the recovery of CCE, the leakage current decreases under cooling. Its temperature dependence is given by [PDG00]

$$I \propto T^2 \exp \frac{E_a}{2k_B T}, \tag{3.18}$$

with an activation energy $E_a = 1.2\,\mathrm{eV}$. For Silicon this means that the leakage current is reduced by a factor of 2 for a step down in temperature by 5 K. Another interesting feature is that the CCE shows a time evolution if the detector is operated with reverse bias, decreasing from a high value to a reduced saturated value. This result is shown in figure 3.10.

Apart from CCE recovery, cryogenic temperatures permit forward biasing of Silicon detectors, since Silicon becomes an insulator. At room temperatures this is not possible since the bias current in forward direction is much too high, whereas at cryogenic temperatures irradiated detectors show a negligible bias current for both polarities. In figure 3.10, CCE is also plotted for different forward bias voltages. With forward biasing, comparatively high CCE is reached for voltages up

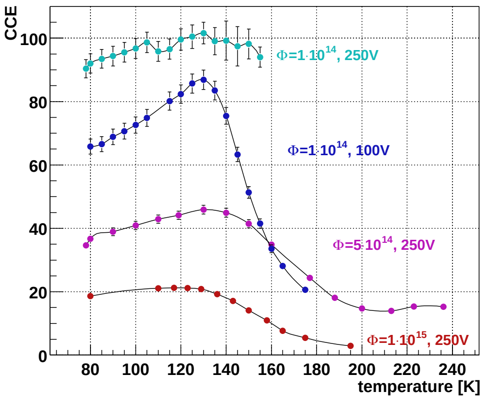

Figure 3.9: CCE at different temperatures. The curves show measurements for detectors exposed to different radiation doses [Bor00].

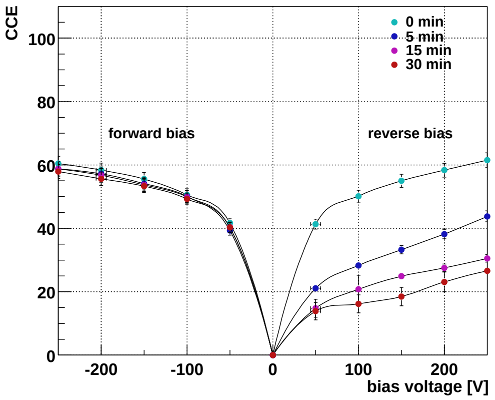

Figure 3.10: CCE for different bias voltages, measured with a detector exposed to a dose of $2{\cdot}10^{15}$ n/cm^2 [Bor00]

to 200 V. In addition, no time dependence is observed, as opposed to the reverse bias case.

3.6.2 Current understanding of the Lazarus effect

The efficiency of a Silicon detector is proportional to the width of its depleted zone. As soon as a certain level of fluence is reached, full depletion may not be possible any more, as the necessary voltage exceeds the highest possible bias voltage for the detector. The non-depleted volume of a detector cannot contribute to particle detection. Moreover, it acts lika a resistor to an AC signal. The signal height is proportional to $Q \cdot d/D$ [Bea98], with the total generated charge Q, the width of the depleted zone d and the total detector width D. It can further be shown that for MIPs the generated charge is proportional to d/D. We expect CCE to scale as

$$\mathrm{CCE} \propto \frac{d^2}{D^2}, \tag{3.19}$$

or with the bias voltage, as discussed in section 3.4.

Free charge carriers can be trapped in the semiconductor. Traps are formed by deep-level radiation induced defects, which increase the effective doping concentration N_D and are created by mechanisms discussed in the previous section. Trapping is characterized by a time constant τ_trap.

After a certain time, characterized by an *emission time constant* τ_e, they are liberated again. If $\tau_\mathrm{e} \gg t_\mathrm{drift}$, i. e. if emission time is considerably longer than the collection time (cf. section 3.4), the trapped charge carriers are lost for readout, and efficiency drops even for a fully depleted detector:

$$\mathrm{CCE} \propto \frac{d^2}{D^2} \exp\left(-\frac{t_{\mathrm{drift}}}{\tau_{\mathrm{trap}}}\right). \tag{3.20}$$

When temperature is lowered, the emission process is strongly reduced due to the exponential dependence of the emission time constant on temperature:

$$\frac{1}{\tau_{\mathrm{e}}} \propto \Delta E / k_{\mathrm{B}} T. \tag{3.21}$$

ΔE is the distance of the defect from the valence band or conducting band, respectively. The effect is pronounced for deep traps in the Silicon band gap, where $\Delta E \approx 0.5\,\mathrm{eV}$, whereas for shallow traps with smaller values of ΔE it is not that effective. (3.21) implies that at cryogenic temperatures, the equilibrium between trapping and re-emitting charge carriers gets strongly unbalanced.

It should be possible to freeze out defects by increasing the emission time and constantly filling the traps with charge carriers. If a significant fraction of traps stays filled, the effective charge carrier density in the Silicon bulk is decreased. According to (3.8), this results in an increased width d of the depleted zone for a given bias voltage, increasing CCE. The process seems to be most efficient at 130 K. Below this temperature, the decreasing CCE might be explained by a possible overcompensation, leading to an increasing effective CCE.

In addition, filled traps cannot capture radiation-induced carriers. This increases τ_{trap} in (3.21), again contributing to an increasing CCE.

To ensure that trapping has no negative effect on the charge generated by passing particles, charge carriers filling the traps can be injected by constantly generating them with light-emitting diodes. Forward biasing has the same effect, as charge carriers to fill the traps are constantly provided by the bias voltage.

Chapter 4

Implementation of Silicon trackers in COMPASS

This chapter describes the implementation of Silicon trackers in COMPASS. It deals with the design of the Silicon detectors and their specific eligibility for high-radiation environment, the mounting structures (cryostats and supports), the front-end electronics and the readout chain.

4.1 Detector design

For COMPASS, double-sided Silicon originally designed for the HERA-B experiment is used [Abt99]. The design was done at the Halbleiter-Labor (HLL) of Max-Planck-Institut für Physik, München. The wafers the COMPASS Silicon group received came out of a batch produced by SINTEF (Oslo, Norway) [Ber97], and show slight technological differences compared to the original HLL design.

Geometry. As the spatial resolution is dominated by multiple scattering contributions, a reduction of the amount of material used is desired; therefore, double-sided Silicon detectors are favored, because double the information is achieved with the same amount of material as would have been necessary for single-sided readout. Two double-sided detectors constitute a so-called station. Such a station has to provide three or more independent projections so that ambiguities in multi-hit events can be disentangled and ghost hits can be rejected. Therefore a stereo angle of 5° of the two detectors with respect to each other was chosen (fig. 4.1). This allows the largest possible overlap of the two detectors and at the same time to use the same wafer design for both detectors in one station. The two detectors are mounted back-to-back in a cryostat, where the first of them gives

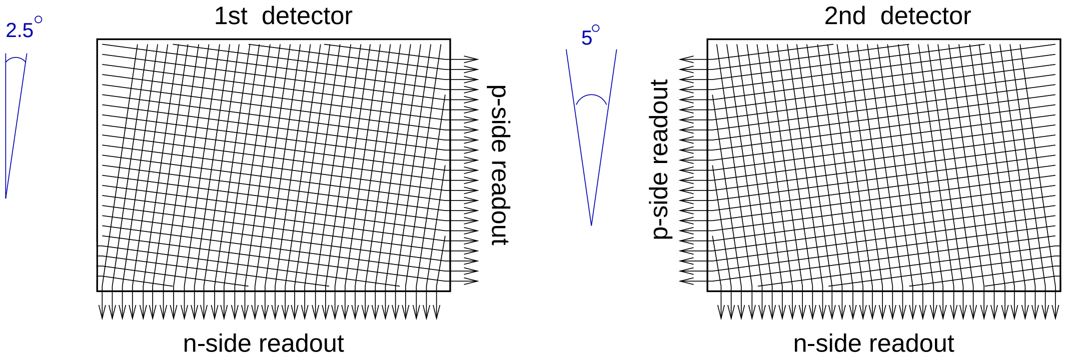

Figure 4.1: Readout strips on the two double-sided detectors mounted in one tracking station. The strips are inclined by 2.5° with respect to the wafer. 58 strips on the p side are not connected to readout electronics, since their bond pads end on the other side of the wafer [Abt99]

x and y projections inclined by 0° and 90° with respect to the COMPASS coordinate system, the second u and v views with inclination angles of -5° and 85°, respectively.

4.1.1 Processing

The detectors were processed on 280 µm thick, n-type Silicon substrate of $2 \ldots 3\ \mathrm{k\Omega\,cm}$ resistivity. They provide an active area of 50×70 mm and a readout pitch of 54.667 µm on the n-side and 51.667 µm on the p-side. A cross section of the Silicon microstrip detectors is given in figure 4.2.

The p-side is separated into 2047 strips, of which every second one is read out. The intermediate strips enhance the spatial resolution by charge division as discussed in section 3.4.1. The readout strips are 15 µm wide, while the intermediate strips have a width of 8 µm. On the n-side, 1280 readout strips are present, which are arranged perpendicularly to the p-side strips.

Separation on the ohmic side. The readout strips on the p-side are isolated from each other by the Silicon bulk. This isolation is supported by fixed positive oxide charge in the oxide layer at the Si-SiO_2 interface, which induces an electron layer in the Silicon bulk. On the n side, however, such accumulated electrons between the readout strips would simply shortcut them. With a spread charge on the n-side, position measurement becomes nearly impossible. To read out the n^+ strips separately and to preserve spatial information, they have to be isolated from each other. This is done by 15.667 µm wide, highly p^+ doped compensation implantations arranged between the n^+ readout strips, so called *p-stops*.

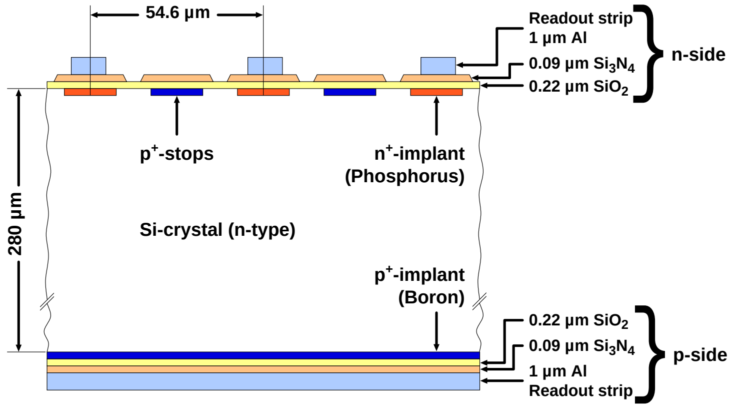

Figure 4.2: Cross section of the Silicon detectors used in COMPASS [Abt99]

4.1.2 Radiation-hard design

With an expected trigger rate of up to 100 kHz and the beam passing right through the center of the detector area, the detectors have to cope with fluences of up to $6 \cdot 10^{14}/\text{cm}^2$ per year of run time. In order to stand such high rates, a dedicated radiation-hard design for the detectors was developed for HERA-B; various tests on radiation hardness were carried out [Abt95, Abt96]. Details of the features introduced include:

- Capacitive coupling of the readout strips
- Polysilicon resistors for strip biasing
- A multi guard ring structure

Capacitive coupling. To reduce leakage currents, the readout electronics are coupled capacitively to the Silicon. For this AC coupling, the Aluminum readout strips are separated from the n^+ and p^+ implants by a layer of Silicon dioxide and strips of Silicon nitride. The Si_3N_4 strips atop the oxide reduce the chance of short circuits (*pinholes*) in the coupling capacitors. Moreover, they provide equalization of the potential on the detector surface due to their limited conductivity, and they act as a diffusion barrier against impurities during processing [Fox96].

Biasing. Usually, the bias voltage for depleting the detector is provided by punch-through contacts to the readout strips. However, irradiation studies [Abt99] have shown that this technology is not sufficiently radiation resistant, as traps, which are created in the punch-through channel, lead to an increase in

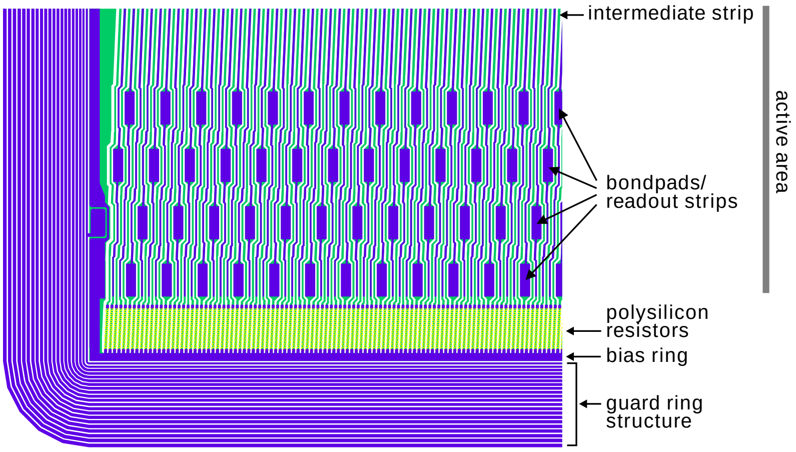

Figure 4.3: Layout of one corner of the n-side of the Silicon detector [Abt99].

noise. Therefore, strip biasing is done with polysilicon resistors of approximately 1 MΩ. Such structures are less sensitive to point defects.

The multi guard ring structure. With increasing radiation damages, the detectors are expected to need voltages as high as $300 - 500$ V for full depletion of the Silicon bulk. A structure of 16 punch-through guard rings has been applied on both sides of the detectors (fig. 4.3) in order to shield the active area from surface and edge leakage currents. Additionally, a gradual drop of the potential from the detector rim towards the potential of the undepleted substrate is provided. Stable operation of the detectors at a bias voltage well above 500 V has been shown [Abt96].

Cold Silicon. While the Silicon detectors in HERA-B are planned to be exchanged once every run time, in COMPASS it is intended to extend the Silicon lifetime even longer than one beam time by operating it at temperatures of 130 K and exploiting the Lazarus effect (cf. section 3.6). Cold detectors at least for the spectrometer stations are challenging, since there a minimization of material and radiation length is required.

4.2 Silicon stations in COMPASS

For the 2001 muon run, it was planned to have Silicon detectors in front of the target as a beam telescope. Therefore, apart from 2 stations of scintillating fibers, three detectors were ready to be installed, giving 6 projections altogether.

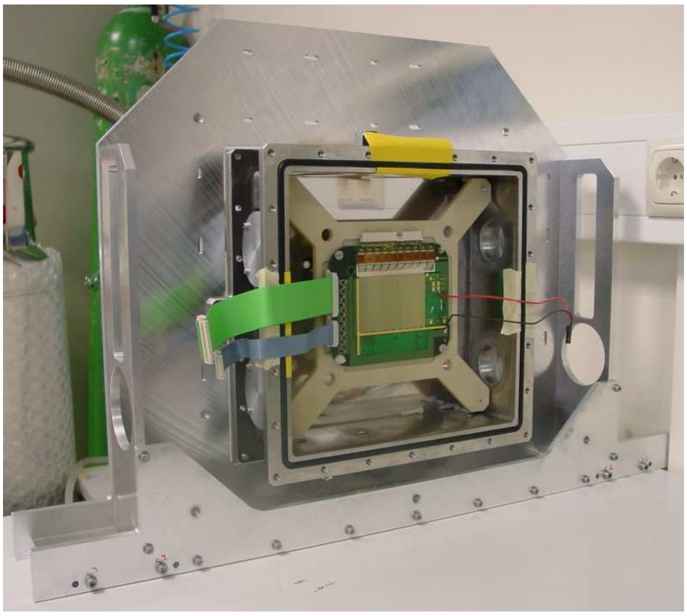

Figure 4.4: Support for the target area with installed cryostat and detector SIL8

In future runs, a total number of 4 *target stations* is planned, consisting of 8 detectors altogether. For the *spectrometer stations*, it is planned to accompany the 7 existing tracking stations with 2 Silicon detectors each. The tracking stations presently comprise large area trackers (Straws or MWPCs) and GEMs at various positions in the experiment.

4.2.1 Silicon detectors

Between November 2000 and August 2001, four Silicon detectors were assembled and fully equipped with readout chips. Table 4.1 summarizes their characteristics and usage. Detector SIL6 was produced for the T11 test beam in April (chapter 6), while the other three detectors were assembled in July. For the COMPASS beam time, the detectors had to be equipped with cooling tubes. Unfortunately, its Silicon wafer broke during this procedure, so that for the 2001 beam time, only the remaining three detectors could be used.

The cooling tubes are arranged on the front-end boards between readout chips and Silicon wafer. The reason for this is that the chips produce a considerable amount of heat, and the tubes should, besides cooling, also serve as heat barrier, so that the temperature gradient over the Silicon is as small as possible.

Since cold Silicon is still under development, up to now no cooling to cryogenic temperatures has been applied. The tubes were flushed with Nitrogen gas at room temperatures instead. After the gas has passed the chips and the Silicon wafer inside the tube, it is released into the cryostat. This is done to keep the temperature inside the cryostat in a range where stable readout conditions can be maintained.

Wafer	V_{dep}	Capacitance at 40 V	Usage	Detector name in COMPASS
SIL6†	26 V	1339.9 pF	Fully equipped, T11 test beam	—
SIL8	38 V	1356.1 pF	Fully equipped, COMPASS 2001 run	SI01XY
SIL10	84 V	1918 pF	Fully equipped, COMPASS 2001 run	SI02UV
SIL12	88 V	1925 pF	Fully equipped, COMPASS 2001 run	SI02XY

†broken during mounting of cooling tubes

Table 4.1: Detectors used in the T11 and M2 runs in 2001. The data for are taken from SINTEF data sheets.

4.2.2 Target region

One Silicon station consists of two detectors mounted on a Stesalit fiber glass support in a stainless steel cryostat. The cryostat provides stable working conditions for the Silicon detectors and allows cooling to liquid Nitrogen temperatures.

To reduce the amount of material "seen" by the beam, the cryostat is equipped with round entrance windows with a diameter of 86 mm along the beam axis, which are only covered with black plastic foil for light shielding and aluminized mylar for electrical shielding. Around the target, the beam is confined to a comparatively small area. Therefore, apart from material reduction in the beam vicinity, the cryostat design is rather simple and does not take into account material budget considerations for minimizing the *radiation length*[1] X_0. Expressed in units of X_0, the two Silicon wafers in one station contribute $X = 6.42 \cdot 10^{-3} X_0$, while the shielding foils account for $X \approx 1.5 \cdot 10^{-3} X_0$.

The cryostat is fixed to a support structure, which also carries the repeater cards. Figure 4.4 shows an opened cryostat mounted on a support frame in the lab. In the COMPASS hall, the support itself is fixed on an optical bench, which allows alignment along all three coordinates. All components of the cryostat and of the support are designed for precise surveying of the system, which is important to align the detector to the experiment coordinate system. A picture of the setup in the COMPASS hall in the 2001 beam time is given in figure 4.5. A schematic view of cryostat, support and optical bench is shown in figure 4.6.

---

[1] Radiation length is defined as the distance over which the energy of a high-energy electron is reduced by a factor of 1/e due to radiation loss only [Leo87]

Figure 4.5: Setup in the COMPASS hall. On the concrete platform, the blue optical bench can be seen, on which a Silicon support is mounted. The cryostat's window is still closed with a fiber glass plate. Downstream of the Silicon, one Scifi station is located (white plane). The orange fibers along the concrete block belong to the Silicon readout chain-

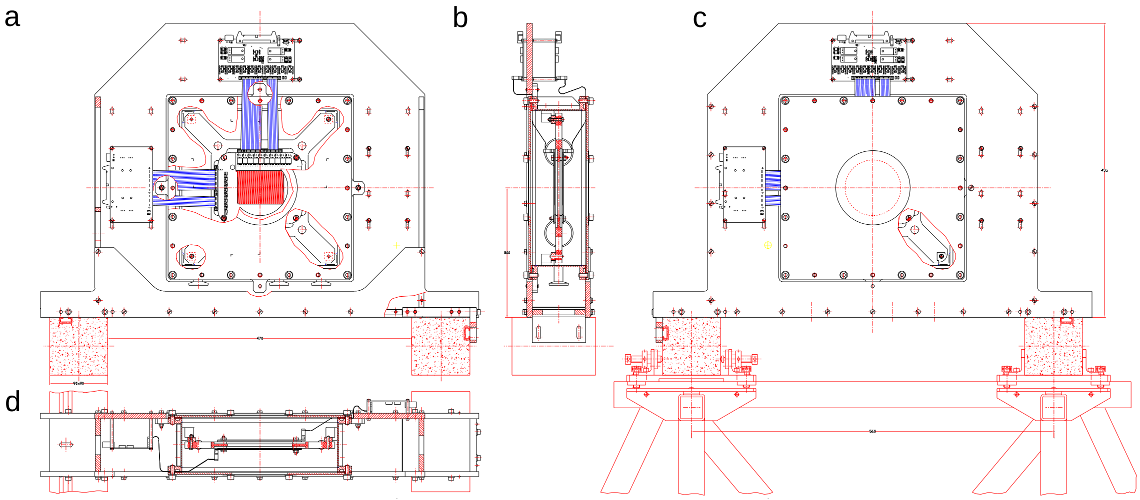

Figure 4.6: Schematics of a target region cryostat, including Silicon detector (red), repeater cards (to the top, left, and right of the detector), and optical bench (red). a) front, b) side, c) back, and d) top view

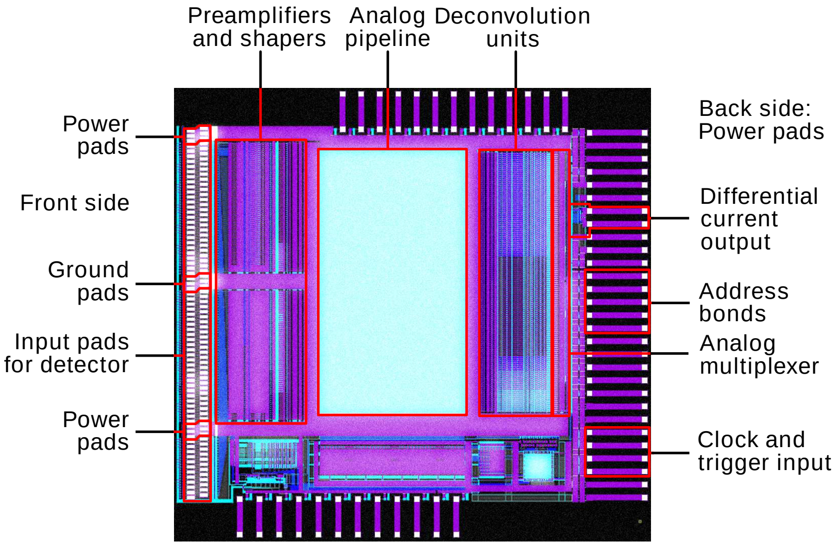

Figure 4.7: Layout of the APV25 chip. To the left ("front side") we see the bonding pads for the readout strips. The bonding pads on the right are for output, clock, trigger and power lines are on the right ("back side"). The pads on top and bottom are probe pads.

4.3 Front-end electronics

Readout of the detectors is done via the APV25-S0 chip developed for the CMS Silicon trackers at LHC [Jon99, Ray00, Jon00, MED]. The front-end electronics, consisting of the APV chips themselves and the front-end boards housing chips and the Silicon wafer itself, is described in the following.

4.3.1 The APV25-S0 readout chip

The APV25-S0[2] is a 128 channel analog pipeline ASIC[3] for readout of Silicon microstrip detectors in the CMS tracker at LHC. In COMPASS it is used as readout chip for both GEM and Silicon microstrip detectors. The chip has a total size of 8.2 × 8.0 mm^2, with an active area of 7.2 × 6.5 mm^2. It is fabricated in a 0.25 micron CMOS process to take advantage of the radiation tolerance, lower noise, lower power consumption, and the high circuit density which can be achieved. The APV25-S0 is running at a frequency of 38.88 MHz. It amplifies signals from Silicon detectors of magnitude 100 mV (25000 electrons) and continuously samples the signals at the amplifier stage every 25 ns.

Each channel of the APV25 comprises a low noise CR-RC type shaping amplifier

---

[2] **A**nalogue **p**ipeline, **v**oltage-type

[3] **A**pplication **s**pecific **i**ntegrated **c**ircuit

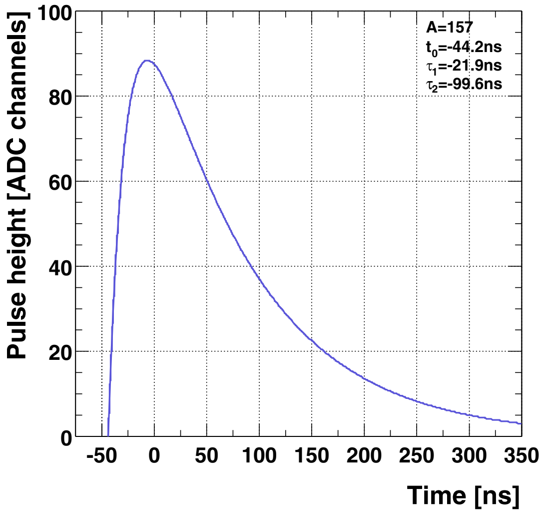

Figure 4.8: Response of the APV chip, generated by injecting an δ-shaped charge pulse into an APV [Wie00]. A product ansatz of two exponential functions has been fitted to the measured APV response.

which reshapes the arriving charge cloud into a well-defined 50 ns voltage pulse, a 160 element deep analog pipeline, and a pulse shape processing stage. On trigger request, analog samples are multiplexed onto a single differential output for subsequent transmission to the DAQ system.

Pipeline. The pipeline consists of 160 switched capacitor elements for each channel, which work like a circular buffer and are used to store the data between the hit and the trigger (this time is called *latency*) up to a maximum time of 4 µs or 160 clock cycles. As soon as a trigger is received, either one or three columns of the capacitor array are marked for readout. Once marked, these columns cannot be overwritten until the data has been read out. The maximum number of markers available is 20.

APV response. The time evolution of the APV response can be studied by varying the trigger latency. Such a scan can be done by injecting a δ-shaped charge pulse into an APV chip [Wie00]. The response can be fitted by a product ansatz of two exponential functions,

$$R = A \left(1 - \exp^{-(t-t_0)/\tau_1}\right) \exp^{-(t-t_0)/\tau_2}, \tag{4.1}$$

with t_0 the begin of the rise, τ_1 the time constant of the rising edge, and τ_2 the time constant of the falling edge (fig. 4.8).

Modes of operation. The APV25-S0 can be operated in three modes. In *peak mode*, only the contents of one specific memory cell is read out, preferably the cell containing the peak of the signal. With low intensities, this should already be sufficient to reconstruct hits and yield maximum linearity. Due to uncertainty in the signal timing, the signal to noise ratio attainable is about 90% of the maximum ratio.

Since COMPASS is a fixed target experiment, there is a jitter of 25 ns between the exact peak position of a hit in the pipeline and the arrival of the trigger. At higher intensities, background from signals still present in the detector from hits at earlier times may add to the observed events. To remove this *pileup* and determine the precise timing of the signals of interest, in *multi-mode* the APV25-S0 allows to read three consecutive pipeline cells. In COMPASS it is planned to study the time evolution of the signals over a period of 50 ns (readout takes place at times 0 ns, 25 ns and 50 ns, respectively) and thus determine the signal timing. Tools to obtain time resolutions of the order of nanoseconds are currently developed ([Fri01], sect. 6.3.7). Unless stated otherwise, for all analyses done in this thesis multi-mode was used.

Another mode distinctively designed for high data rates is the *deconvolution mode*. Here, like in multi-mode, three consecutive samples are read, but treated with a three-weight FIR[4] deconvolution-type algorithm, outputting a weighted sum. This algorithm reshapes the analog pulse to a peak of 25 ns length, the height of the peak corresponding to the charge collected. Effects of pileup are removed, but the time resolution in this mode is limited to 25 ns.

The output data format. Without triggers, a synchronization pulse (*tick*) is sent out every 1.75 µs, which can be used to synchronize readout electronics with the chips.

As soon as it receives a trigger signal, the APV25 sends data as a differential current, i. e. signal and inverted signal are carried by the two signal lines, respectively, and have to be subtracted from each other to regain the original signal. Noise that is picked up simultaneously by both lines cancels.

Transmission can be done at 38.88 MHz and 19.44 MHz. Currently, the latter transmission frequency is used, since it leads to lower noise on the multiplexer stage of the APV chip. It is planned to switch to 38.88 MHz in the future (cf. sect. 6.3.6), but this mode has not been tested up to now. For output, the 128 data channels are sent out serially by the APV. They are preceded by a 12 bit "digital" header, comprising 3 header bits signaling the start of transmission, 8 bit

---

[4] **F**inite **I**mpulse **R**esponse filter, a non-recursive filter defined as a sum of step functions in the frequency domain [Boc98a]

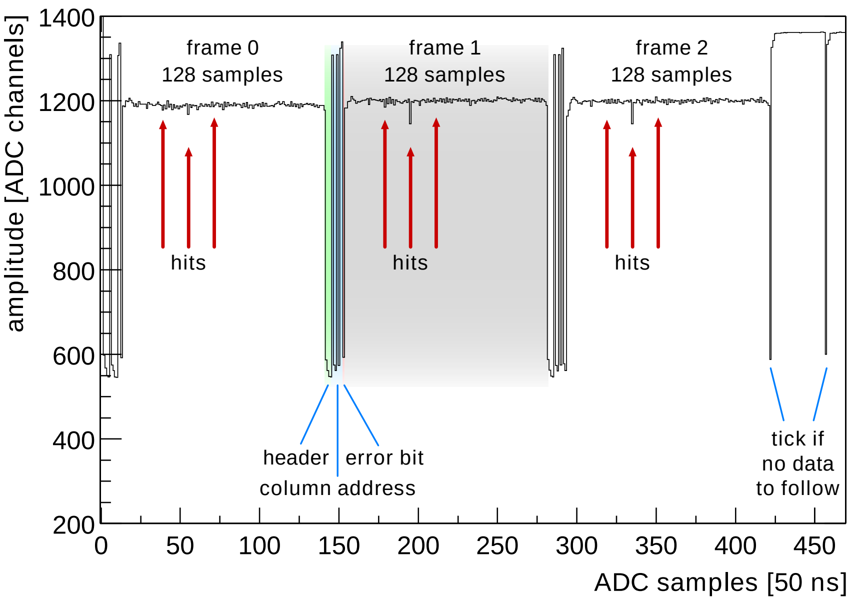

Figure 4.9: Raw output of the APV25 chip in multi-mode. As soon as a trigger is received, the APV25 sends out a block of data (*frame*). One frame consists of 12 header bits followed by 128 channels of analog data. The header bits contain “digital” information, *true* denoted by an ADC amplitude of about 600, *false* by an amplitude of about 1200. Having transmitted the data, the chip starts sending synchronization ticks until the next trigger is received.

indicating the pipeline address where the data originated from and one error bit. In multi-mode, three such *frames* of 128 channels are sent for the three consecutive trigger delays, each of them taking 21 µs for output (fig 4.9).

The maximum signal height is designed to provide a range of a 8 MIP signal. Signal height of the analog baseline can be adjusted as well as the polarity of the signals (signal reversal). This is necessary, as negative and positive charge is collected on the respective sides of the Silicon detector, while the amplifiers in the readout chain are optimized for one polarity (electrons) only.

Analog multiplexer. The APV25 uses a three-stage current mode architecture multiplexer, so that the order in which the channels are finally transmitted over the data lines is not representing the geometrical order of the input channels. The recuperation of the primary channel order from the APV output is called *reordering*. This multiplexing can be exploited in noise studies. Noise originating before the APV multiplexing stages will result in possible cross-talk to adjacent channels on the detector, while noise picked up after the multiplexers can be detected by cross-talk to neighboring channels in the readout ordering of the channels.

Programming of the APV25. For sending settings and configuration to the APV chip, a protocol compatible with the Philips I^{2}C standard is implemented [Jon00]. The chips have individual 5 bit wide I^{2}C addresses, which are defined by bonding

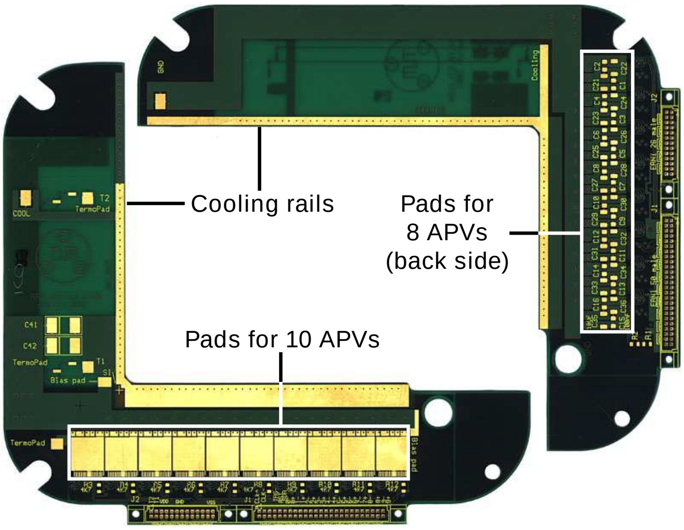

Figure 4.10: Front-end boards ("L-boards"). A set of two boards, one carrying 10 APV chips, the other one 8 chips, are needed for one Silicon wafer. The wafer is sandwiched between the boards.

out address pads on the chip. The binary address 11111 is reserved as a broadcast address to which all chips on the I^2C bus listen, the remaining 31 addresses can be used to address up to 31 chips individually.

4.3.2 Front-end boards

The Silicon wafer is glued to two L-shaped front-end boards. Figure 4.10 shows one set of these boards. The 1280 channels on the n-side and 1024 channels on the p-side are read out with 10 and 8 APV25 chips respectively. On the left board, the pads for 10 APV25 chips are visible, the remaining 8 pads are on the back side of the right board. The boards also provide pads for the Silicon bias voltage. As the bias voltage is applied between them, the two boards are on different ground potentials. Right below the pads for the chips, contacts for two flat cables are visible. These cables provide data transmission lines as well as power lines, a configuration bus, and clock and trigger information.

The front-end boards also provide cooling facilities. Tubes for liquid Nitrogen can be mounted near the Silicon wafer and the chips. Heat is transferred via the metal layers ("cooling rails") on the boards. For temperature control, each L-board hosts two thermometers.

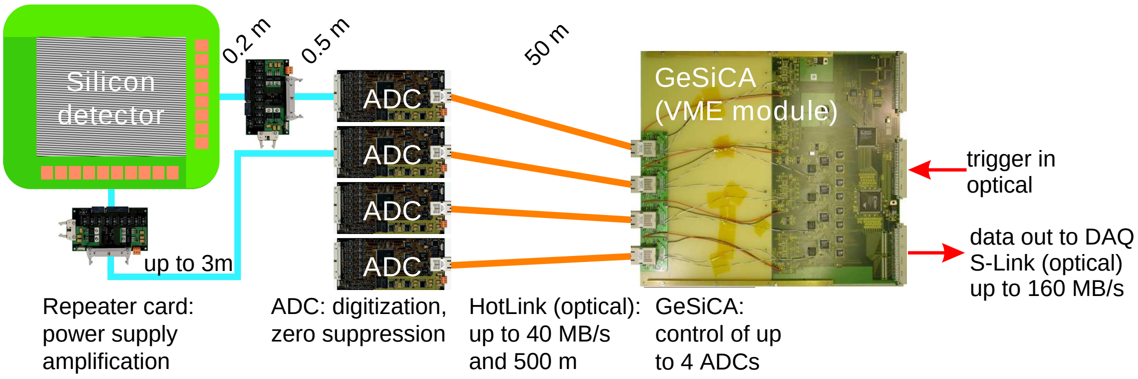

Figure 4.11: Silicon readout chain (not to scale)

4.4 Silicon readout chain

A specialized readout chain (fig. 4.11) has been developed for Silicon and GEM detectors, employing features like data reduction algorithms and fast readout. Optical data transmission is used, since the two sides of one detector are read out with the same readout chain, although they are on different potentials due to the bias voltage applied to the detector.

Details on the COMPASS readout system and a thorough description of the data reduction algorithms in the ADC are given in [Gru01].

4.4.1 Repeater cards

A first signal preamplification is done in the *repeater cards*. One repeater board for each side is used. Apart from amplification, the boards provide power for the APV chips, distribution of clock and trigger lines, and an interface for temperature monitoring on the L-boards. In COMPASS power supply for the repeater boards is done with floating C.A.E.N. low voltage power modules, which allow monitoring of the currents that the APVs draw. Together with temperature monitoring, these currents proved to be an important tool for checking the chips' status and for remote debugging purposes.

4.4.2 The Silicon/GEM ADC card

For digitization of the APV signals, an ADC card developed for GEM and Silicon readout is used (sg_adc). One card processes information received from the repeater board of one detector side. Digitization is done with 10 bit precision. The

APV header information is merged with additional event information into a new header and data is sent out via optical fibers. The implemented *Hotlink* protocol permits transfer rates of up to 40 MByte/s on optical fibers.

Modes of operation. The sg_adc provides two modes of operation. In *latch-all mode*, the amplitudes of all channels and all three samples are transmitted to the readout chain. An amount of 9 kB data per event and detector is produced, limiting readout to a relatively low trigger rate of about 1 kHz. To increase performance, dedicated data reduction methods have been implemented in the sg_adc.

Zero suppression & common mode correction. In *sparse mode*, a Xilinx FPGA[5] chip on the card performs pedestal subtraction for each channel.[6] In addition, a correction for collective changes of all pedestals—the *common mode*—due to a baseline shift of individual APV chips is done. Only data of channels which exceed a given threshold is transmitted. Since a high fraction of channels contain low-amplitude noise, the data rate is reduced considerably by *zero suppression*. Thresholds and pedestals are loaded into the ADC via software using the I^2C protocol and are obtained from dedicated pedestal runs in latch-all mode. For the future, mechanisms to obtain pedestals during data runs are considered.

4.4.3 GeSiCA

GeSiCA[7] is a control module housed by a VME crate, managing communication between ADCs and the data acquisition system. It sequentially multiplexes data of up to four ADCs connected via Hotlink and sends them via a 160 MB/s optical Slink connection [Bij01] to the COMPASS data acquisition. Moreover, GeSiCA receives the experiment-wide clock and trigger through a TCS[8] receiver and distributes them to the ADC. For configuration, the APVs' I^2C bus can be accessed and configuration registers of GeSiCA can be set via the VME bus and a VME front-end machine running Linux. Loading scripts and software for configuration settings for GeSiCA, ADC and APVs have been developed in the framework of this thesis.

---

[5] **F**ield-**p**rogrammable **g**ate **a**rray

[6] In a noise spectrum, the baseline differs slightly from channel to channel. The zero values of the individual channels are called *pedestals*.

[7] **GE**M and **Si**licon **c**ontrol and **a**cquisition

[8] **T**rigger and **c**ontrol **s**ystem, see [Gru01] for details

Chapter 5

Noise studies

In this chapter, the noise tests a Silicon detector has to undergo during assembly are described. The assembling procedure itself is sketched and the software for obtaining noise histograms and for lab quality tests is described. General noise performance of the detectors is presented.

Of the four detectors mentioned in this thesis, detector SIL6 was the first detector to be produced. As this detector showed several insufficiencies in its common mode and strip noise performance, it is the main subject of the discussions in this chapter.

5.1 Assembly

After gluing the APV readout chips to the front-end boards with two-component conductive glue, power and readout lines are bonded to the APV. If all chips work, the silicon wafer is glued to the two L-boards with NEE001, a Silicone based glue.[1] This glue is suited for different reasons. It shows good thermal conductivity and elasticity at low temperatures. Moreover, the leakage current over the detector rises less with increasing bias voltage than when using Araldit [Abt97].

Since the pitch of the APV is different from the pitch of the Silicon readout strips, a glass pitch adaptor with etched Aluminum lines is used. The adaptor has to be aligned precisely to the L-board and is then glued to it with Araldit.

---

[1] Detector SIL6 was glued with Araldit 2011, an epoxy based glue. This turned out to be unsatisfactory due to its stiffness; results are discussed in this chapter.

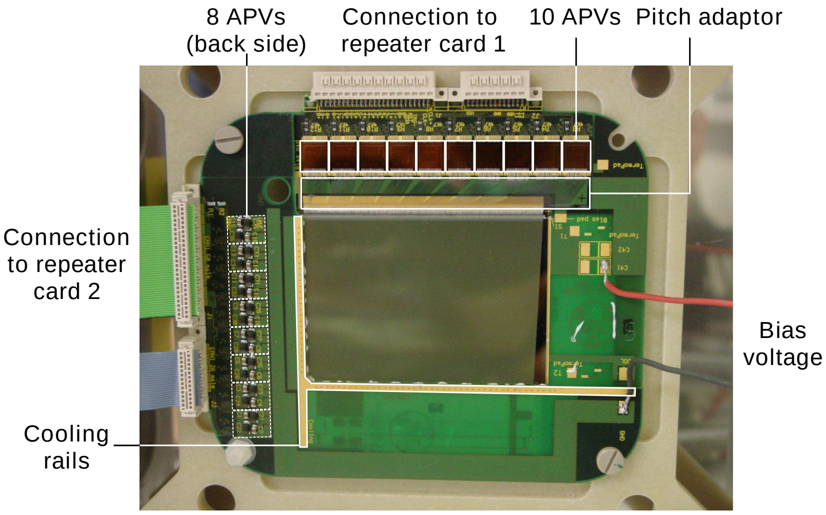

Figure 5.1: Detector SIL8 mounted in the lab. Two L-boards house the APV chips and hold the silicon wafer. On the top, the pitch adaptor between chips and wafer is visible. The detector is mounted on a fiber glass frame to provide thermal insulation from the cryostat in which it will be mounted. The cooling tubes are not mounted on the cooling tubes yet. On the edges of the wafer next to the cooling rails, the gluing points formed of pellets of Silicone glue are visible.

After the APV chips, the wafer, and the pitch adaptor are glued to the L-boards, bonding of the Silicon readout strips to the pitch adaptor and from there to the APV input pads has to be done. While there are 22 bonds necessary for connecting one APV back side (power and output lines), bonding the Silicon to the input pads requires 4480 bonds for each detector. Figure 5.1 shows a detector SIL8 at this production stage.

Finally, cooling tubes have to mounted (This has not done for the detector seen in the picture). These tubes are fixed under the APV chips on the other side of the L-board, and are flushed with Nitrogen during operation to provide temperatures where stable operation of the APV is possible. Due to the bad experience with mounting the tubes in this late stage of production, the production process for further detectors will be optimized in this respect.

5.2 Analysis software

Noise of the setup is measured at different stages during mounting. These measurements are done with a program for GeSiCA readout, employing features like pedestal subtraction and common mode correction. Readout is done via the VME bus. Although with trigger rates of about 10 Hz direct VME readout is quite slow, it is sufficient for noise measurements and proved to be very reliable and easy to

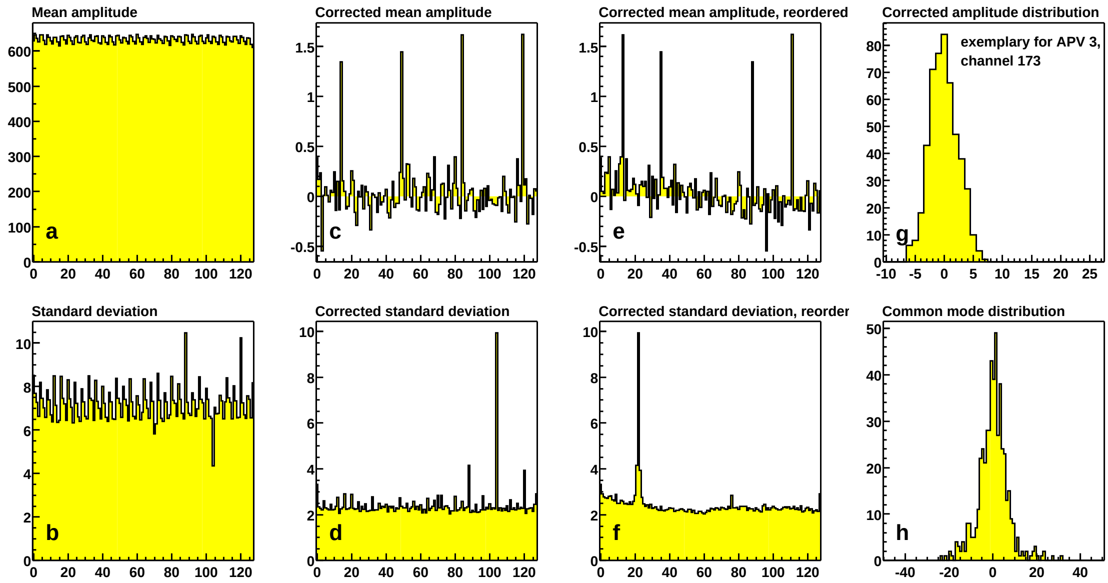

Figure 5.2: Histograms taken with `GeSiCAReader`: a) mean amplitude and b) standard deviation calculated from the raw data, c) mean amplitude and d) standard deviation calculated from pedestal and common mode corrected data, e), f) same but reordered to reflect the geometrical order of the channels, g) amplitude distribution for each channel and h) common mode distribution for each APV front-end chip

set up for lab tests of the detectors and their components. Lab tests in Munich and digitizazion delay tests (section 6.3.6) have been done with `GeSiCAReader`.

`GeSiCAReader` takes measurements in two steps: First, individual *pedestals* for each channel are obtained by averaging channel amplitudes over a certain number of events. The common mode is calculated for each APV chip by averaging over all but the highest and lowest 15 channel amplitudes of this chip and averaging the result over all events. This *median cut* on high and low amplitudes is done to exclude channels which always show high noise ("hot channels") from common mode calculation.

After the pedestal run, a second run is started to create histograms containing relevant information on detector performance. These histograms include the amplitude distribution for each channel and the common mode distribution for each front-end chip. In addition, mean amplitude and standard deviation σ (which characterizes the *noise*) are calculated for every strip from the raw data and from pedestal and common mode corrected data. A sample of the histograms `GeSiCAReader` creates is shown in figure 5.2.

5.3 Tests and quality control

5.3.1 Fingerprints and overall noise performance

After mounting the APV chips and prior to gluing and bonding the silicon wafer, histograms of all mounted chips are taken to ensure that the APVs are working and show reasonable noise. These histograms are referred to as *fingerprints*, since they characterize the noise behavior of each chip individually. Figure 5.3 shows a fingerprint of one APV chip together with the measured noise performance of the completed detector in single-side readout. The electronics produce a noise of $\sigma = 0.71$ (ENC: 284 electrons), which is less than one ADC channel. As soon as the silicon wafer is bonded to the APV, the noise increases to $\sigma = 7.44$. For the fully depleted detector, the noise decreases to a value of $\sigma = 1.96$, equivalent to an ENC of 784 electrons. These numbers have been obtained without the second side of the silicon powered. As soon as both sides are powered, a noise of $\sigma = 2.2$ (fig. 5.4) can be obtained, equal to an ENC of 840. This value is in very good agreement with our estimation of 850 electrons from section 3.4.2.

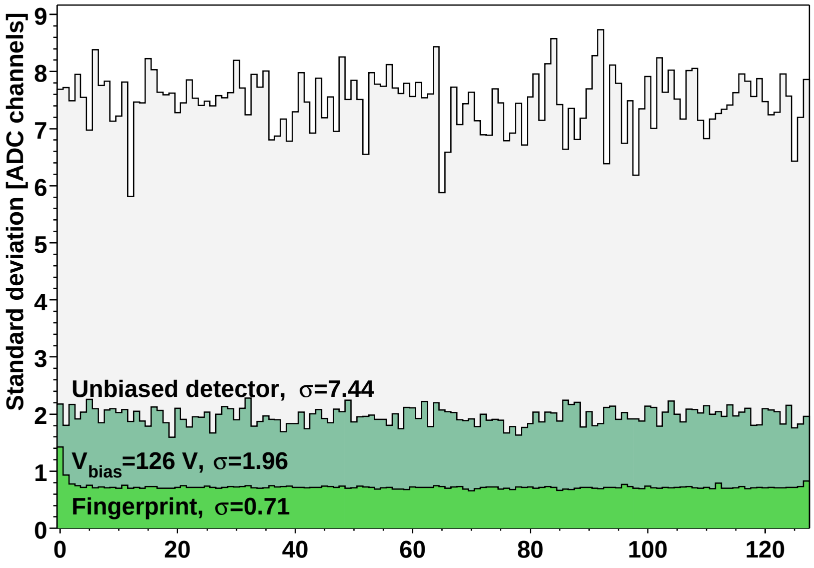

Figure 5.3: Fingerprint and noise histograms of the 128 channels of one APV chip on detector SIL10, taken in single-side readout. The readout chain without silicon wafer produces a noise of σ=0.71. With an unbiased silicon connected, the noise increases to σ=7.44, whereas for a fully depleted detector, a value of σ=1.96 is reached.

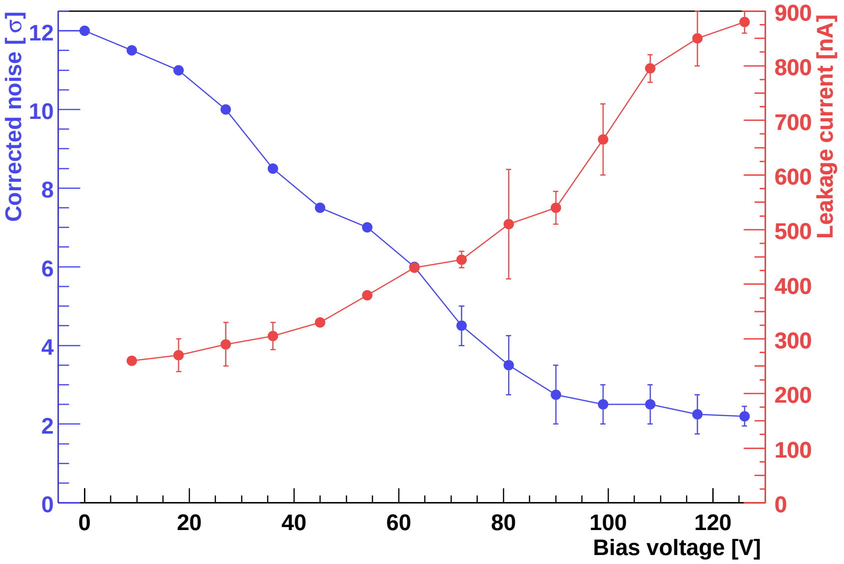

Figure 5.4: Noise performance and leakage current of detector SIL12 with varied bias voltage in double-sided readout. For the plot, the strip noise of all strips has been averaged over the detector. The standard deviation of the strip noise reaches a constant value as soon as full depletion of the detector is reached.

In figure 5.4, bias voltage is plotted against average strip noise and leakage current. The strip noise approaches a constant value from $V_{\text{bias}} = 99$ V on, showing that full depletion of the silicon bulk is reached. The leakage cannot be used as a direct indicator for depletion as we would expect from (3.10), because comparatively large capacitances of 2.4 mF were switched in parallel to the detector, contributing to the total leakage current.

5.3.2 Common mode noise

First systematic studies of the noise performance of a double-sided silicon detector were done in April 2001 with the detector which later on was used in the T11 test beam. Figure 5.5 shows the common mode distribution for detector SIL6 with different capacitances switched in parallel to the wafer for noise reduction. (The silicon itself has a capacitance of about $1.3 - 1.9$ nF.) Additional capacitances damp oscillations which occur between the two readout planes and would give rise to common mode.

While in principle a capacitance as high as possible is desirable, other types than the used electrolytic capacitor react faster to voltage drops. Therefore, apart from a large electrolytic capacitor, additional small capacitances of 1 µF and 100 nF

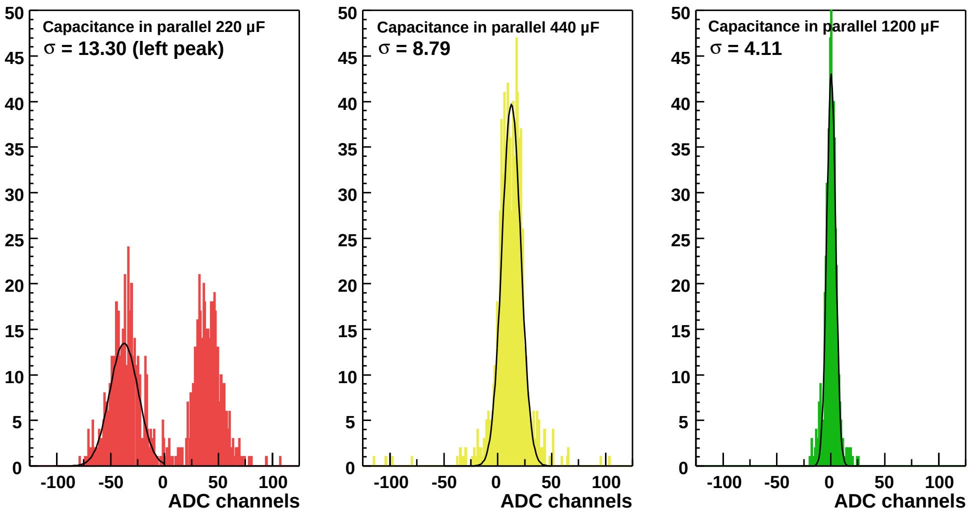

Figure 5.5: Common mode distributions for detector SIL6. The three plots show the common mode for different additional capacitances $C_{\|}$ switched in parallel to the Silicon wafer.

were used. These capacitances were always included in the setup and are not mentioned any more in the following.

With a capacitance of $C_{\|} = 220\,\mu\text{F}$, a broad two-peak distribution is observed, with an overall σ of about 37 channels. The jitter in common mode noise clearly points to some kind of oscillation. As such oscillations were observed with all front-end chips of the detector, the detector as a whole causes the jitter rather than single APV chips.

After doubling the parallel capacitance, the common mode noise distribution becomes much narrower ($\sigma = 8.79$), although the two-peak structure still is faintly visible. When further increasing the capacitance to $C_{\|} = 1.2\,\text{mF}$, a $\sigma = 4.11$ of is reached, which we considered low enough to go into the test beam.

5.3.3 Strip noise performance

While the detectors should show small common mode distributions in order to apply common mode correction algorithms, another important issue is the inherent strip noise performance, which enters in signal to noise ratios and signal height cuts and cannot be corrected.

First noise measurements again have been taken with the test beam detector SIL6. Exemplarily, we will discuss the structures on one of the APV chips on this detector. The histograms in figure 5.6 show the influence of different capacitances parallel to the Silicon on the strip noise behavior.

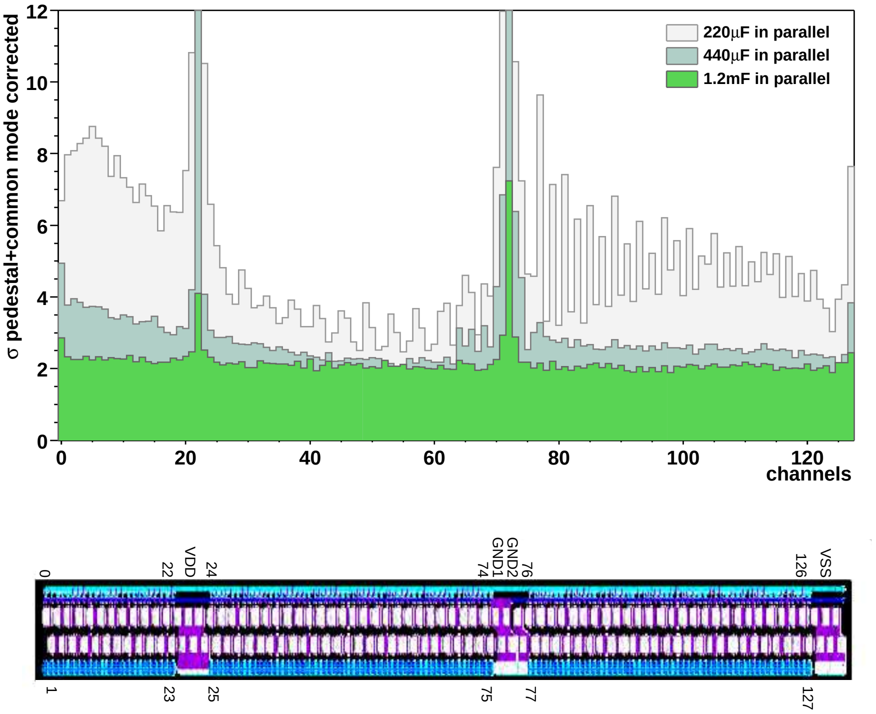

Figure 5.6: Noise performance of one of the APV chips of detector SIL6. The different histograms show the noise for each of the 128 channels of one APV chip for different capacitances switched in parallel to the Silicon. Under the histogram, the bond pad region of the APV chip is depicted. Channels next to the power (VDD, VSS) and ground (GND) pads exhibit high noise.

With a parallel capacitance of $C_{\|} = 220\ \mu\text{F}$, many structures are present on the 128 channels. If the parallel capacitance $C_{\|}$ is increased, the strip noise is reduced considerably. While most of the structures disappear at $C_{\|} = 440\ \mu\text{F}$, a comparatively uniform baseline over the 128 APV channels of $\sigma \approx 2.2$ is obtained with $C_{\|} = 1.2\ \text{mF}$.

Bonding problems. Among the channels with comparatively high noise, the spikes around channels 24, 73 and 127 are most prominent. The bonds corresponding to these channels lie next to the VDD, GND and VSS pads, which provide power supply for the analog amplifiers in the APV chips. High noise is picked up if power/ground bonds and readout bonds are touching. The noise peaks disappeared and reappeared for different runs, very much like the connection of readout and power bonds is not a permanent one.

From channel 25 to 75, every fourth channel has a relatively large noise compared to the neighboring channels. A possible explanation are bonding problems at bonds between the pitch adaptor and the Silicon wafer, where groups of four bonds are done one over another. Bonding is done by a machine, which does all

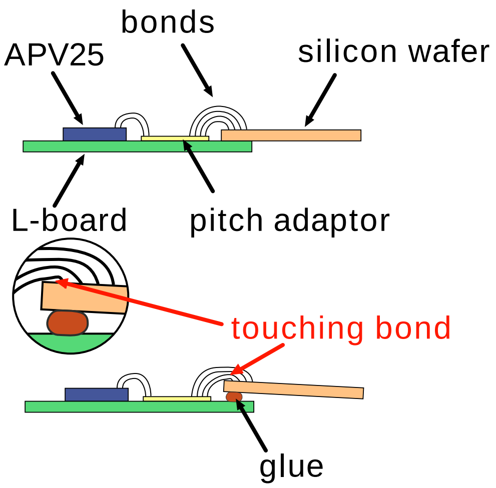

Figure 5.7: Possible bonding problems due to piled-up glue: If a blob of glue forms under the wafer, the bonds easily get skewed and touch the wafer's guard ring structure.

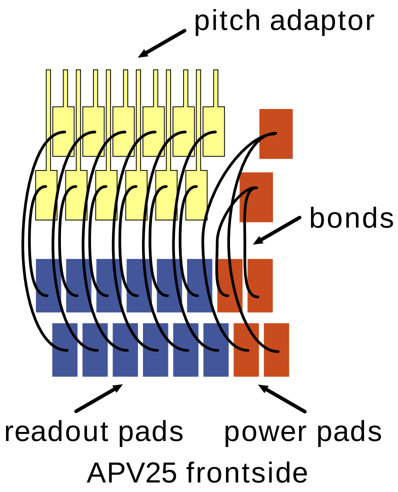

Figure 5.8: Schematic layout of the bonding pads on the APV front side and on the pitch adaptor. Bonds are arranged in pairs, which are bonded one over the other.

bonds with four different wire lengths. The lengths of the wires remain constant for all bonds over the detector length, however. If we assume that the wafer is misaligned with respect to the L-boards as figure 5.7 suggests, the lowest bond touches the wafer near the guard ring and the biasing structure, and may pick up noise there.

In the region between channels 77 and 127, every second bond exhibits high noise. This could indicate bonding problems between APV chip and pitch adaptor. Here (fig. 5.8) bonds are arranged pairwise, so that one bond has to be done over the other. However, this explanation is not as straightforward as the previous one.

5.4 Results and discussion

While the noise measurements discussed in the previous section were done in the lab, in this section results from the detectors in the beam area are presented. Detector SIL6, which had some assembly problems, and was used in a test beam in April 2001 is discussed in section 5.4.1. Results of two detectors produced later on for the COMPASS 2001 beam time are presented in section 5.4.2.

Unfortunately, the four detectors discussed in this thesis differ in properties like their full depletion voltage, their assembly procedure and their operation parameters. Therefore, a direct comparison of the detectors is at least difficult. Table 5.1 summarizes the main differences.

Detector	SIL6	SIL8	SIL10	SIL12
Glue	Araldit	Silicone	Silicone	Silicone
Full depletion voltage	26 V	38 V	84 V	88 V
Operated at V_{bias} of	63 V	99 V	99 V	99 V
Capacitance $C_{\parallel}$	up to 1.2 mF	2.4 mF	2.4 mF	2.4 mF

Table 5.1: Properties, assembly procedure and operation parameters of the four detectors

5.4.1 Prototype detector SIL6

Of the four detectors mentioned in this thesis, SIL6 was the first detector to be produced. This detector had some assembly problems. Due to a design bug, the pitch adaptor broke at one edge, so that the last two chips on the *n* side could not be bonded to the detector. Parts of the bonds of chip 8 on the *n*-side were torn off by the bonding machine, so this chip practically could not be used for readout. While chip 10 was not included in readout, for chip 9 we expect to see noise of an APV not connected to the detector. Chip 1 on the *p* was not powered, because some of the power bonds of these chips were not done correctly. On this chip, pure ADC noise is observed.

Beyond that, problems due to gluing of the silicon wafer were encountered. The wafer is sandwiched between the two L-shaped front end boards and has to be fixed to both of them with glue. In contrast to the assembly procedure described in section 4.2.2, the Silicon wafer of SIL6 was not glued to the L-boards with Silicone glue, but with Araldit. It seems that due to this glue's properties, it piled up under parts of the Silicon wafer. Like that, the wafer became misaligned with respect to the L-boards, resulting in bonds touching the detector surface (fig. 5.7).

Noise performance of the detector. In figure 5.9, histograms showing the noise of each strip (cf. fig. 5.2f) for the complete detector are compiled. The detector was equipped with a parallel capacitance of 1.2 mF and biased with $V_{\text{bias}} = 62.6$ V. For chip 1 on the *p*-side, which was not powered, the pure ADC noise is observed. Chip 10 on the *n*-side was not read out at all.

Most chips (unless not powered) on both sides show a noise baseline given by $\sigma \approx 2.5$. Apart from that, regions of channels with high noise, e. g. on chip 6 and 8 on the *n*-side, as well as many small groups of at most 4 neighboring channels are present. The latter mostly are located around the APV power pads, either touching the power bonds or at least influenced by them. In addition, other effects are observable in the plots.

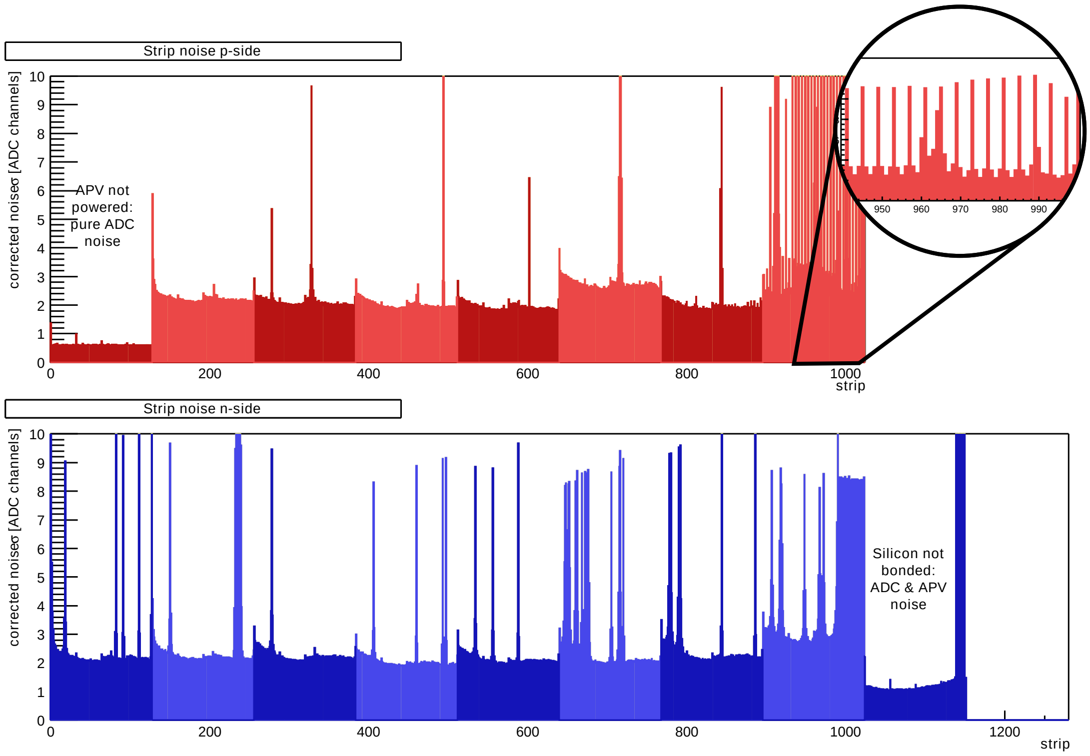

Figure 5.9: Detector noise performance for detector SIL6 at a bias voltage of 62.6 V. Top: p-side. Bottom: n-side. The different tones mark groups of 128 channels, each of which is read out by one APV front-end chip. The first APV chip on the p-side was not connected to the readout chain, so that pure ADC noise is visible. The channels on chip 9 on the n-side were not bonded to the Silicon; there we see APV noise. Chip 10 was not included in readout. Inset: Strip noise of chip 8 on the p-side. Every 4th channel is noisy.

- On the p-side, chip 6 shows a higher noise baseline than other working chips. This is not due to higher noise of the whole chip, but due to a different signal amplification. This means, this chip produces 41.9% higher signals compared to the other APVs, which is visible in the signals originating from this chip as well and has been compensated in analysis. The difference in signal height can be due to an irregularity in the preamplification stage or because of a different termination resistor.

- On chip 8 of both sides, we observe high noise on many channels; in addition, every fourth channel exhibits high noise of $\sigma \approx 9$. This is caused by the misaligned Silicon wafer, as discussed in the previous section.

- Over all channels and chips, in particular on the n-side, we observe several single channels with high noise. This in most cases is due to touching, misaligned or broken bonds.

5.4.2 Detectors SIL10 & SIL12

Figures 5.10 and 5.11 show the resulting noise histograms of the detectors SIL10 and SIL12, which were used in the COMPASS 2001 beam time. Apart from chip 1 on the p-side and chip 10 on the n-side, nearly all chips show uniform baselines, not exceeding $\sigma = 2.5$. In general, the noise performance of the n-side seems to be slightly better than that of the p-side. In comparison to SIL6, the detectors show satisfactory strip noise performance.

On detector SIL10, all APV chips on the p-side have high noise around channel 24, which points to bonding problems near the power pads again. This systematic behavior is absent in detector SIL12. here only few strips show high noise.

The slightly higher noise around channel 64 of every chip of detector SIL10 seems to be an artifact of one of the APV multiplexer stages. This structure can also be observed on detector SIL6 (see previous section), while it is not visible on SIL12. APV chips come in two designs, 0.8 mm and 0.3 mm high. While the chips on SIL6 and SIL10 are from the 0.3 mm batch, SIL12 has been equipped with 0.8 mm APVs.

Some of the higher peaks have been identified to originate from readout bonds touching power bonds, and have been marked accordingly in figures 5.10 and 5.11. It should be possible to separate touching power and readout bonds. In fig. 5.11, two pairs of shortcut readout strips, namely strips 462/463 on the p-side and strips 1157/1158 on the n-side have also been marked. While shortcut strips can be identified, strips with pinholes or low signals cannot be detected by their noise behavior.

Common mode correction. Special attention has to be paid to chips where the common mode correction algorithm based, which is based on all 128 channels of one APV, cannot be applied. Figure 5.12 shows the general layout of the detector. On the p side, the last 56 strips are not connected to the APV, since in the HERA-B design, the readout pads for these strips are provided on the other detector side. Therefore, the APV chips on the p side have been arranged in such a way that the first 56 strips on APV 1 remain unconnected. Hence, the common mode correction for this chip breaks down, since it assumes a common movement of all 128 channels of this chip. Instead of this, the noise of the connected 72 channels will move independently from the 56 unconnected channels, which see only the noise of the readout electronics. In figure 5.12, the noise of the first chip without and with common mode correction is shown. Without correction, the unconnected channels show a noise of about 0.7 ADC channels, like we expect from the fingerprints (section 5.3.1). Starting with the first connected channel, the noise increases gradually to a value of about 2.1 ADC channels.

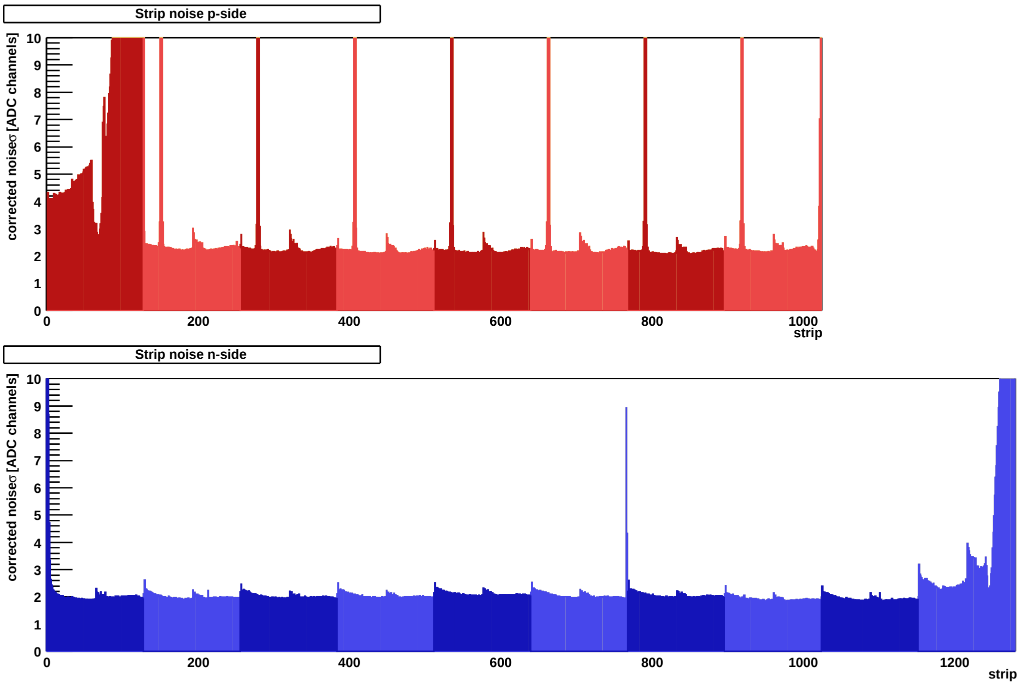

Figure 5.10: Detector noise performance for detector SIL10 at a bias voltage of 99V. Top: p-side, bottom: n-side. The high noise peaks around channel 24 of each chip on the p-side is due to bonding problems at the power pads.

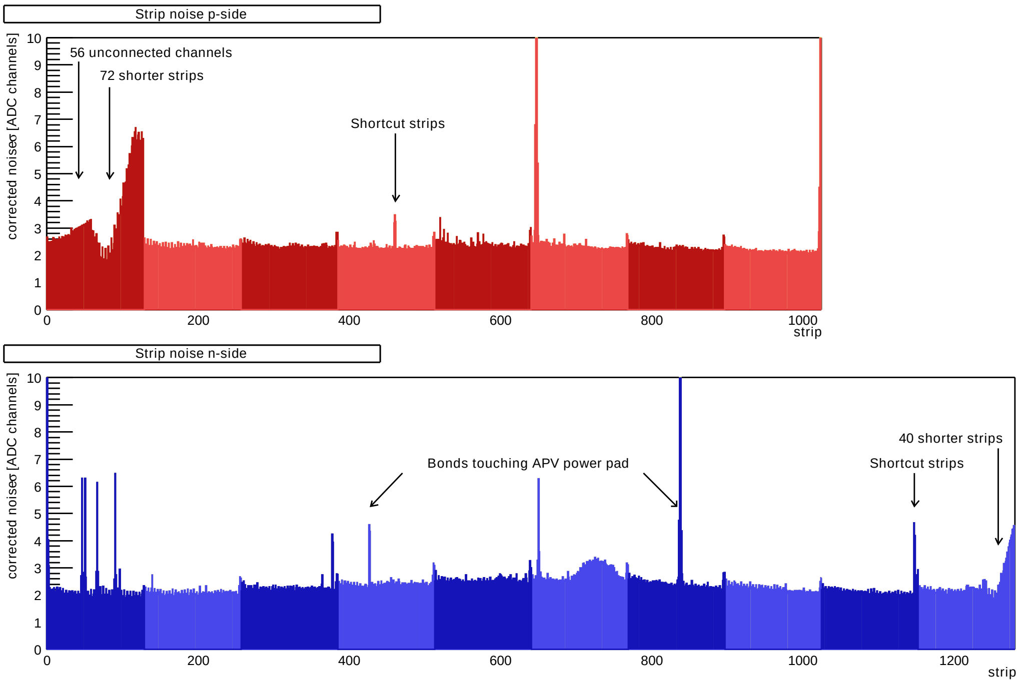

Figure 5.11: Detector noise performance for detector SIL12 at a bias voltage of 99V. Top: p-side, bottom: n-side. Two pairs of strips shortcut during the production process of the wafers are marked. The structures on the first chip on the p-side and on the last chip on the n-side are due to the common mode correction (see text).

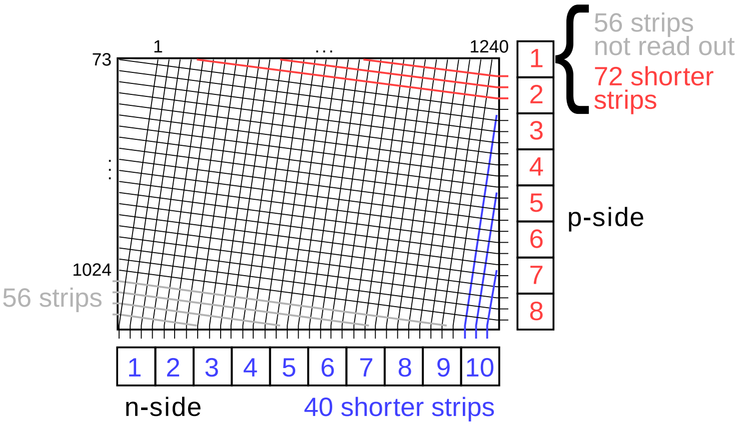

Figure 5.12: Layout of the Silicon wafer and arrangement of the APV front-end chips. Due to the 2.5° inclination angle, the last 40 of the strips connected to APV 10 on the n-side are shorter than the others. On the p-side, the first 56 strips of APV 1 are not connected, while the remaining 72 strips are shorter due to the inclination angle as well. The positions of the 10 and 8 APV readout chips and the numbers of the readout channels are marked with respect to the Silicon detector.

Shorter strips. The gradual increase of the noise is due to the fact that the channels 72…128 are connected to strips which are shorter than the nominal strip length because of the 2.5° inclination angle between strips and wafer. The same effect is observed for chip 10 on the n-side of the detectors. Here, the last 40 readout strips are shorter. The shorter a strip is, the smaller is its noise. This smaller noise is wrongly corrected by the common mode correction algorithm, which artificially lifts in with respect to the other channels on the chip (fig. 5.11). This effect is even more pronounced at detector SIL10 (fig. 5.10), which can be attributed to the fact that that the common mode is higher for SIL10.

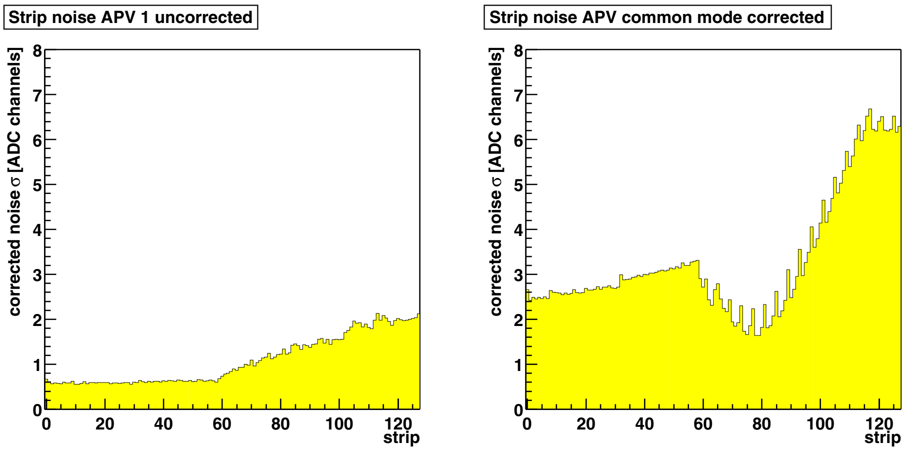

Figure 5.13: Strip noise of APV 1, p-side. Left: Without common mode correction, the unconnected channels show a noise of 0.71 ADC channels, like expected from the fingerprints. On the connected channels, noise increases gradually up to 2.1 ADC channels. Right: Strip noise after common mode correction.

Chapter 6

A double-sided detector in the test beam

In April 2001, one Silicon microstrip detector was installed at the T11 test beam area, located in the PS East Experimental Area at CERN. In this low intensity beam of pions and protons, performance and properties of a COMPASS Silicon microstrip detector with two-sided readout were studied for the first time. In addition, the complete readout chain for Silicon and GEM detectors in COMPASS was available, so that a detector fully equipped with front-end electronics could be read out.

6.1 Test beam setup

6.1.1 The T11 beam line

The T11 test beam is a secondary beam produced from 24 GeV/*c* primary PS protons impinging on a 250 mm Aluminum target. The maximum proton intensity on the production target is $2\cdot 10^{11}$ particles per pulse, with a beam spill length of 300 to 400 ms, and typically 1 to 2 spills in the 14.4 s PS super-cycle [Dur93]. The beam line optics only select particle momentum, so that different particles were present in the secondary beam, namely $3.5\cdot 10^{5}$ positive pions, $3\cdot 10^{5}$ protons, muons from π^0 decay, as well as kaons ($\approx 3\cdot 10^{3}$) and positrons ($\approx 3\cdot 10^{3}$) from pair production (fig. 6.1, 6.2). The secondary particle momentum was set to the maximum momentum possible, 3.6 GeV/*c*. The theoretical momentum resolution of the T11 beam line optics is 1.9%.

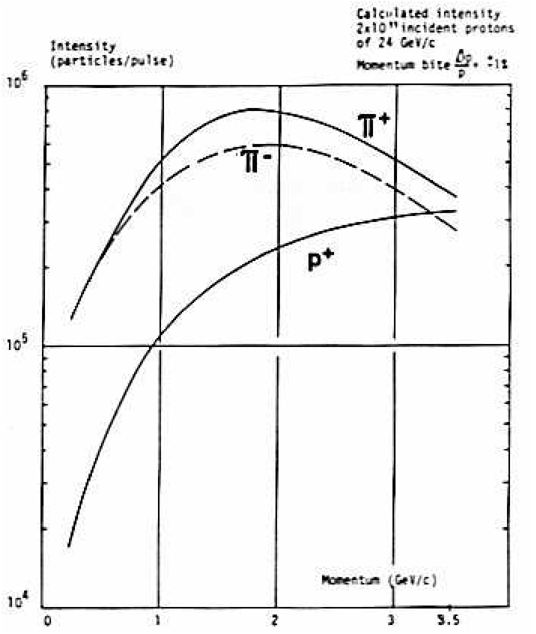

Figure 6.1: Calculated particle intensity at the reference focus of the T11 beam [Dur93]

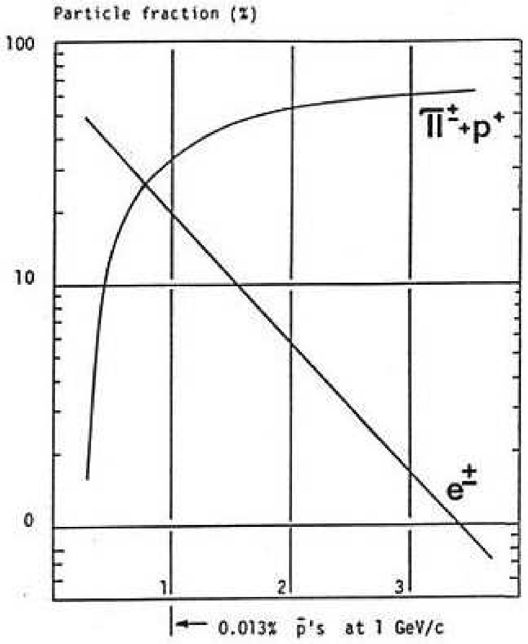

Figure 6.2: Observed particle fractions in the T11 beam [Dur93]

6.1.2 Trigger setup

For trigger definition, a system of three scintillators read out with photo diodes was used. Two of them (SC1 & SC2) were placed upstream of the detectors, covering an area of 10×10 cm^2. An additional small scintillator finger SC3 of about 5×2 cm^2 was installed downstream of the detectors. The trigger was generated by a coincidence of either all three scintillators or only the two big scintillators. The latter mode was used for large area scans for GEM detector tests, whereas the full set of scintillators in the trigger coincidence allowed to illuminate the Silicon detector only partially. For a more explicit description of the trigger setup, see [Sim01].

6.1.3 Detector setup

Unlike in the preceding test beams, where detectors only partially equipped with readout chips were used with prototype ADCs, in this test beam a detector equipped with the full number of 18 APV readout chips was installed. Due to problems during assembly, one chip on the p-side and two chips on the n-side could not be used, so that the remaining 8 + 7 chips allowed an active area of

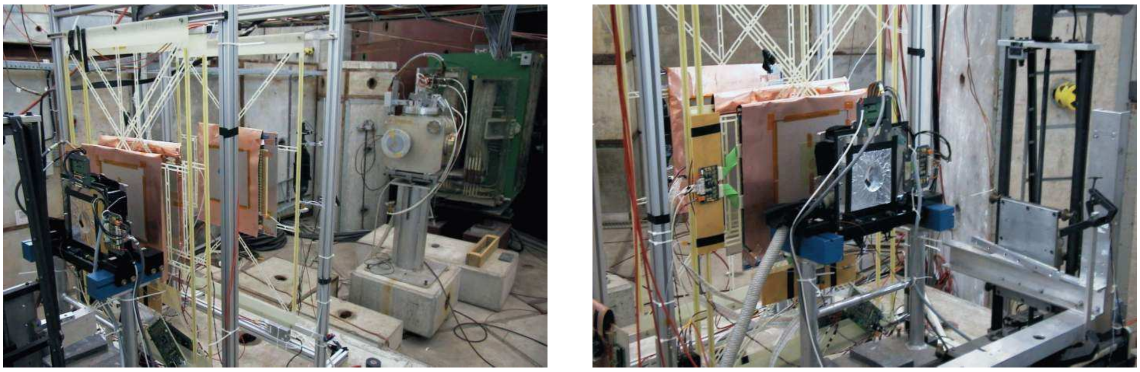

Figure 6.3: Pictures of the setup in the test beam area. Left: The doublet of scintillators is installed right upstream of the first GEM detector. Right: To the very right, the small downstream scintillator finger is visible.

$56 \times 43.75\ \mathrm{mm}^2$ to be read out. This set no constraints on the test beam measurements, which aimed mainly at the overall and noise performance of a double-sided Silicon microstrip detector and the complete readout chain.

The detector SIL6 was mounted in a new cryostat made of stainless steel (cf. section 4.2.2), which had been designed for the beam stations in the COMPASS beam line. Although these cryostats are suited for cooling the detector down to temperatures of liquid nitrogen, in T11 it was only used as support structure. Instead of cooling, only a moderate air flux for refreshing the electronics was applied.

Due to the mounting, the readout strips on the n-side had an inclination of 2.5° with respect to the vertical, while the strips on the p-side were inclined by 92.5°, respectively.

Apart from SIL6, the detectors TGEM10 and TGEM11 were installed in the test beam. With the help of SIL6, tests of the spatial resolution and efficiency of these detectors could be done. The geometrical setup and location of the scintillators used for triggering is shown in figure 6.4.

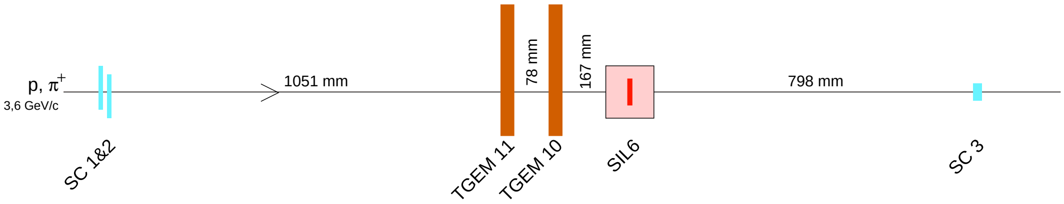

Figure 6.4: Geometrical setup in the T11 test beam area

6.1.4 Data acquisition

Readout was done with the complete readout chain for Silicon and GEM detectors in the COMPASS experiment. The DATE data acquisition software [DAT00] is responsible for collecting the front-end data via optical link from GeSiCA, for eventbuilding and writing the data to disk. These data contain strip amplitudes, event numbers and sizes, as well as GeSiCA, ADC and front-end chip IDs, allowing equipment identification. DATE prepends this data with useful headers containing event type, event sizes and unique equipment IDs.

In April 2001, zero suppression and common mode correction was not implemented in the ADCs, so for each event the full detector information had to be read out by the DAQ. Thus, in order not to overload the readout chain, only a moderate trigger rate of 1k triggers/spill could be chosen.

Online and basic offline analysis of the data stream was performed with `gemMonitor` [Ket01], a program written by B. Ketzer which reads, decodes and analyzes APV data interfacing the DATE data stream. Decoding includes mapping of the individual front-end IDs and the strip amplitudes onto the right detector projections. As Silicon microstrip detectors and GEM detectors use an identical readout chain, `gemMonitor` is suited for analyzing Silicon data with only minor modifications, which are discussed later.

For analysis purposes and to reduce the amount of data, `gemMonitor` applies zero suppression and common mode correction algorithms to the data. Reduction in this respect means that for each event a maximum of 25 strip numbers per projection with the corresponding amplitudes and noise for these strips is extracted from the data. This vector of 25 strips contains the five strips with the highest amplitudes found, accompanied by the two adjacent strips on each side of these strips. These five groups of strips are candidates for cluster finding algorithms applied later on. Since analysis is done with the help of ROOT [Bru01], an object-oriented data analysis framework developed at CERN, relevant histograms for analysis as well as a ROOT *tree*[1] are written to file after processing. The tree comprises strip numbers, amplitudes, and noise of the hit candidates.

---

[1] In this context, a tree is a data structure organized like a *ntuple*. A ntuple is a collection of tuples, a tuple is a set of numbers. In general, a tree is a generalized structure not only to store numbers, but any kind of objects.

6.2 Online data analysis

6.2.1 Trigger timing

A fundamental prerequisite for analysis and in fact for seeing signals at all in the data is the right trigger timing. To form and distribute the trigger to the detector, time is needed. Upon arrival of the trigger at the detector, the cells in the circular buffer of the APV have to be read out which contain the information from the time of the particle's transit. In this respect, the latency (section 4.3.1) is the time one has to subtract from the time of the trigger arrival to find the pipeline cell which contains the corresponding signal. The latency setting is stored in one of the APV's registers. To find the right latency, a systematic scan is started with a value at which the signals are expected. A rough estimate yields:

Detector hit → Scintillator signal	Time of flight, 80 cm	≈ 2 ns
Scintillator signal → TCS controller	Cable, 48 m	160 ns
TCS controller, encoder, receiver	Logics, synchronization	≈ 75 ns
TCS server → TCS receiver	Optical fiber, 100 m	500 ns
GeSiCA → ADC	Optical fiber, 50 m	250 ns
		987 ns

The latency can be set in steps of 25 ns. A reasonable starting point for a *latency scan* is a value of 975 ns. In figure 6.5, different latencies are plotted against mean pulse height. The rising edge of the signal is short, while the falling edge is rather long. To obtain precise timing information, it is advisable to set the latency register to a value at which the rising of the signal is observed.

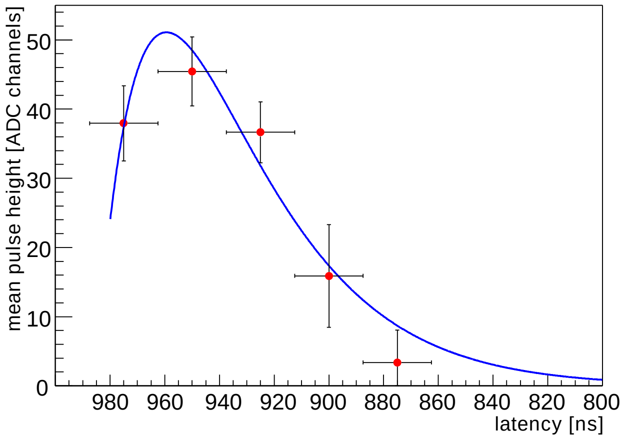

Figure 6.5: Latency scan at T11. Different latencies are plotted against mean pulse height. The plot shows the APV response to the Silicon signal, which is a convolution of the signal itself and the shaping function of the APV.

6.2.2 Bias voltage adjustment

Prior to performance analysis, an optimal value for the bias voltage has to be found. This is an optimization problem. As we have seen in section 3.4.1, the full width of the charge cloud generated by a passing particle is only about 20 μm when it arrives at the readout plane. It is advantageous to have cluster sizes larger than the width of one readout strip, as only then the spatial resolution can be increased by calculating the center of gravity. Therefore, a bias voltage as low as possible should be chosen, to enable the charge cloud to spread as much as possible during drifting to the readout strips. Nevertheless, full depletion of the detector has to be maintained for a high signal amplitude and an optimal signal/noise ratio.

Depletion of the Silicon bulk. With the right latency selected, it is interesting to see the depletion of the Silicon bulk for different bias voltages V_{bias} applied to the detector. As a measure for depletion, the mean value of the Landau distribution can be used, like it was done in figure 6.11 on page 71. For the Silicon used in our detector, SINTEF states a voltage of $V_{\text{bias}} = 26$ V [Ber97] at which the Silicon bulk should be fully depleted. The plot shows how the signal gets saturated from about 45 V on. A closer analysis of signal and noise dependence of bias voltage is given in section 6.3.4.

6.2.3 Channel exclusion

For the T11 analysis, all channels with noise higher than 3 ADC channels were not taken into account in the analysis. To exclude dead strips, a minimum noise of 0.4 ADC channels after common mode correction was demanded. In addition, channels that permanently give signals were ignored.

The detector SIL6 had comparatively many channels with high noise (section 5.4.1). Of the 7 APV chips read out on the *p*-side, 13 channels had to be excluded from readout, plus nearly all channels of chip 8, while on the *n*-side, exclusion was necessary for 137 channels of chips 1–8. APV chips 9 and 10 were not read out there.

Concerning the region interesting for analysis—the scintillator shadow—on the *p* side 141 out of 896 channels were excluded, while for the *n*-side, 25 out of 350 channels were not read out.

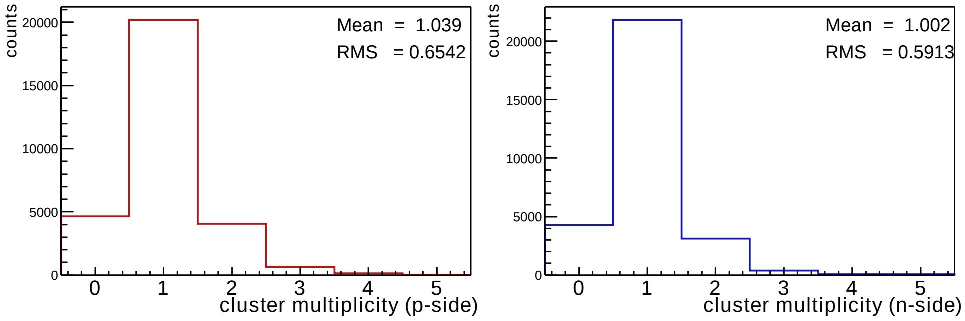

Figure 6.6: The cluster multiplicity is the number of clusters found on the readout plane. If a trigger is received but the corresponding particle crosses the detector in an inactive area, it is possible that a cluster multiplicity of 0 is generated. Left: p-side, Right: n-side.

6.3 Data analysis

6.3.1 Cluster finding

The charge summed up over one cluster equals the charge generated by a passing particle. Thus, for analysis an algorithm for finding charge clusters extending over more than one strip is used, which was developed by B. Ketzer. This peak search algorithm assumes that a Silicon cluster is not be bigger than three channels. The strip signals are required to lie more than $3\sigma_{\text{noise}}$ above noise, while the cluster has to be $5\sigma_{\text{noise}}$ above strip noise, where σ_{noise} denotes the r. m. s. noise. If clusters contain more than one strip, the cluster center is calculated as the center of gravity, using the effective signal height (amplitude minus noise threshold) for every strip above threshold.

6.3.2 Cluster size analysis

Cluster multiplicity. To see how many clusters are present in one event, the cluster multiplicity has been plotted in figure 6.6. With the low particle flux in the T11 beam, we expect a multiplicity of the order of one. On both coordinates, 15% of the events have a cluster multiplicity of 0. This is because particles seen by the scintillator finger are lost for readout in dead areas of the detector, due to strips excluded from readout or not powered front-end chips.

On the p-side, where the readout strips are inclined by 92.5° to the long scintillator side, 15.7% of the strips are not read out. On the n-side—the readout strips are parallel to the scintillator finger apart from the 2.5° inclination angle of the silicon—all relevant strips in the scintillator shadow are read out.

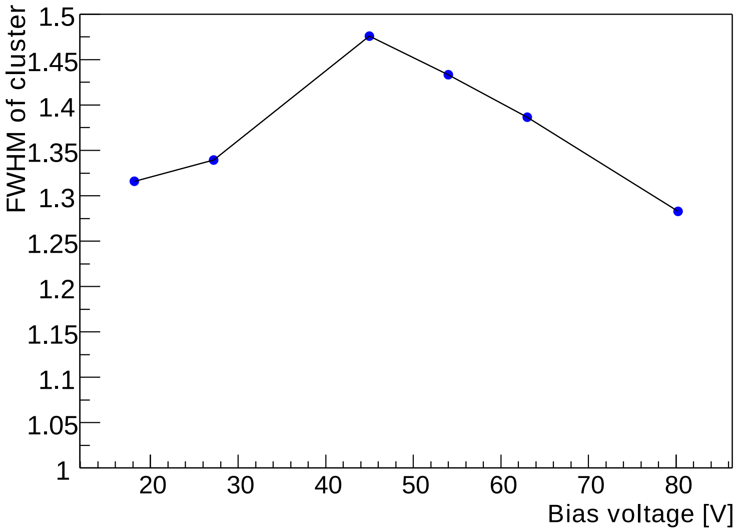

Figure 6.7: Cluster size scan: Bias voltage applied to the detector against the FWHM of a Gaussian fitted to the cluster.

Cluster size for different bias voltages. Figure 6.7 shows the FWHM of the cluster size for different bias voltages. On the rising edge of the curve, the width of the charge cloud is increasing with the total number of charge carriers generated, as the size of the depleted zone increases. For voltages over 45 V, the decreasing drift time is dominating the width of the charge cloud when arriving at the readout strips. Bias scan and the cluster sizes at different bias voltages suggest to choose a bias voltage of about 50 V for optimal operation.

Cluster size and FWHM. For a run with nominal conditions, cluster size and FWHM are plotted in figure 6.8. With a mean size of 1.685 strips, the clusters on the p side are in average broader than the n-side clusters (1.475 strips). Since the p side has intermediate strips for capacitive charge coupling, we expect a bigger cluster size than on the n-side, where such additional strips are not present. Like expected, we hardly get clusters spreading over more than three strips. Still, a considerable number of hits permit using the center of gravity method to increase spatial resolution. We find:

Cluster width	p-side	n-side
1	40.2%	57.9%
2	52.2%	37.6%
3	5.8%	3.4%
4	1.2%	0.8%

To see how the charge is distributed over the cluster, the average charge in units of σ_{noise} is plotted in figure 6.9. The plots have been generated by summing up all events and normalizing to strip noise and event number. Only contributions

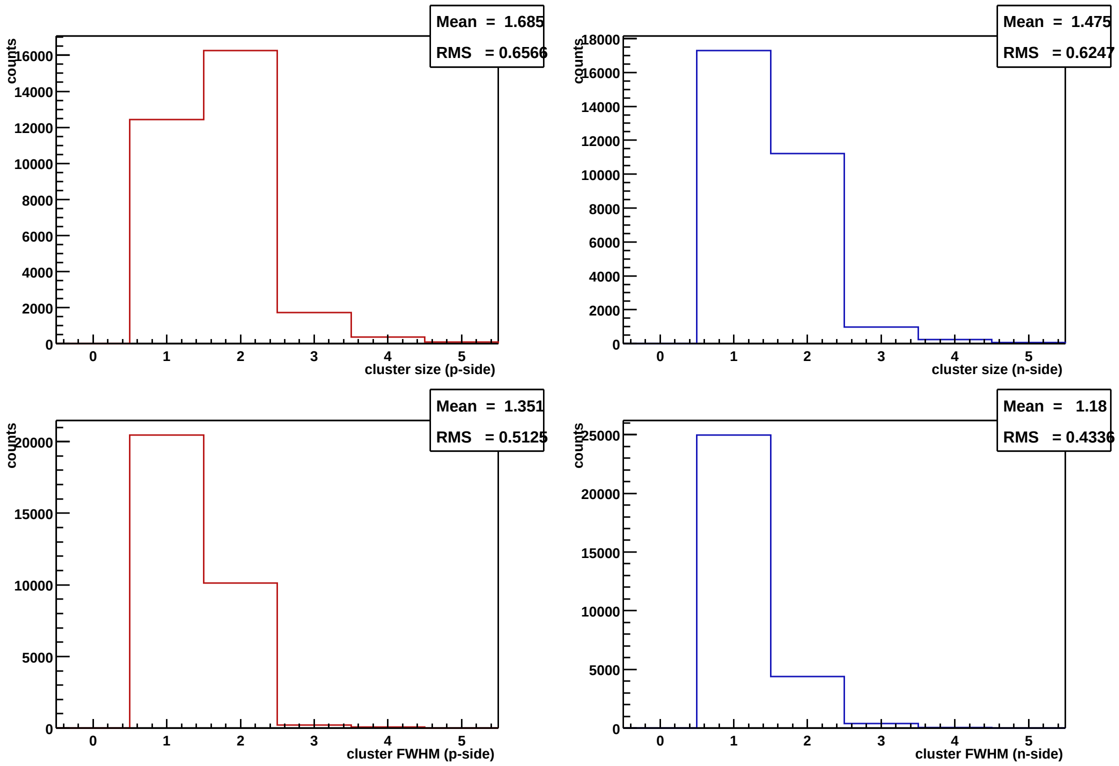

Figure 6.8: Cluster width. The measurements were taken with a bias voltage of 63 V.

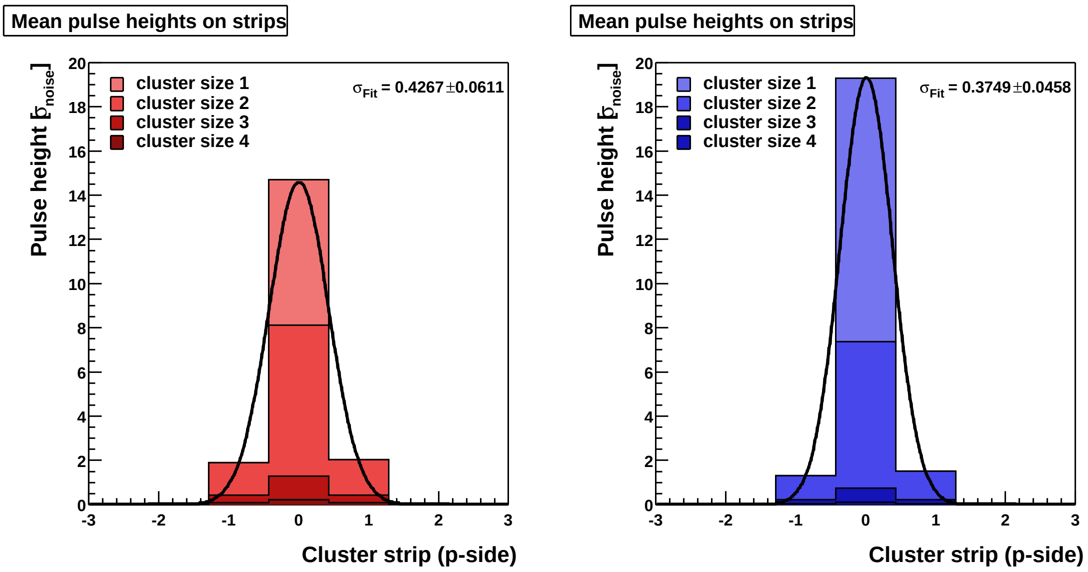

Figure 6.9: Mean pulse height on strips. For each cluster, strips exceeding a $3\sigma_{\text{noise}}$ threshold have been filled in the histograms. The plots have been normalized to the total event number. The contributions of single- and multi-strip events can be distinguished.

above noise level have been taken into account. The color code in the histograms allows to distinguish entries from events with different cluster widths. Since the strip with the highest charge in these plots is the central strip per definition, for e. g. cluster width 2 we obtain entries in the bins –1 or 1.

As an important result, the symmetry of the histograms shows that for multi-strip clusters, the cluster charge is equally distributed over the cluster. Moreover, we notice that it is very unlikely that the strips not directly adjacent to the central strip in the cluster show signals. Their pulse height is too small, as it is not exceeding the typical detector noise of 2.5 ADC channels. The difference in the total (integrated) charge of p and n-side is discussed in section 6.3.4.

6.3.3 Geometrical properties

The hit map given in figure 6.10 gives some idea of how the detector was positioned in the beam. It was generated using single-hit events, i. e. events in which exactly one hit in each of the two readout planes was found. Consequently, for each hit an unambiguous position can be obtained. The plot includes cluster charge projections for the two detector sides. For clusters with more than one hit strip, the cluster position was calculated using the center of gravity method. From the three samples given for three different timings, always the last sample, denoted by a_2, was used, since the trigger timing was adjusted in a way that a_2 showed the highest amplitude. For the calculation, the effective signal height $(a_2^{(j)} - 3\sigma)$ is taken for every strip above threshold j in the cluster:

$$x_{\text{cluster}} = \frac{\sum_j (a_2^{(j)} - 3\sigma^{(j)})\, x^{(j)}}{\sum_j (a_2^{(j)} - 3\sigma^{(j)})}. \tag{6.1}$$

Since triggers were defined by a coincidence of all three scintillators, the shadow of the small scintillator is visible in the hit map. Regions without hits within the scintillator shadow are due to the exclusion of noisy strips and hot strips[2]. Furthermore, the inclination of the detector strips with respect to the scintillator finger is visible. From the rising and the falling edge of the scintillator shadow on the n-side charge projection, the inclination angle can be calculated to be $2.56^\circ \pm 0.13^\circ$.

---

[2] strips which always give signals

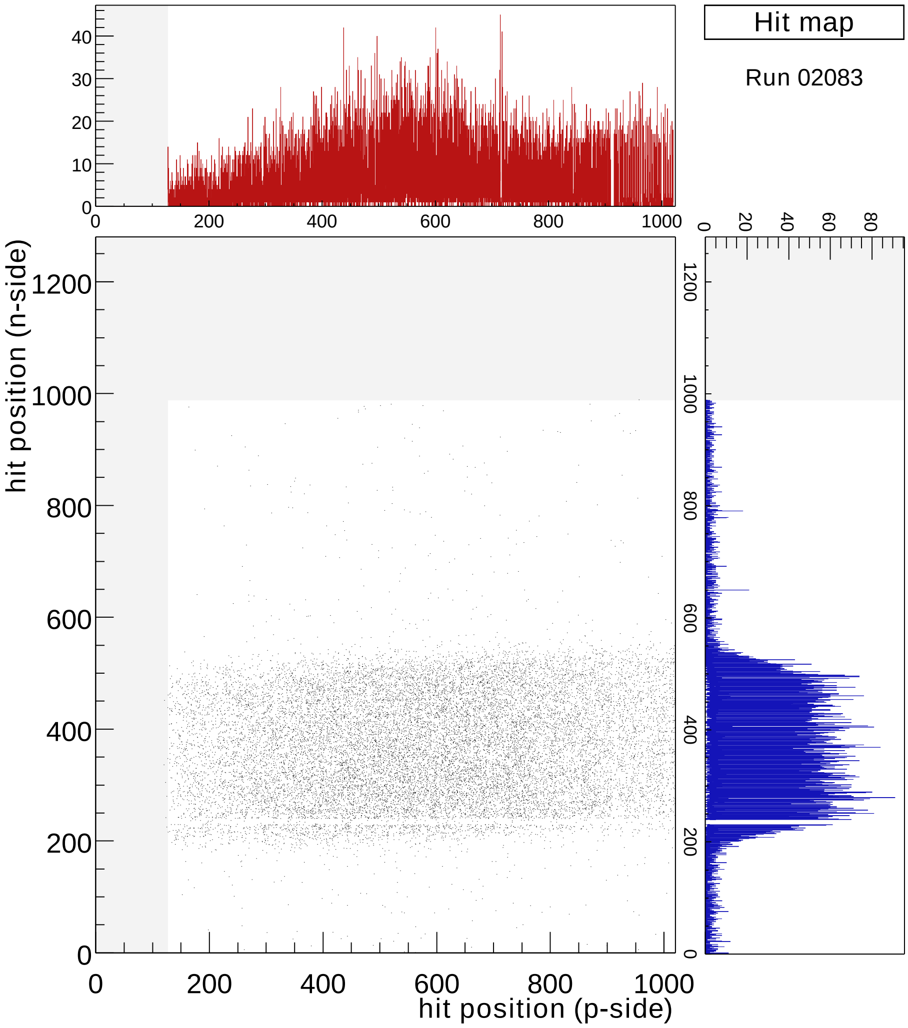

Figure 6.10: The hit map shows the geometrical locations of single hit events. The red and blue histograms show the cluster charge distribution on the two projections. The cluster center has been calculated using the center of gravity method, where applicable. The gray area in the hit map marks front-end chips which were completely excluded from analysis.

6.3.4 Signal/noise ratio

In the preceding beam tests for COMPASS Silicon detectors, the detectors were read out only single-sided. In these tests, signal/noise ratios (SNR) of 28 were reached [Wie00], a value the results presented in this section have to be compared with.

As Silicon clusters tend to be very small (usually not more than 2, at most 3 strips), the SNR is usually defined by dividing the total charge collected in one cluster by the noise on one strip. Accordingly, to calculate the SNR, the most probable value of the Landau signal distribution is divided by the mean value of the Gaussian noise distribution.

In figure 6.11, the cluster pulse height distribution is given for both detector sides. A Gaussian fit to the strip noise is also included in the plots. From the fits to the data, we find

p-side:	SNR=23.61	cluster signal: $1.9\cdot10^4$ h^+	strip noise: $8.0\cdot10^2$ h^+
n-side:	SNR=25.80	cluster signal: $2.1\cdot10^4$ e^-	strip noise: $8.2\cdot10^2$ e^-

Assuming that the n-side sees about 93% of the nominal signal (cf. section 6.3.6), and the most probable number of generated electron-hole pairs for the T11 beam in 300 μm Silicon is $2.3\cdot10^4$, the number of electrons per ADC channel is about 390. For the noise, we get ENC values of about 820, matching the estimates given in section 3.4.2.

For both sides in the signal distribution, the small noise peak is clearly separated from the real signal. Thus, a noise cut to the signal is easily applicable.

While for the n-side the SNR is comparable with SNRs found for single-side readout, the SNR for the p-side is about 15% lower. The reason for this is unclear. In the primary process, the same number of electrons and holes are created, no matter if the detector is fully depleted or not.

Dependence on bias voltage. Cluster signal and strip noise amplitudes have been plotted against bias voltage separately in figure 6.12. For the cluster signal, the mean value of the Landau distributions has been plotted. For the strip noise, the width of a Gaussian fitted to the noise distribution is given.

The signal amplitudes rise with increasing bias voltage, to reach a plateau at about 70. . . 80 V. Although the slope of the amplitude is about the same for both n and p-side, the p-side amplitude is about 15% lower than the n-side amplitude.

The noise on the p-side stays the same for all bias voltages, because the detector gets depleted starting from the p-implants. As the depleted zone extends to the n

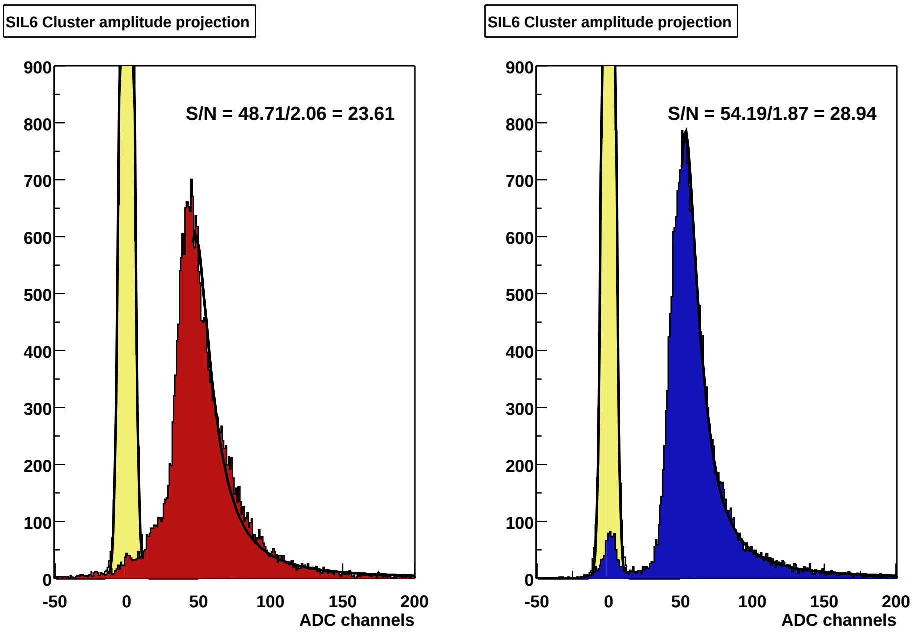

Figure 6.11: Cluster amplitude and strip noise distribution for detector SIL6 Left: p-side, right: n-side. The plots were done with 54 V bias voltage applied. The plots combine cluster amplitude and strip noise histograms.

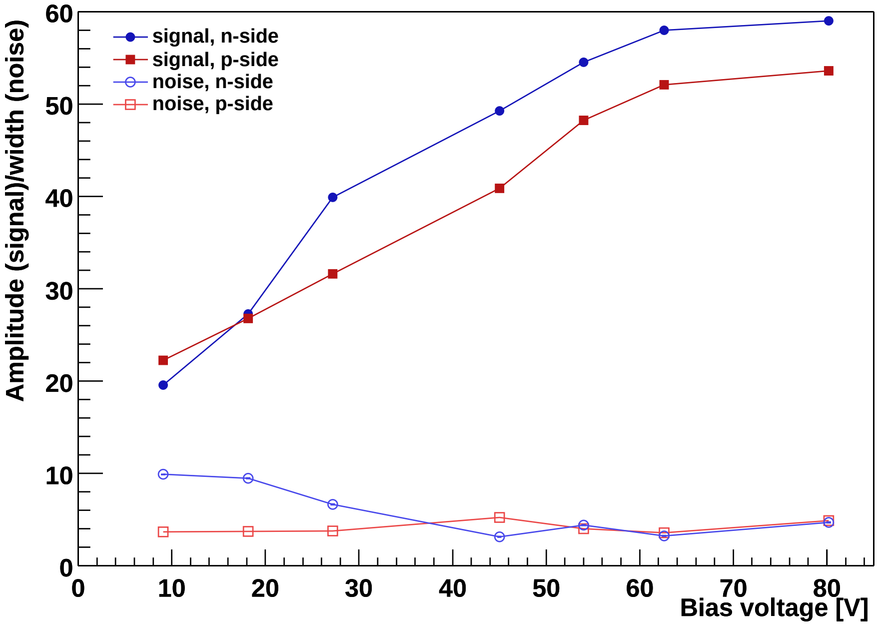

Figure 6.12: Cluster signal and strip noise for different bias voltages for detector SIL6. The values for the p side are plotted in red, those for the n-side in blue. The upper two curves represent the peak position of the Landau distribution of the signal amplitudes, the lower lines the width of the Gaussian fitted to the noise amplitude distribution.

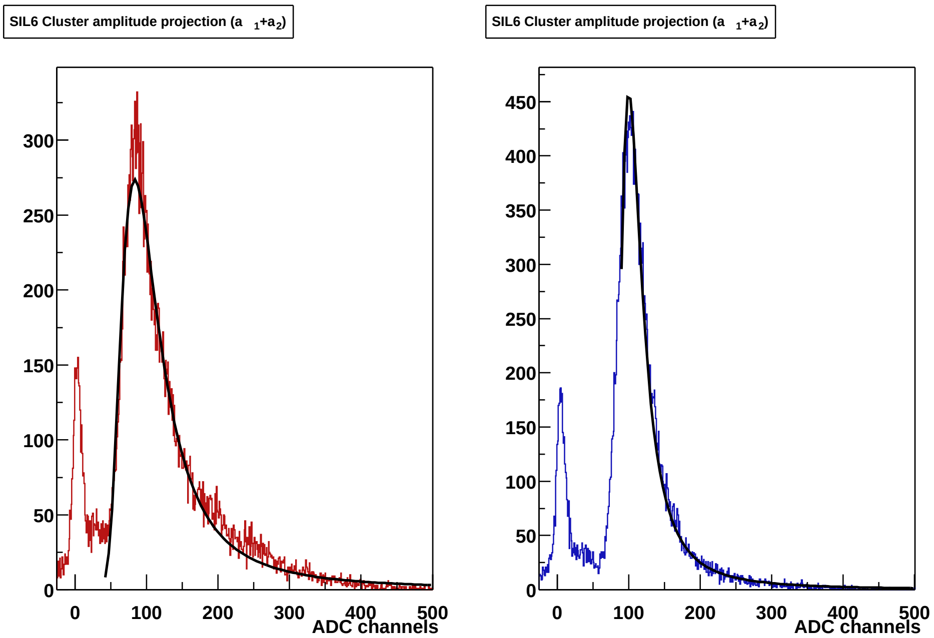

Figure 6.13: Signal form for two added samples. Two of the samples obtained in the APV's multi-mode can be added. While the signals add linearily, the noise should only add quadratically. Left: p-side, right: n-side.

side with increasing bias voltage, noise on the n-implants decreases. An indication for complete depletion is the parallel evolution of the noise of both detector sides from 54 V on.

Multi-mode. The signal of a particle hit is read out in three consecutive samples in multi-mode. If a trigger timing is chosen at which two of these samples see a sufficiently high signal, this can be used for improving the SNR. While the signals in the two samples are correlated and add linearily, the corresponding noise should not be correlated, so that it adds quadratically only,

$$SNR(a_i + a_{i+1}) = \frac{a_i + a_{i+1}}{\sqrt{\sigma_i + \sigma_{i+1}}} \approx \frac{a_i + a_{i+1}}{\sqrt{2}\sigma}, \tag{6.2}$$

with a_n the amplitude in the nth sample and the noise σ. However, the assumption of uncorrelated noise is only a good one for strip noise, not for the common mode. In figure 6.13, two samples of the signal were added. The maximum of the Landau distribution has moved, while the gap between the trailer of the noise peak around zero has grown, so that a noise cut is more easily applicable.

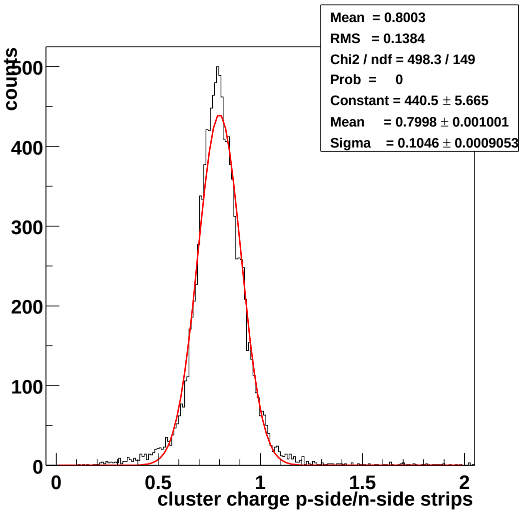

Figure 6.14: Cluster charge ratio

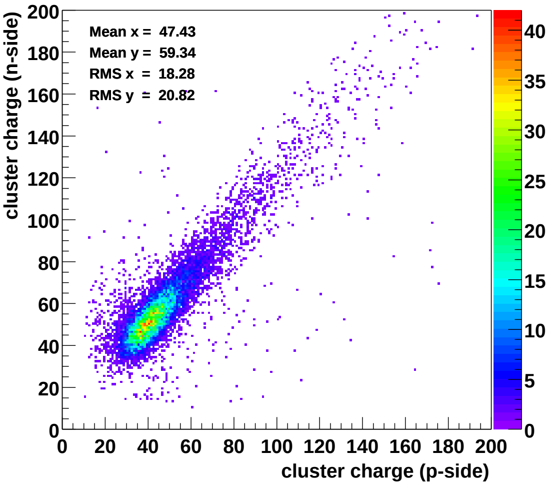

Figure 6.15: Cluster charge correlation

6.3.5 Cluster charge correlation

The COMPASS data analysis routines are based on *projections*, which means that basically the hit correlation between the two detector planes is not crucial to disentangle multi-hit events. Nevertheless, the correlation between the two detector sides is interesting to study, as both readout sides should see the same charge. To see how good the correlation between p and n-side is, the plots discussed in the following have been generated using single hit events only. From the different signal heights for p and n-side we expect the cluster charge ratio to deviate from 1. In the test beam runs, a cluster charge ratio of $0.8 \ldots 0.87$ was observed (figure 6.14).

We get the same picture in the cluster charge correlation, given in figure 6.15. The correlation is peaking at the most probable values of the cluster signal distributions. The distribution of the cluster charge correlation is centered around a line with slope 0.8, which is the cluster charge ratio.

Since in the correlation plot most of the events are contained in the peak, while not many of them are found in the Landau tails, the correlation can practically not be used for disentangling multi-hit events.

6.3.6 Delay of digitization time

As the APV outputs the signals of its 128 channels serially, the analog signal of each channel is present at the ADC input for a time of 51.44 ns, while digitization takes place at a certain point within this time window. To digitize at full signal height and at the same time not to collect cross-talk from the preceding or succeeding channel, it is important to fine-tune the digitization point of time.

Clock and trigger lines arriving at the ADC card are distributed to the connected APV chips. As the ADC works with the same clock and trigger signals the APVs see, its clock and trigger lines have to be delayed to account for the time the trigger signal needs to reach the APVs and data are returned by the APV. The delay can be set by writing to an register on the ADC, where one unit of delay is equivalent to a time of 250 ps and has to be added to the built-in delay of 12 ± 2 ns.

Delay scan. A delay scan obtained with a cable length of 320 cm between ADC and APV is shown in figure 6.16. It was done by looking at an APV synchronization pulse (tick), which ideally covers the whole dynamical range of the APV and has a width of one channel. The plots show how the point of time at which digitization takes place scans over the 51.44 ns tick signal. At the edges, a part of the signal is collected in the adjacent channel, resulting in cross-talk and a smaller digitized amplitude in the nominal channel. Since the ADC synchronizes on the ticks, as soon as the adjacent channel collects more charge than the nominal channel the ADC regards it as the "new" channel to synchronize on.

The plots show how the edge of the tick signal is passed at delays of 17.5 ± 0.5 ns and again at a delay of 69.5 ± 2.5 ns, resulting in a calculated signal width of 52 ± 2.5 ns. For this cable, a total delay of about 44 ns seems advisable for optimal operation.

Impact on the T11 data. Figure 6.17 shows the reconstructed pulse form of the APV tick as the ADC sees it. The correct delay setting can be found somewhere on the plateau of the pulse, whereas in the T11 test beam a setting marked by the red circles was used. The circle around 13.5 ns indicates that in average 7% of the signal was wrongly digitized and thus assigned to the preceding ADC channel, while only 93% of the signal were read into correct ADC channel.

Since digitization was done right at the edge of the signal, the amount of charge going to the neighboring channel is subject to variations. Due to the APV multiplexer, the lost signal is not digitized in the geometrically adjacent channel, but in the succeeding channel after multiplexing. Hence, results of test beam data analysis sensible to signal heights—like the signal timing analysis—were corrupted.

25 ns readout. Currently, the readout chain is operated at a frequency of 19.44 MHz (cf. section 4.3.1). Digitization is done with the same frequency. In the long-term planning, it is planned to double this frequency, which means that the APV25 samples will not be present at the ADC for 51.44 ns, but only for 25.72 ns each. As the signal plateau in figure 6.17 is very flat and uniform, another result

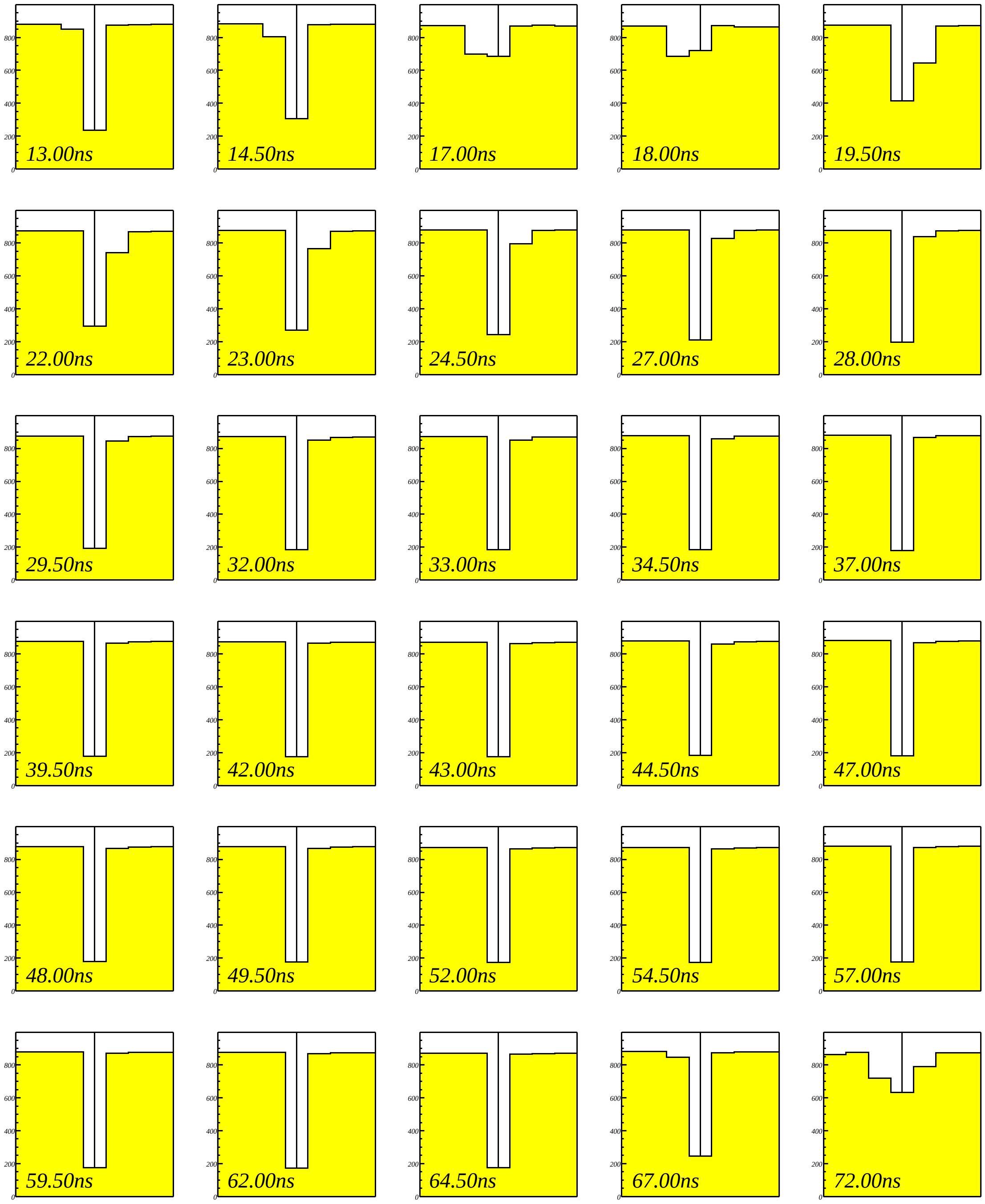

Figure 6.16: Delay scan for 320 cm cable distance between ADC and APV. In the histograms, seven ADC channels centered around one channel containing an APV synchronization tick are plotted against signal height. Total delay times are given in the histograms. The point of time at which digitization takes place scans over the 50 ns tick signal. At the edges of the signal, a part of it is collected in the adjacent channel, like at a delay of 17 ns and again at a delay of 72 ns.

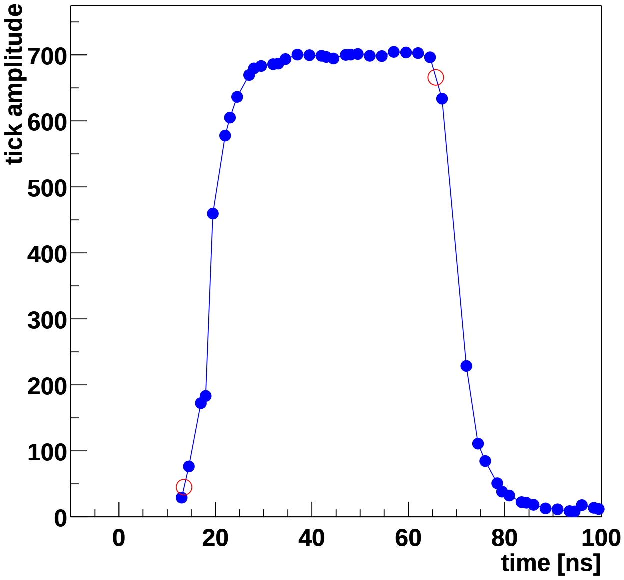

Figure 6.17: Shape of an APV synchronization pulse, as seen by the ADC. The red circle at 65 ns indicates the delay setting at which the ADC was sampling in the T11 test beam, while the other red circle at 13.5 ns gives the signal which was wrongly sampled in the preceding channel

of the delay scans is that switching to 38.88 MHz readout seems quite feasible from the signal form point of view.

6.3.7 Signal timing studies

Method. To gain information about signal timing, the characteristic time evolution of the signal is exploited. Therefore, the APV25 chip is operated in multi-mode, which, when triggered, allows to read out three consecutive amplitude samples of the signal 25 ns apart. The goal of timing analyses is to reconstruct the time evolution from the given three samples, and, of course, as soon as the signal form has been studied, to construct a mapping from the three samples to the exact timing of the corresponding event.

Due to the shaping amplifier of the APV chip, the signal rises in about 50 ns and fall in a time of about 200 ns (fig. 6.5). Due to the short rise time, the rising edge is very sensitive to the signal timing. Rather than absolute amplitudes, ratios of the three signal amplitudes are considered [Fri01], since only the signal form is important for the timing analysis and one wants to become independent of the total pulse height.

We denote the earliest sample taken by a_0, the other two by a_1 and a_2, respectively.

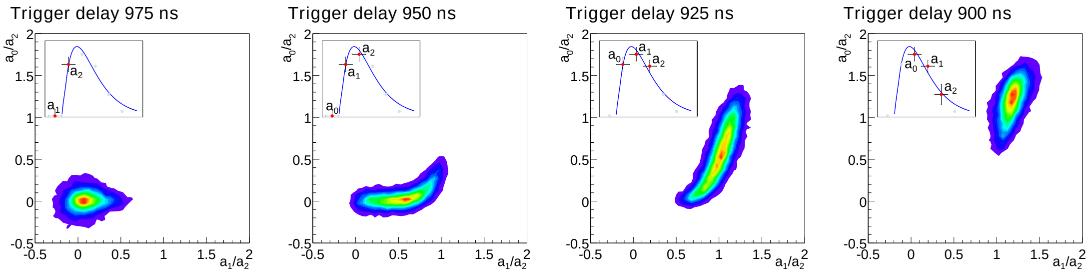

Figure 6.18: Speed plots for different trigger delays at T11. For a given trigger timing, each of the four plots show the ratio of cluster samples, while the positions of the three samples on the Silicon signal is given in the inset. While it is expected that the plots show a rather sharp curve, they are rather blurred.

To look at the rising edge of the signal, we require the trigger to be delayed so that a_2 is taken right behind the peak of the pulse ($a_0 \leq a_1$, $a_0 \leq a_2$, and $a_1 \approx a_2$). As a_2 has a comparatively large value, it is advisable to normalize the other two amplitudes to a_2 to gain a stable denominator.

Figure 6.18 shows the quantities a_1/a_2 and a_0/a_2 plotted in a two-dimensional histogram for different latencies, starting "in front" of the signal, i. e. too early. As long as the three samples are taken too early, all amplitudes are zero and the events are filled around $(0|0)$. When sample a_1 (and a_2) cover the rising edge of the signal, a_1/a_2 increases and the events move along the a_1/a_2-axis. As soon as a_0 starts seeing the signal, the entries in the plot start moving upwards. Since the form of the curve in the plots is characteristic for the rising time and falling time—for the "speed" of the signal—they sometimes are referred to as *speed plots*.

Timing studies for the T11 beam. In low intensity beams like the T11 test beam, most of the detected particles are on time, i. e. we expect to see a narrow bunch of events within the plot's plane on the curve given by the pulse shape. As triggers arrive synchronously with the TCS clock and thus asynchronously with the real hit, we expect this peak to be broadened in a 25 ns range resulting from this time jitter. In high intensity beams, the ratio of pileup to on-time hits should increase dramatically, leading to entries all over the curve within the plot. For such environments, knowledge where to expect on-time signals will be necessary to decide which hits to accept and which ones to reject.

The speed plot for a T11 test beam run is shown in figure 6.19. The signal is peaking between the samples a_1 and a_2, since a_1/a_2 is in the range $0.5 \ldots 1.5$. Since the signal rises very fast, only few events in the 25 ns window still have $a_0 = 0$. To relate the position in the plot to a certain signal timing, a sharp curve is necessary, which is not given with the broad distribution observed in the T11 beam. The broader the curve, the bigger are the variations in the signal form.

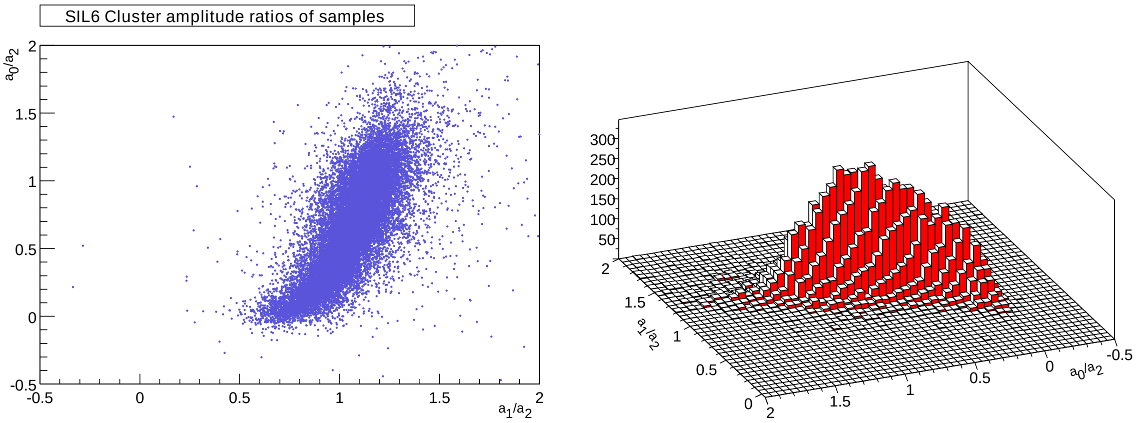

Figure 6.19: Correlation of cluster amplitude ratios for determining the signal timing for the T11 beam. Since the distribution is very spread, no precise timing information can be obtained from these data.

For a precise signal timing, the curve in the speed plot should feature a fast rising edge. Since the speed plots obtained in the test beam do not fulfill this criterion, they cannot be used to determine the precise hit timing. Before the digitization time delay analysis presented in section 6.3.6 was done, the reasons for this insufficient performance were not clear. Since it was not understood whether the blurring of the distribution in the plot was caused by additional noise sampled by switching from one-side to two-side readout, by a reduced overall performance of the detector or by mistakes in the analysis, closer investigations had to be done.

Correlations with tracks. For creating the plots, up to now we only required the cluster amplitude to be above a signal threshold of 5 ADC channels (central strip) and 3 ADC channels (adjacent strips). To see if "good" hits also show insufficient timing behavior, a plot of hits was made which requires tracks correlated to the hits passing the detector. Such hits were selected using the two GEM detectors also installed in the test beam and FASTTRACK, a software tracking tool for the test beam data developed by F. Simon [Sim01].

Figure 6.20 shows a plot done with the conventional cuts for Silicon and a plot created with a cut requiring hits to be part of a track going through all three detectors in the test beam. Apart from some minor contribution of events showing a high amplitude in the first sample (a_0) with conventional cut, the two plots show similar behavior. This means the analysis did not mix up events and noise, and the bad signal form is intrinsic to the data.

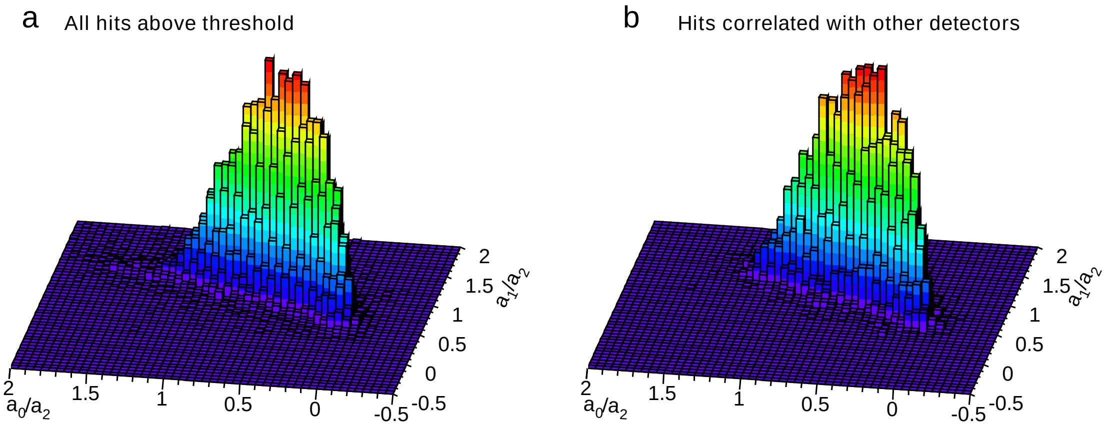

Figure 6.20: Correlation of of cluster amplitude ratios for a) hits fulfilling the conventional Silicon signal cuts and b) hits correlated with other detectors.

6.4 Summary

Detector SIL6 was a compromise in some respects. It was not glued with Silicone, but with Araldit, and many strips could not be read out due to bonding problems or high noise. Many of the results of the analysis could be brought on line with these features. The unstable signal form, preventing timing analysis, was traced back to a wrongly set digitization time delay. Main properties like the signal/noise ratio, or cluster size could be studied. The difference in signal height for the two detector sides could not be thoroughly explained.

Chapter 7

COMPASS 2001 muon run

In the 2001 beam time, the installation of three Silicon detectors as beam telescopes in front of the COMPASS target was planned. Due to various difficulties in commissioning of new front-end electronics, problems with the noise performance had to be solved. This chapter summarizes the steps taken to reduce the electronics noise.

As soon as the detectors were at an acceptable noise level, commissioning of one detector in the COMPASS beam line and inclusion in the central COMPASS DAQ was possible. Analysis of detector data is presented, focusing on the signal timing performance and on first results with the new electronics and sparsified readout.

7.1 The M2 beam line

The M2 beam is the CERN high-intensity muon beam. It provides the COMPASS experimental hall with a high-intensity tertiary muon beam in the momentum range of 60 to 190 GeV/c with fluxes of up to $2 \cdot 10^8$ muons per SPS cycle [Gat00, Gat01]. A secondary hadron beam with a momentum between 40 and 280 GeV/c at a maximum flux of 10^8 hadrons per SPS cycle is also available.

Layout. A 400 GeV/c primary proton beam is extracted from the SPS and directed onto the primary target. The proton intensity is in the range between $2 \cdot 10^{12}$ and $1.2 \cdot 10^{13}$ protons per SPS cycle. From the target, a secondary beam is either transported directly to the experiment (in the case of the hadron beam), or tertiary muons are selected. This is done by a 600 m long pion and kaon decay channel, at the end of which the remaining hadrons are stopped in a 9.9 m Beryllium hadron absorber. The remaining muon beam is shaped in terms of spot size

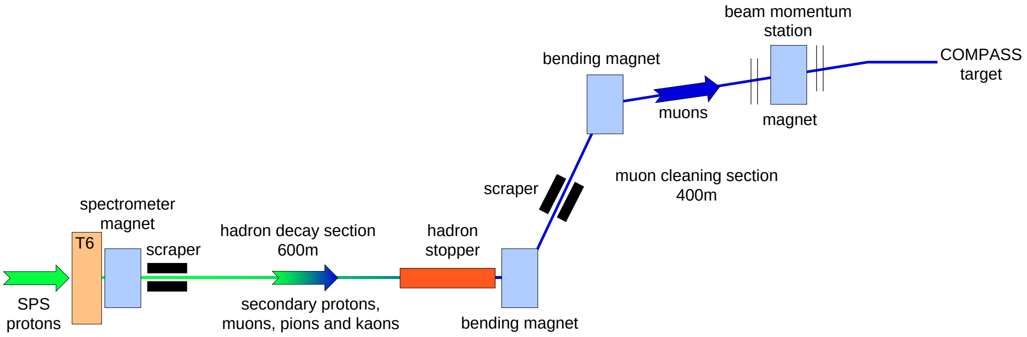

Figure 7.1: Layout of the M2 beam line. SPS protons hit the T6 production target. After the 600 m pion and kaon decay channel and a hadron stopper, only muons are left. In the 400 m muon section, the beam is shaped and cleaned [Nie00]

and divergence in the 400 m long muon section. A schematic layout of the M2 beam is shown in figure 7.1.

For 190 GeV/c muons, typical spot sizes at the target are 7 mm RMS in the horizontal plane and 8 mm RMS in the vertical plane, with a divergence of 0.5 mrad RMS in the horizontal plane and less than 1 mrad RMS in the vertical plane. The momentum accuracy is $\Delta p/P < 3.7\%$.

7.2 Commissioning

Commissioning of the Silicon detectors was done in different steps. The position where the Silicon was supposed to be installed was occupied by a target loading platform until the middle of August. As soon as the platform was removed, cabling and installations were started.

7.2.1 Electronics

GeSiCA and ADC. Until mid-September, the Silicon was operated with the same electronics that were used in the T11 test beam and in the lab. This proved to be difficult, as GeSiCA required switching to the experiment trigger at the beginning of a run. This feature was not implemented in the COMPASS DAQ for Silicon. Therefore, it was decided to wait for the new version of front-end electronics, which was about to be commissioned.

The main new feature of version 2 of the ADC is its capability to do zero suppression, as discussed in section 4.4.2. Version 1 was a prototype which could only be read out in latch-all mode. The GeSiCAs had to be updated with new connectors, since with the new ADCs I^2C configuration signals are not sent over separate fibers any more, but are transmitted over the same fibers the data are read out. This reduced cabling and decreased the time that is needed for loading the ADCs considerably. As soon as stable readout conditions in latch-all mode were reached with the new electronics, the implementation of zero-suppression algorithms was started. Zero suppression was available from the beginning of October on.

Repeater cards. Apart from the new ADC, a new version of repeater cards was also introduced. This version featured minor modifications in functionality, including the possibility to send a reset signal to the APVs via I^2C protocol and additional connectors for temperature measurements. Main design changes include a simplification of the layout, so that no crossing lines are necessary anymore on the PCB board. In addition, a thinner PCB was used.

7.2.2 Noise problems

After switching to the new readout electronics, a very high common mode was observed on the detectors. The distribution (fig. 7.2a) is non-Gaussian with broad tails, spreading over a range of over 200 ADC channels. The broadest distributions observed had a RMS of 37.29. Although it in principle is still possible to apply common mode correction algorithms in this case [Gru01], such broad distributions point to problems with the detector which ought to be debugged.

Since the readout chain is common to GEM and Silicon detectors and the problem was not observed with the GEMs, it was clear that some Silicon-specific equipment had to be responsible for the high common mode. The common mode distribution showed no oscillations as with the T11 detector (cf. section 5.3.2). To reduce noise, the capacitors switched in parallel to the Silicon were moved into the cryostat, to have them as near as possible at the detector. In addition to the black plastic foil, the entrance windows for the beam were covered with metallized mylar for electrical shielding, and a grounding of one of the two detector sides was added to the cryostat inside the cryostat. This led to small improvements (fig. 7.2b–c): The distribution got smaller, but the tails were still there.

In addition to being Silicon-specific, the problem had not been observed with the old electronics. The new repeater cards were a first possible candidate for a source for the high noise. Systematic tests with single-side readout showed that as soon as the repeater card on the other detector side is connected to the silicon, the common mode already increases considerably (fig. 7.2c–d).

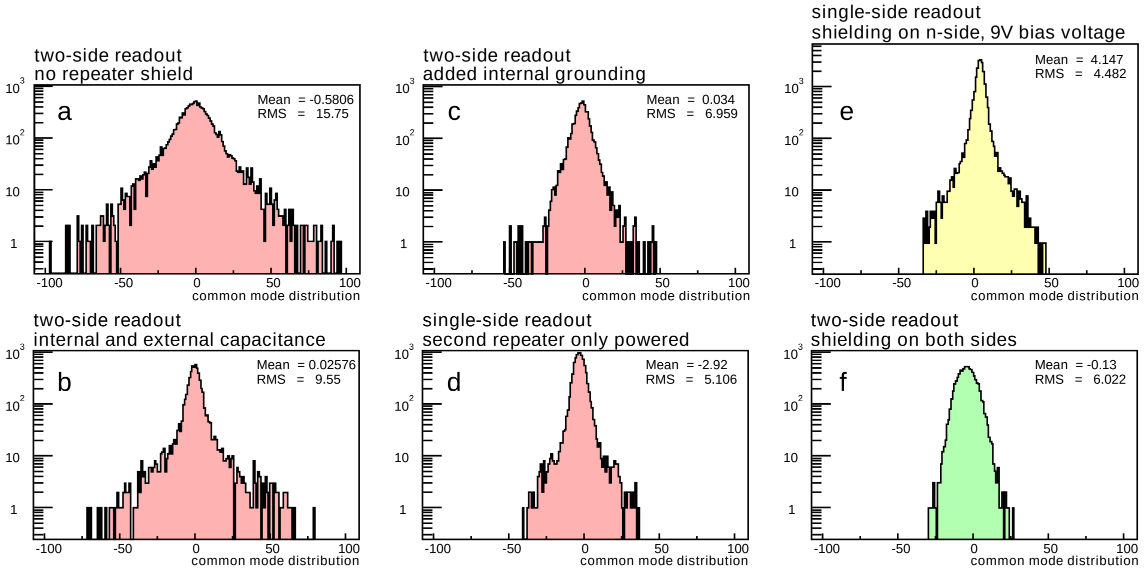

Figure 7.2: Different common mode distributions. a) basic situation: broad distribution b) one capacitance moved into the cryostat c) added internal grounding d) chips on other side powered, but not loaded e) additional shielding on one side f) shielding on both sides

Shielding the repeater boards from their environment by a copper-coated mylar foil or a cage made of a metal mesh proved to further decrease the common mode width (fig. 7.2e). When mounting the shielding to both repeater cards, the tails of the common mode distribution disappeared and the distribution became Gaussian (fig. 7.2f). A common mode distribution with a full width of about 50 and a RMS of about 6 could be reached.

Reasons for the high common mode connected with the new electronics still have to be investigated. Nearly all components of the front-end electronics—ADC, repeater cards and L-boards—were subject to design revisions. Nevertheless, after systematic tests it turned out that the repeater card on the respective opposite detector side introduces the common mode.

The APV chips are very sensitive to noise on their power lines. At the moment it seems that as soon as two repeater cards are connected to the detector, oscillations on the power supply of one card are transmitted via the capacitance of the detector (fig. 7.3). As soon as they are picked up by the APV chips on the other side, they give rise to the high common mode. By increasing the capacitance parallel to the Silicon, the connection to the other side is stabilized and oscillations which cause the noise are damped. In addition, the shielding of the repeater cards seems to be crucial, as it prevents them from acting as antennae for noise pickup. While not being fully investigated, it seems that the antenna-like behavior of the repeater cards can be related to the thinner PCB used.

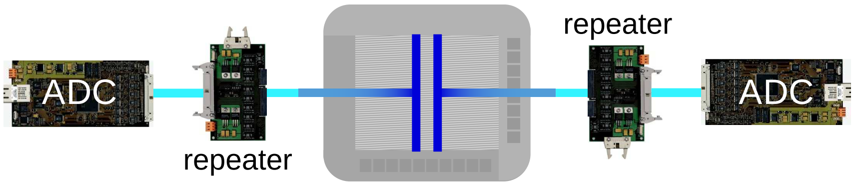

Figure 7.3: Noise induced by the second detector side

Applying mylar foil or a metal cage as a repeater shielding is quite a difficult task, since the non-grounded side of the detector with its repeater card lies on the potential of the bias voltage with respect to the ground potential, which is present at the cryostat's surface. During debugging, a discharge happened to detector SIL10 and the 8 APV chips on the p-side stopped responding to I^2C accesses. To what extent the electronics have been damaged is still to be looked into.

7.3 Data analysis

As a result of the problems with the common mode noise and the availability of new electronics, it was not possible to have more than one detector in the COMPASS beam at one time. Analyses of the T11 test beam could be repeated and the performance of the detector in a high-intensity beam could be studied.

Since zero suppression had not been implemented in the readout electronics from the beginning of the beam time on, the first runs were taken with latch-all readout. Therefore, the number of triggers per spill (4 sec) had to be reduced to about 2.5k by introducing an artificial dead time of 1600 µs. This is necessary in order not to overload the Silicon readout chain with too high data rates.

7.3.1 Signal height and distribution

Expected signal form. For relating signal height to ADC channels, and for comparison to the T11 data, let us calculate the expected energy loss for the beam particles. While the T11 beam to a good approximation contains 3.6 GeV/c protons and pions with a ratio of 3.5 : 3, the M2 beam consists of 160 GeV/c muons. The Bethe-Bloch formula (3.1) for the respective beam energies (fig. 7.4) yields differential energy losses of

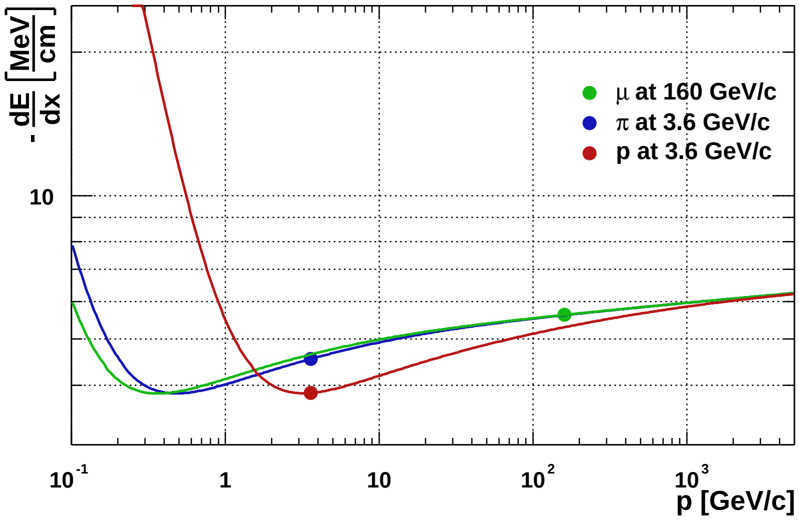

Figure 7.4: Mean energy loss of pions, protons and muons in Silicon. The points mark the relevant particle energies of the T11 beam (protons and pions) and the M2 beam (muons).

$$\begin{aligned} -(\mathrm{d}E/\mathrm{d}x)_{\mathrm{p}} &= 3.85\,\mathrm{MeV/cm}, \\ -(\mathrm{d}E/\mathrm{d}x)_{\pi} &= 4.55\,\mathrm{MeV/cm\ and} \\ -(\mathrm{d}E/\mathrm{d}x)_{\mu} &= 5.622\,\mathrm{MeV/cm}. \end{aligned}$$

While the protons may to a good approximation still be regarded as MIPs, this is not the case for the pions and the muons. Since the energy loss in Silicon is very small compared to the beam energies, the integration of the Bethe-Bloch formula can be approximated by multiplication with the Silicon thickness D:

$$\Delta E_{\mathrm{mean}} = \int_0^D \frac{\mathrm{d}E}{\mathrm{d}x}\mathrm{d}x \approx \frac{\mathrm{d}E}{\mathrm{d}x} \cdot D. \tag{7.1}$$

The results for 300 μm Silicon are given in table 7.1. The Landau distributions in figure 7.5 for the M2 muon beam and the T11 beam were calculated according to (3.4). Since in T11 a mixture of beam particles was observed, the distribution is a combination of two Landau curves and thus broader than the curve for the M2 beam. The width of the curve, characterized by λ in (3.4), of course also depends on the particle velocity, $\lambda \propto 1/\xi \propto \beta^2$. The forms of the two distributions look similar; the maximum of the Landau curve for 160 MeV muons is 33% higher than that for a 3.6 GeV pion/proton beam.

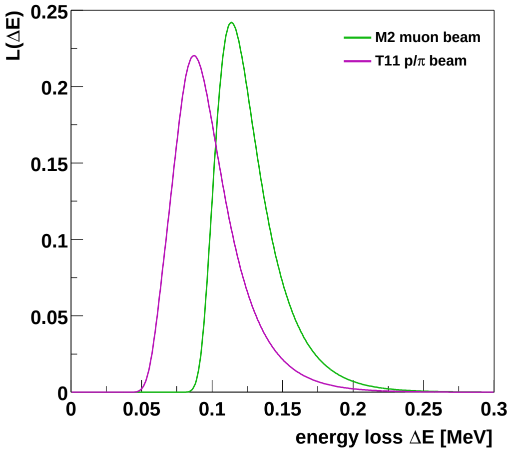

Figure 7.5: Expected Landau distributions for a 3.6 GeV beam composed of protons and pions (T11 test beam) and a 160 GeV muon beam (M2 beam-line)

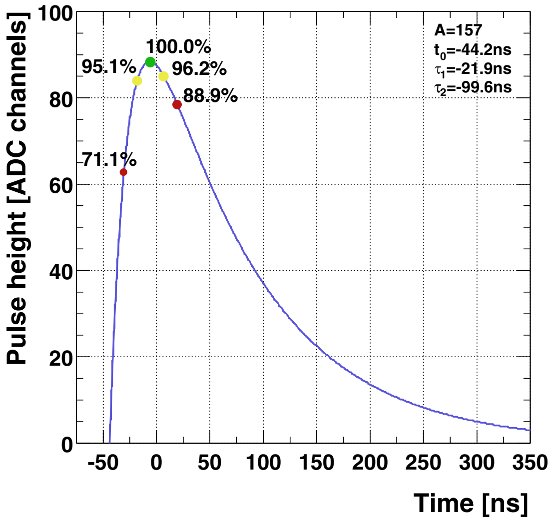

Figure 7.6: Response of the APV chip to a δ-shaped charge pulse. The relative signal height for samples taken $\pm 12.5\,\mathrm{ns}$ off and $\pm 25\,\mathrm{ns}$ off the peak are shown.

	ΔE_{mean}	e-h pairs	ΔE_{mp}	e-h pairs
3.6 GeV protons	116 keV	$3.2 \cdot 10^4$	78 keV	$2.1 \cdot 10^4$
3.6 GeV pions	136 keV	$3.72 \cdot 10^4$	92 keV	$2.47 \cdot 10^4$
160 GeV muons	169 keV	$4.66 \cdot 10^4$	113 keV	$3.04 \cdot 10^4$

Table 7.1: Mean energy loss and most probable energy loss for 3.6 GeV protons, 3.6 GeV pions and 160 GeV muons in 300 $\mu\mathrm{m}$ Silicon. The most probable energy loss is equal to the maximum of the Landau distribution.

Comparison with the T11 data. Although the T11 signal is broader due to the fact that different particles contribute to the signal, it is questionable whether a difference in signal form can be seen in Silicon data. Since the arrival of the trigger differs from the exact peak of the time evolution of the signal by up to 25 ns (cf. section 4.3.1), the observed signal amplitude distribution will be a superposition of the Landau distributions of signals within this 25 ns window.

The height of the single Landau distributions is determined by the time evolution of the APV response to the Silicon signal. Fig. 7.6 shows the relative signal heights ± 12.5 ns and ± 25 ns away from the signal peak are indicated. Due to this superposition, the signal amplitude distribution will be broadened, blurring the differences between the T11 and M2 signal forms.

The time of the single events is equally distributed over the 25 ns window given by the jitter of the trigger arrival with respect to the particle hit (cf. section 4.3.1). Therefore, the Landau distribution corresponding to the maximum amplitude of the signal in its time evolution should always be inside the 25 ns window.

However, we have to deal with a superposition of all Landau distributions in this 25 ns window. The peak of this superposition is not necessarily equal to the most probable value of the Landau distribution corresponding to the highest amplitude of the detector signal in its time evolution. An exact analysis requires information on the timing of the single signals.

Width of the Landau distribution. In the M2 beam, different detector/readout chain configurations came into operation. While the two detectors SIL10 and SIL12 have similar properties (table 5.1), the grounding for detector SIL12 has been improved during the debugging described in section 7.2.2. In contrast to SIL12, SIL10 was grounded like the detector in the T11 test beam.

Figure 7.7 shows cluster amplitude and noise for detector SIL10 and a run obtained with the readout electronics that were already used in T11. The noise is comparable with the T11 data, as well as the width of the Landau distribution, σ_L. The same plot is shown for detector SIL12 in figure 7.8, this time with the new readout electronics, but still in latch-all readout. While the noise remains the same compared to detector SIL10, the width of the Landau distributions has considerably increased, from about $\sigma_\mathrm{L} = 5.28$ to $\sigma_\mathrm{L} = 8.65$. In sparsified readout, similar distribution widths are observed (fig. 7.8).

Up to now, the difference in the distributions' widths has not been investigated thoroughly. Whether it is due to the different groundings of the two detectors, to the different electronics versions or to other reasons is not obvious.

Peak position. Comparing the signal height for detector SIL10 with the values obtained in the T11 test beam, no increase of 33% can be observed. Instead of that, the peak positions of the Landau distributions, 53.6 ADC channels for the p-side and 55.3 ADC channels for the n-side can be compared with the value of 54.2 ADC channels obtained in the T11 beam, although the 160 GeV muons of the M2 beam clearly cannot be regarded as MIPs any more.

A reason for the fact that the amplitudes are lower than expected might be that the detector was not fully depleted. While the detector in T11 was operated 30 V and more over its full depletion voltage quoted by SINTEF, this was not possible for the detectors in M2, since the capacitors used for noise reduction could only be operated at voltages up to 100 V. Here, the detectors could be operated only 10 V over their quoted full depletion voltage.

The sparsified plots for detector SIL12 (fig. 7.9) show a higher peak position of the Landau curves than the latch-all plots (fig. 7.8). Because the two sets of plots were taken with the same electronics and the same particle beam, in principle the amount of charge created by detected particles should be the same.

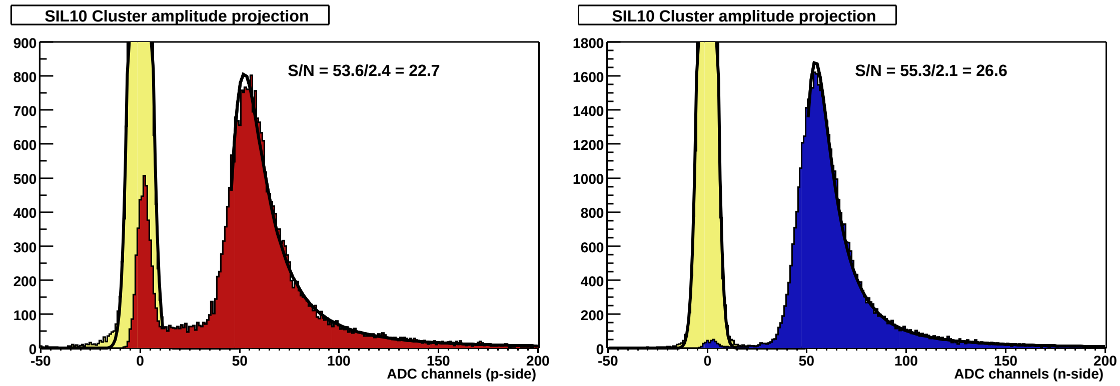

Figure 7.7: Cluster amplitude and strip noise distribution for detector SIL10 with old electronics in latch-all readout. Left: p-side, right: n-side.

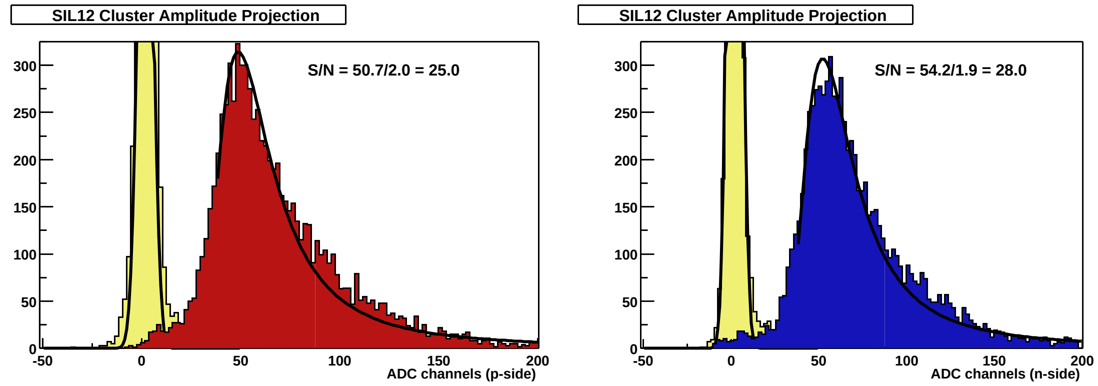

Figure 7.8: Cluster amplitude and strip noise distribution for detector SIL12 in latch-all mode with new electronics in latch-all mode. Left: p-side, right: n-side.

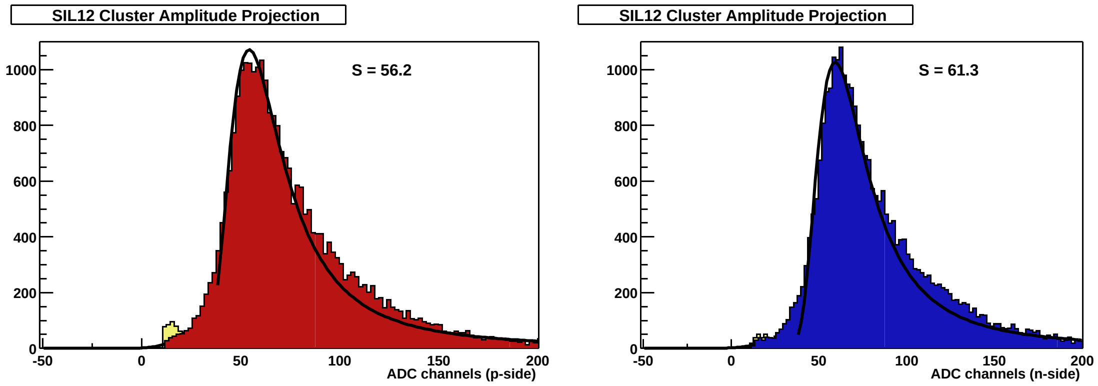

Figure 7.9: Cluster amplitude for detector SIL12 with new electronics in sparsified mode. Left: p-side, right: n-side.

The difference in signal amplitude is an important issue, since when going from latch-all to sparse mode, the ADC performs data reduction, which means that data is irrevocably lost. It is crucial to fully understand how differences between the two readout modes can happen.

7.3.2 Cluster size

While the cluster FWHM for the M2 beam is about the same as observed in the T11 beam, the cluster size (fig. 7.10) is 13% bigger for both detector sides, yielding 1.92 for the p-side and 1.66 for the p-side. Like in the T11 beam, the p-side shows larger clusters.

The detectors SIL10 and SIL12, which were studied in the M2 beam, have a considerably higher full depletion voltage of over 80 V compared to the detector used in T11 with 26 V. The assumption that SIL6 was operated overbiasedly could explain the increased cluster size observed in M2.

7.3.3 Cluster charge correlation

In figure 7.11, the cluster charge ratio for a latch-all run is shown. For this run, with a mean value of 0.974, both sides nearly see the same charge. It has to be mentioned, however, that for different runs the cluster charge ratio varies from 0.92 to 0.98. The width of the charge correlation (fig. 7.12) has slightly increased compared to the T11 beam. It remains constant for different runs.

7.3.4 Geometrical properties

Figure 7.13 shows two hit maps taken in the high-intensity muon beam, one with latch-all readout, the other with sparsified readout. The hit maps are accompanied by cluster charge projections on the two detector sides. For comparison, in the upper plot the charge projections were calculated using the center of gravity method where applicable, while in the lower hit map, the projection plots were obtained using the strip number of the cluster center only.

The spikes in the projections originate from strips excluded from readout, e. g. the shortcut strips 462 and 463 on the p-side of SIL12. For the muon beam, we can translate the r. m. s. values to a r. m. s. of 10.6 mm for the horizontal plane and 7.43 mm for the vertical plane. The structures, especially the “bump” in the horizontal plane of the lower plot, are due to misalignment in the beam optics,

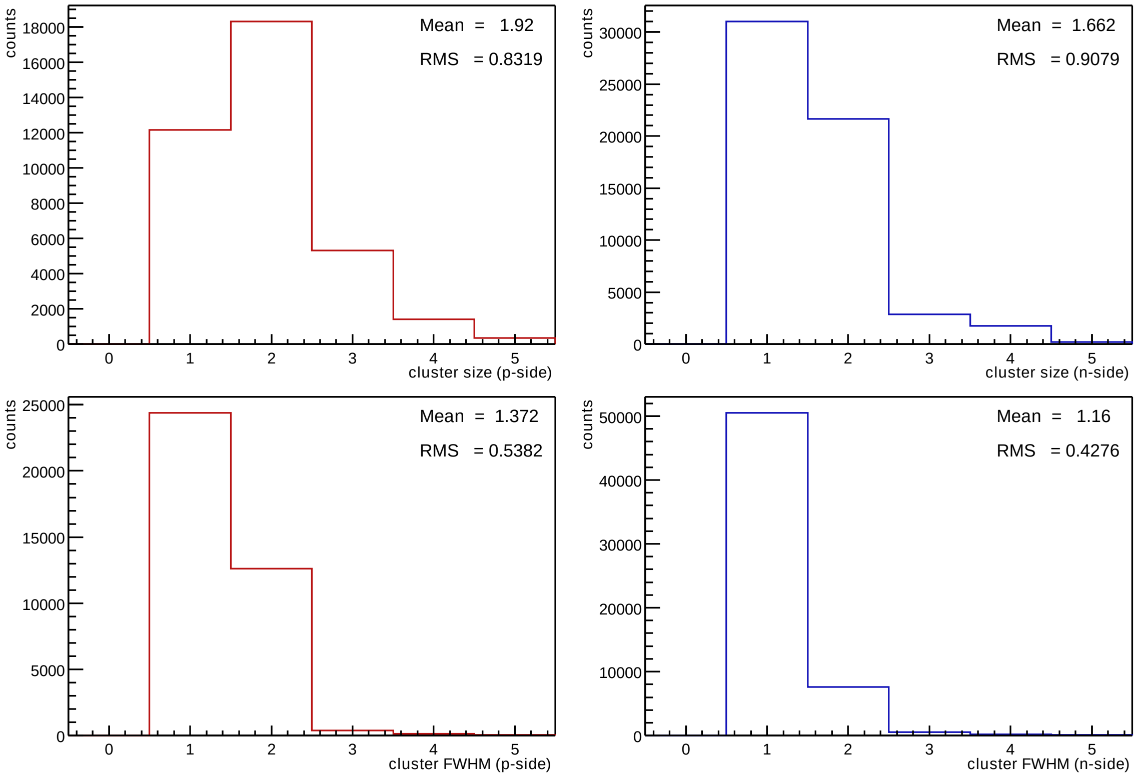

Figure 7.10: Cluster width and FWHM for detector SIL10

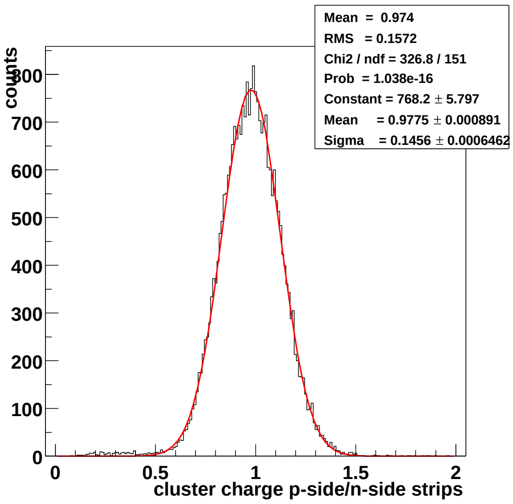

Figure 7.11: Cluster charge ratio

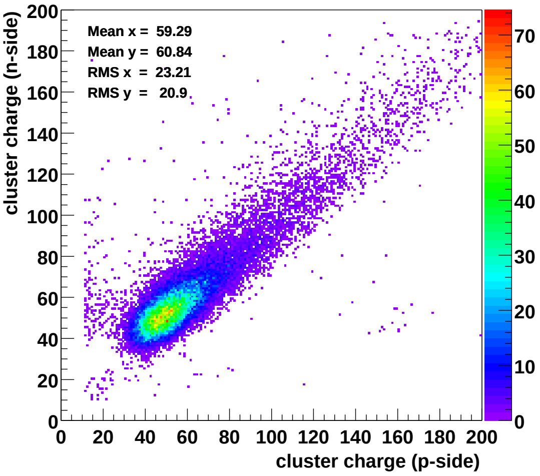

Figure 7.12: Cluster charge correlation

which occurred after beam realignment. They are not observed in the upper hit map, which was taken some weeks before.

7.3.5 Signal timing

A key problem of the T11 data were the very poor speed plots (sect. 6.3.4), which did not look promising with respect to determining signal form and signal timing. Corresponding plots for the M2 beam time are shown in figure 7.14. These plots were obtained for two consecutive trigger delays of 2050 ns and 2075 ns. The events are confined to a thin curve in the plane, which is given by the signal form. The thinner the curve, the smaller variation in the signal form. Since the structure is not blurred like the plots from T11, a deduction of the signal timing should be possible from these plots.

The curve itself is dominated by on-time hits in the 25 ns time window in which triggers arrive with respect to the real particle hit. There are no contributions from off-time events, which is due to the fact that only a low intensity beam was used ($5 \cdot 10^5$ particles per spill).

For the events in the left curve, most of the events see no signal in the first sample a_0. Shifting the trigger delay forward 25 ns allows to see signal in all three samples, while still sitting on the rising edge of the signal ($a_1 \approx a_2$, $a_0 < a_2$). Since the signal should rise faster than it decays, looking at the rising edge is most promising for determining the signal timing. An analysis regarding the signal timing based on these plots remains to be done.

High-intensity. For high-intensity runs, there is a clear necessity to separate real hits from pileup in the detector by a timing cut. In contrast to the plots shown in the last paragraph, figure 7.15 shows speed plots for p and n-side of detector SIL12 in a high-intensity beam. Since there is considerably more than one hit per event in the detector, hits cannot only be found in a 25 ns window on the curve in the speed plot plane, but populate the whole curve. This is due the presence of pileup in the detector. Measurements and an estimation of the number of strips read out for each event is given in section 7.4.

The two plots obtained were taken in sparsified readout. This means cuts on which strips to take into account are already applied by the ADC card. The pedestal correction algorithm implemented in the ADC e. g. doesn't return amplitudes $a_i < 0$, so that there are no entries with $a_0/a_2 < 0$ in the speed plot.

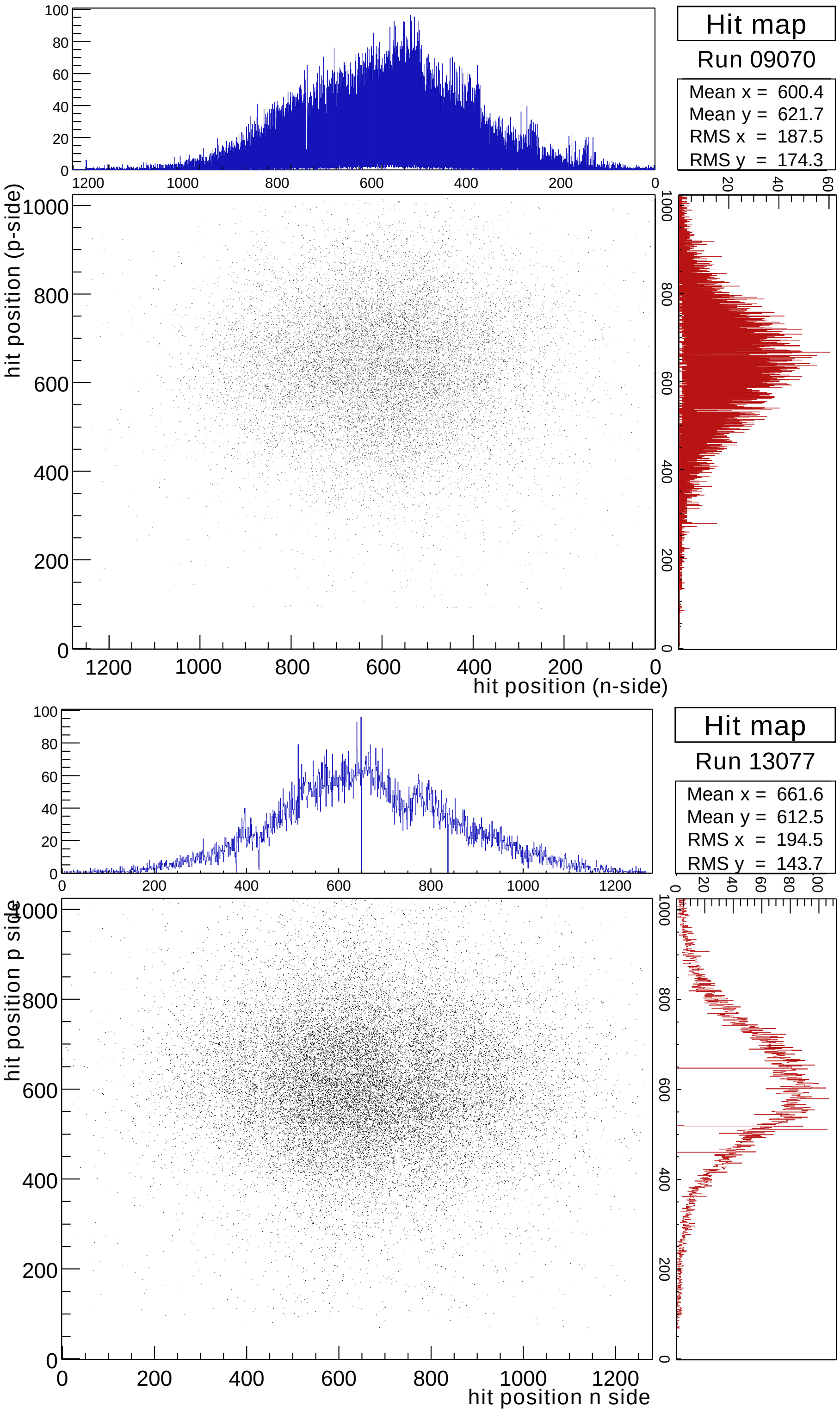

Figure 7.13: Hit maps for two runs in the muon beam. Top: detector SIL10 in latch-all mode, bottom: detector SIL12 in sparse mode. The hit maps are accompanied by cluster charge projections on the two detector sides. The spikes in the projections are connected to strips excluded from readout. As the detectors are mounted back-to-back in one cryostat, the horizontal axes of the detectors are swapped with respect to each other.

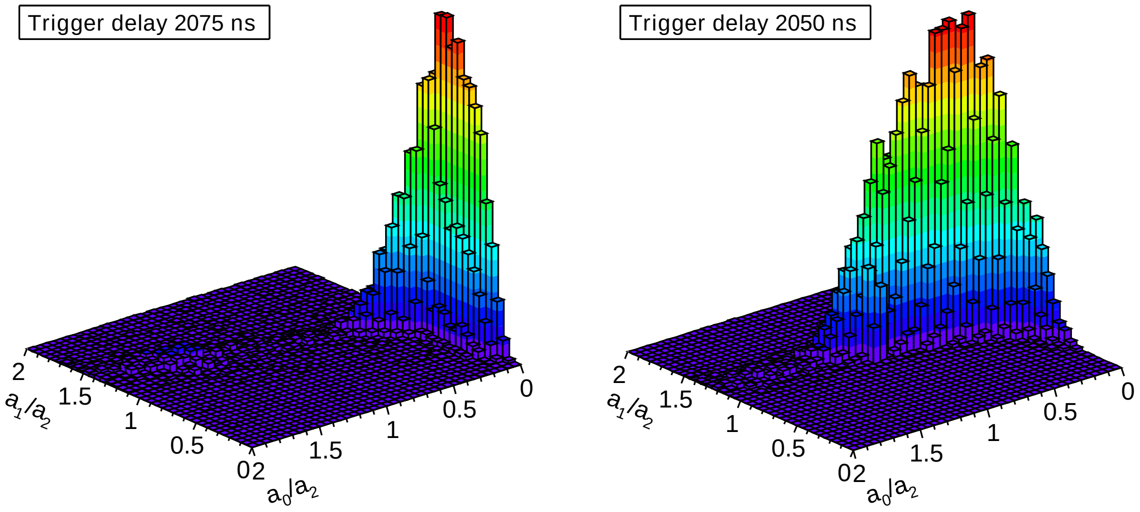

Figure 7.14: Speed plots taken with the M2 beam. The trigger delays used in the two plots differ by 25 ns, so that the events in the right plot lie more up the curve, since they arrive later. In the right plot, the first sample a_0 starts seeing the signal.

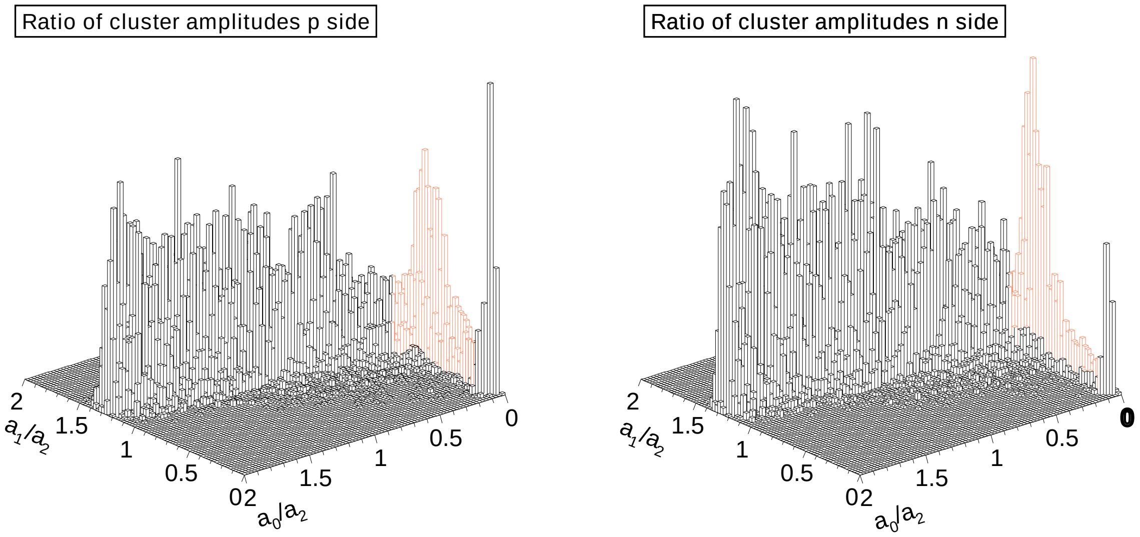

Figure 7.15: Speed plots for detector SIL12 in a high-intensity beam. Left: p-side, right: n-side. The range in which on-time events can be expected has been marked in both plots. The off-time events are not confined to the 25 ns acceptance window of the trigger arrival, but are spread over the whole curve. The plots were obtained with 99 V bias voltage applied.

7.4 Sparsified readout

In sparsified readout, the ADC is performing pedestal subtraction and common mode correction to reduce the amount of data that has to be processed by the data acquisition. Individual signal thresholds for each channel can be specified, so that the respective channel is only processed if the signal exceeds this threshold. Hence, the amount of data which is sent through the readout chain is reduced sufficiently. Thus, the trigger rate can be increased. In the 2001 run, trigger rates of up to 20 kHz have been reached.

Occupancy. The probability that a certain channel of a detector is hit by at least one particle is its *occupancy*. This definition is also applicable for the readout electronics, where occupancy is the probability that a certain channel has to be read out.

The occupancy plots are primarily important for determining the load on the readout chain. Stable data acquisition was possible with all three threshold settings. To see as many hits as possible with multi-strip clusters, the threshold has to be chosen as low as possible.

For the M2 high-intensity beam, the histograms in fig. 7.16 show the number of hit strips per event for the two detector sides. An exponential fit has been applied to the histograms. The histograms were created with different thresholds, requiring strip signals to be at least 7 times, 5 times and 3 times over the individual strip noise σ. Since for a central hit of a readout strip the charge seen by the neighboring channels is rather small, we expect the number of hit strips depending on the threshold chosen.

The cluster noise for the p-side with $\sigma = 2.1$ is bigger than for the n-side with $\sigma = 1.9$ (cf. fig. 7.8). Therefore, the absolute threshold set on the p-side is larger. This results in a larger number of strips above threshold on the n-side, despite the bigger cluster size on the p-side.

The plots show how the number of hit strips decreases with the threshold applied. At a threshold of 3σ nearly all strips hit ought to be read out. With a high cut like 7σ, readout ought to be restricted to the central strips of the hit clusters, since the strips adjacent to the central strip will in most cases not contain enough charge to be over threshold.

With a beam intensity of $2 \cdot 10^8$ particles per spill (4 sec), we expect 1.25 hits per event. Taking into account the respective cluster sizes (cf. sect. 7.3.2), this equals 2.4 strips on the p-side and 2.08 strips on the n-side. With a 3σ cut, noise should contribute with 3.1 strips on the p-side and 3.8 strips on the n-side on average.

Assuming that strips that only contain noise are not read out when applying a 7σ cut, and only the central strips of the clusters are read out at this threshold, the pileup in the detector is of the order of 1.5 strips (hits) per event on the p-side and 3.5 strips (hits) per event on the n-side, which has to be removed by a cut on the signal timing.

7.5 Summary

A stably running Silicon detector in COMPASS could be achieved for the last two weeks of the 2001 run time. Due to various problems with commissioning and the availability of new electronics, not more than two detectors were in the beam at the same time. Nevertheless, improvements of the detector performance and readout stability have been achieved. Important problems, like the insufficient noise behavior with the new electronics, most probably related to the repeater boards, could be addressed and temporarily solved. Compared to the T11 data, an enhanced detector performance concerning signal timing performance could be shown.

With sparsified readout mode, the Silicon detector could be integrated in nominal COMPASS data runs, without having to use a significant dead time to limit the data rates in the readout chain. Although sparsified mode worked stably and satisfactory, some features, e. g. the differences in signal height between latch-all and sparsified readout, remain to be thoroughly understood.

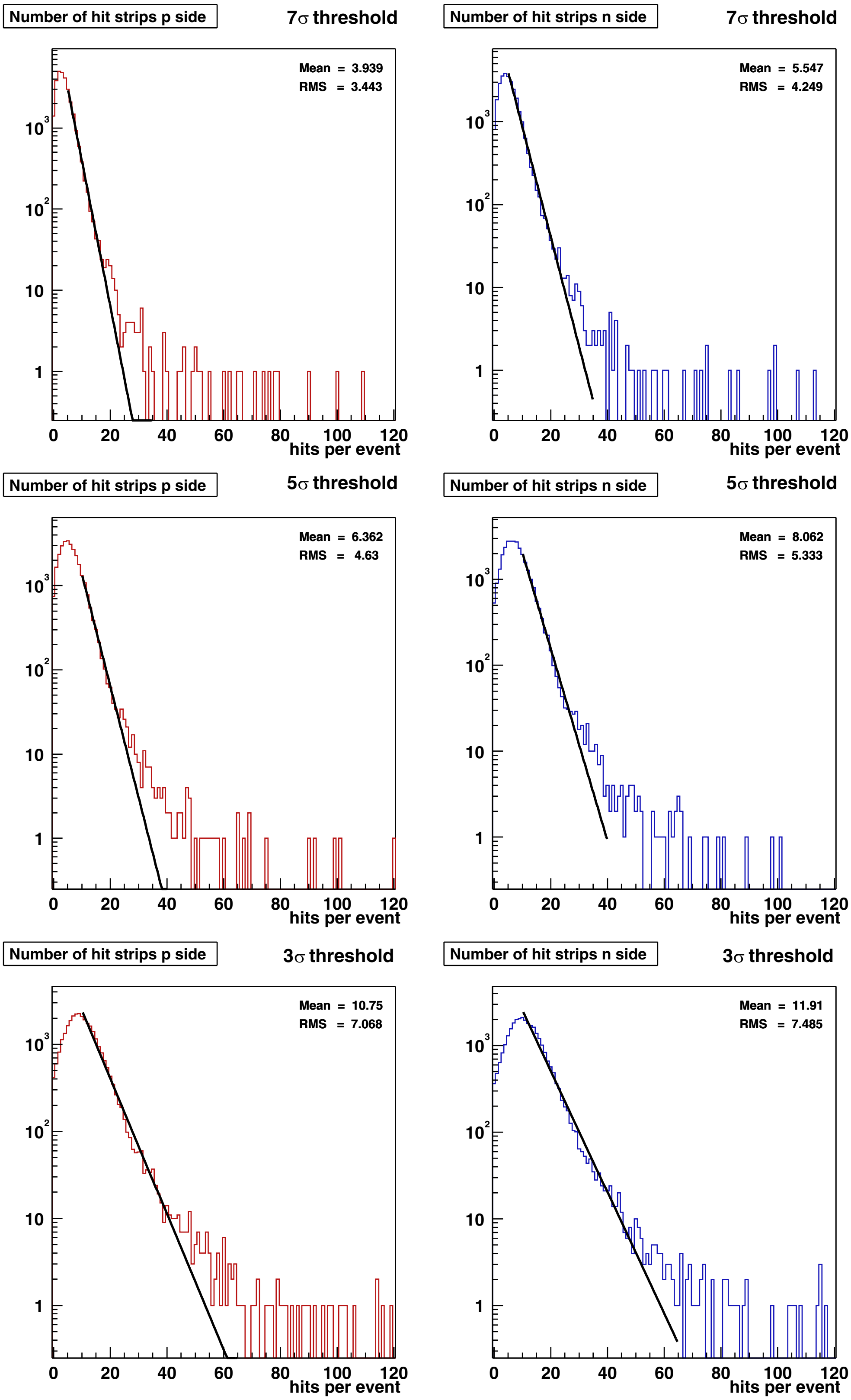

Figure 7.16: Number of hit strips per event for thresholds of 7σ, 5σ, and 3σ. Left: p-side, right: n-side. The distributions were fitted with an exponential function.

Chapter 8

Conclusions and outlook

In this thesis, the realization and production of Silicon microstrip detectors for the COMPASS experiment was described. Properties of Silicon detectors for the COMPASS experiment have been studied in the lab, in a test beam and in the COMPASS muon beam.

Different studies regarding the noise performance were done with detectors assembled for a test beam in April 2001 and for the COMPASS 2001 beam time. It was the first time a fully-equipped COMPASS Silicon detectors was assembled and read out double-sided. The tests helped to gain experience regarding the assembly procedure and the bonding of the detector to the chips. The strip noise was found to be around 820 electrons as expected, uniformly over the whole detector. Single channels showed more noise due to gluing and bonding problems, which could be solved for the future detectors. It could be shown that common mode correction algorithms, which are implemented in the ADC, have to be modified for certain readout chips due to geometrical properties of the Silicon wafer used.

In the test beam in April, for the first time this detector could be operated with the full Silicon readout chain. Reasonable signal/noise ratios of 48.71/2.06 and 54.19/1.87 for the two detector sides were observed. However, the p and n-side unexpectedly showed differences in charge collection and cluster size. With 1.48 strips, the cluster size on the n-side was found to be smaller than on the n-side with 1.69 strips, owing to the missing intermediate strips for charge division on the n side.

Plots suited for determining the time evolution of the detector signal have been studied, since the signal timing is to be deduced from three amplitude samples of the signal. The test beam results showed insufficiencies in this respect. Offline analyses have shown that signal loss due to the delay of the digitization time is responsible for that. During the COMPASS beam time, studies on the signal timing were repeated, resulting in a more promising performance.

The next step for analysis is finding an algorithm which yields the signal timing and time resolution of the detectors from the three samples taken of the detector signal. Parameters that remain to be determined are the spatial resolution and the local efficiency of the detectors.

In the COMPASS 2001 beam time, 3 new Silicon detectors connected to new readout electronics, could been commissioned. They showed an increased noise performance compared to the detector assembled for the test beam. Problems with common mode noise introduced by the new electronics could be solved, so that stable data taking with sparsified readout was achieved. The signal for the M2 beam was not as high as expected, which can be explained with the fact that the detectors might not have been fully depleted. First results from runs with sparsified readout show that stable data taking is possible down to a threshold of 3σ for the individual strips. One of the detectors could be included in the regular COMPASS data acquisition and participated in the regular COMPASS data taking.

The detector tests in the 2001 beam time revealed no major bugs in the detector hardware and the readout electronics. The problems concerning the noise pickup with the new electronics have been attributed to the repeater boards and are looked into.

While in 2001 first steps towards cooled Silicon detectors were taken with mounting cooling tubes, cooling to cryogenic temperatures has to be tested and fully implemented. Based on the experience gained in the 2001 beam time, 5 more detectors have to be assembled, so that four complete target stations can be commissioned for the 2002 run.

Bibliography

[Abt95] I. Abt et al. First results from a radiation test of a 1.2×1.2 cm^2 prototype Silicon detector with a special guard ring structure, `http://wwwhera-b.mppmu.mpg.de/publications.html`.

[Abt96] I. Abt et al. Irradiation tests of double-sided Silicon strip detectors with a special guard ring structure. *IEEE Trans. Nucl. Sci* **43**, 1113–1118 (1996).

[Abt97] I. Abt et al. Gluing Silicon with Silicone. **97-20** (1997).

[Abt99] I. Abt et al. Double sided microstrip detectors for the high radiation environment in the HERA-B experiment. *MPI-PhE* **99-05** (1999).

[Ada97] D. Adams et al. Spin structure functions of the proton from polarized inclusive deep inelastic muon-proton scattering. *Phys. Rev.* **D 56**, 5330–5358 (1997).

[Adi93] M. Adinolfi. A microstrip decay detector for beauty physics. *Nucl. Instr. and Meth. in Phys. Res.* **A 329**, 117–124 (1993).

[Air98] A. Airapetian et al. Measurement of the proton spin structure function g_1^{p} with a pure Hydrogen target. *Phys. Rev. Lett.* **B 442**, 484 (1998).

[Air00] A. Airapetian et al. Measurement of the spin asymmetry in the photoproduction of pairs of high p(t) hadrons at HERMES. *Phys. Rev. Lett.* **84**, 2584–2588 (2000).

[Ale95] Y. Alexandrov et al. The CHEOPS letter of intent. *CERN* **SPSLC 95-22** (1995).

[Ams95] C. Amsler et al. High statistics study of $f_0(1500)$ decay into $\pi^0\pi^0$. *Phys. Lett.* **B 342**, 433–439 (1995).

[Ant96] P. L. Anthony et al. Deep inelastic scattering of polarized electrons by polarized ^{3}He and the study of the neutron spin structure. *Phys. Rev.* **D 54**, 6620 (1996).

[Ash88] J. Ashman et al. A measurement of the spin asymmetry and determination of the structure function g_1 in deep inelastic muon-proton scattering. *Phys. Lett.* **B 206**, 364 (1988).

[Bea98] L. Beattie et al. Charge collection efficiency in heavily irradiated Silicon diodes. *Nucl. Instr. and Meth. in Phys. Res.* **A 412**, 238–246 (1998).

[Bed01] Y. Bedfer, `YBedfer@CEA.FR`. Private communication, November 2001.

[Ber97] SINTEF Electronics & Cybernetics, R. W. Bernstein, T. Westgaard. Technical and test specifications for MPI HERA-B doublesided Silicon. (1997).

[Bij01] E. van der Bij. CERN S-LINK homepage, `http://hsi.web.cern.ch/HSI/s-link/`.

[Boc98a] R. K. Bock and W. Krischer. *The Data Analysis BriefBook*. Springer, 1998.

[Boc98b] R. K. Bock and A. Vasilescu. *The Particle Detector BriefBook*. Springer, 1998.

[Bor00] K. Borer et al. Charge collection efficiency of irradiated Silicon detector operated at cryogenic temperatures. *Nucl. Instr. and Meth. in Phys. Res.* **A 440**, 5–16 (2000).

[Bra98] A. Bravar, D. v. Harrach, and A. Kotzinian. Gluon polarization from correlated high p_t hadron pairs in polarized electroproduction. *Phys. Lett.* **B 421**, 349–359 (1998).

[Bra99] F. Bradamante. The gluon contribution the the nucleon spin and the COMPASS experiment at CERN. In *Proceedings of the 21st Course of the International School on Nuclear Physics*, Erice, September 1999.

[Bru01] R. Brun, F. Rademakers, et al. ROOT web page, `http://root.cern.ch/`, (2001).

[CO96] The COMPASS collaboration. A proposal for a Common Muon and Proton Apparatus for Structure and Spectroscopy. *CERN* **SPSLC 96-14** (1996).

[Dam86] C. J. S. Damerell. Vertex detectors. In *Proceedings of Advanced Study Inst. on Techniques and Concepts of High Energy Physics*, St. Croix, Virgin Islands, June 1986.

[DAT00] CERN ALICE DAQ Group. ALICE DATE user's guide. *ALICE-INT-2000-31 v.2* (2000).

[Dur93] L. Durien, D. J. Simon, et al. Secondary beams for tests in the ps east experimental area, `http://cern.web.cern.ch/CERN/Divisions/PS/Reports/PA9321/`.

[Ell88] J. Ellis, S. J. Brodsky, and M. Karliner. Chiral symmetry and the spin of the proton. *Phys. Lett.* **B 206**, 309 (1988).

[Fli99] T. Fliessbach. *Lehrbuch zur Theoretischen Physik 4. Statistische Physik*. Spektrum Akademischer Verlag, 1999.

[Fox96] H. Fox. *Aufbau und Inbetriebnahme eines Teststands für Siliziumdetektoren des HERA-B Vertexdetektors*. Diploma thesis, Universität Münster, August 1996.

[Fre93] E. Fretwurst et al. Radiation hardness of Silicon detectors for future colliders. *Nucl. Instr. and Meth. in Phys. Res.* **A 326**, 357–364 (1993).

[Fri01] J. M. Friedrich, `Jan.Friedrich@Physik.TU-Muenchen.DE`. Private communication, (2001).

[Gat00] L. Gatignon. The modifications to the M2 beam for COMPASS, `http://sl.web.cern.ch/SL/eagroup/NewM2/main.html`.

[Gat01] L. Gatignon. User guide for the M2 beam, `http://gatignon.home.cern.ch/gatignon/M2manual.html`.

[Glu88] M. Glück and E. Reya. Spin dependent parton distributions in polarized deep inelastic lepton nucleon scattering. *Z. Phys.* **C 39**, 569 (1988).

[God99] S. Godfrey and J. Napolitano. Light meson spectroscopy. *Rev. Mod. Phys.* **71**, 1411–1462 (1999).

[Gru93] C. Grupen. *Teilchendetektoren*. B. I. Wissenschaftsverlag, 1993.

[Gru01] B. Grube. *The trigger control system and the common GEM and Silicon readout for the COMPASS experiment*. Diploma thesis, TU München, December 2001.

[Hal84] G. Hall. Ionization energy losses of highly relativistic charged particles in thin Silicon layers. *Nucl. Instr. and Meth. in Phys. Res.* **220** (1984).

[Hor99] S. Horikawa et al. Time resolution of a scintillating fiber detector. *Nucl. Instr. and Meth. in Phys. Res.* **A 431**, 177–184 (1999).

[Huh93] M. Huhtinen and P. Aarino. Pion induced displacement damage in Silicon devices. *Nucl. Instr. and Meth. in Phys. Res.* **A 335**, 580 (1993).

[Jon99] L. L. Jones et al. The APV25 deep submicron readout chip for CMS detectors. *CERN* **99-09** (1999).

[Jon00] L. L. Jones. APV25-S0 user guide version 2.1, `http://www.te.rl.ac.uk/med/`.

[Kem80] J. Kemmer. Fabrication of low noise Silicon radiation detectors by the planar process. *Nucl. Instr. and Meth. in Phys. Res.* **169**, 499 (1980).

[Kem88] J. Kemmer and G. Lutz. New structures for position sensitive semiconductor detectors. *Nucl. Instr. and Meth. in Phys. Res.* **A 273**, 588–598 (1988).

[Ket01] B. Ketzer. `gemMonitor`, Online analysis tool for GEM and Silicon detectors. (2001).

[Kle86] K. Kleinknecht. *Detectors for Particle Physics*. Cambridge University Press, 1986.

[Kuh01] R. Kuhn. *Simulations for the Measurement of the Polarizabilities of the Pion at COMPASS*. Diploma thesis, TU München, November 2001.

[Leo87] W. R. Leo. *Techniques for Nuclear and Particle Physics Experiments*. Springer, 1987.

[Mat80] J. L. Matthews, D. J. S. Findlay, and R. O. Owens. Distribution of electron energy losses. *Nucl. Instr. and Meth. in Phys. Res.* **180**, 573 (1980).

[MED] Microelectronics design group web page, `http://www.te.rl.ac.uk/med/`.

[Mey98] C. A. Meyer. An experimental overview of meson spectroscopy data. *Hall D Note* **12** (1998).

[Nap95] E. Nappi et al. The HMC letter of intent. *CERN* **SPSLC 95-27** (1995).

[Nie00] M. Niebuhr. *Entwicklung eines 250 MHz-Zählers mit totzeitfreier Auslese für das COMPASS-Experiment*. Diploma thesis, Universität Freiburg, November 2000.

[Pal98] V. Palmieri et al. Evidence for charge collection efficiency recovery in heavily irradiated Silicon detectors operated at cryogenic temperatures. *Nucl. Instr. and Meth. in Phys. Res.* **A 413**, 475–478 (1998).

[PDG00] D. E. Groom et al. Review of particle physics. *European Physical Journal C* **15**, 1–878 (2000).

[Pei92] A. Peisert. Silicon microstrip detectors. *Adv. Ser. Direct. High Energy Phys.* **9**, 1–79 (1992).

[Per01] H. Pereira da Costa. Saclay drift chambers, `http://h.home.cern.ch/h/hpereira/www/`.

[Ray00] M. Raymond et al. The CMS tracker APV25 0.25 μm CMOS readout chip. In *6th Workshop on Electronic for LHC Experiments*, Cracow, Poland, September 2000.

[Ric95] J. D. Richman and P. R. Burchat. Leptonic and semileptonic decays of charm and bottom hadrons. *Rev. Mod. Phys.* **67**, 893–976 (1995).

[Rie94] K. Riechmann. *Strahlenschäden durch Protonen und Pionen an Halbleiter-Detektoren*. Diploma thesis, Universität Heidelberg, September 1994.

[San99] M. Sans and U. Wiedner. Test beam results of 2 prototypes of straw tube chambers for COMPASS. *COMPASS Note* **1999-2** (1999).

[Sau77] F. Sauli. Principles of operation of multiwire proportional and drift chambers. *CERN* **77-09** (1977).

[Sch99] L. Schmitt. Hadron physics in the COMPASS experiment. In *Proceedings of the XXXVII International Winter Meeting on Nuclear Physics*, Bormio, (1999).

[Sch00] L. Schmitt. The COMPASS experiment: Charm physics with muon and hadron beams. Talk given at *Heavy Quarks at Fixed Target*, Rio de Janeiro, (2000).

[Sim01] F. Simon. *Commissioning of the GEM Detectors in the COMPASS Experiment*. Diploma thesis, TU München, November 2001.

[Sot94] S. Sotthibandhu. *Radiation Damage Studies of Silicon Detectors*. Ph. D. thesis, Imperial College London, (1994).

[Ste84] R. M. Sternheimer, M. J. Berger, and S. M. Seltzer. The density effect for the ionization loss of charged particles in various substances. *Atomic Data and Nucl. Data Tables* **30**, 262 (1984).

[The01] D. Thérs et al. Micromegas as a large microstrip detector for the COMPASS experiment. *Nucl. Instr. and Meth. in Phys. Res.* **A 469**, 113–146 (2001).

[Tho01] A. W. Thomas and W. Weise. *The Structure of the Nucleon*. Wiley-VCH, 2001.

[Wie00] M. Wiesmann. Status report: Beamtime in M2, September 2000. Talk given at *COMPASS Collaboration Meeting*, Genéve, (2000).

[Zie01] R. Ziegler, `Ziegler@ISKP.Uni-Bonn.DE`. Private communication, December 2001.

Own contributions

This thesis has been done within the framework of the chair of Prof. Paul at Technische Universität München and at CERN, Genève.

For laboratory tests of the silicon detectors, I developed a VME readout software for sg_adc and GeSiCA, which is able to generate the relevant histograms for quality control.

I developed loading software for the electronic equipment common to GEM and Silicon detectors. These programs were used at the test beam in April/May and during the COMPASS beam time in Summer 2001. I adapted the software to the needs, especially for debugging and for support of the sparsified readout.

I did analysis of the T11 test beam data. This included the noise studies presented. which were done for all detectors mentioned. For the analysis of the beam data, I used the existing environment for analysis, `gemMonitor`, and modified it where necessary; for further analyses, I developed ROOT scripts which made use of the tree generated by `gemMonitor`. The timing performance of the detector was found to be insufficient, so I had to do further studies regarding this issue, leading to the result that the ADC delay was set incorrectly during the test beam. Several other starting points for modifications were found during analysis and pursued.

During the COMPASS beam time, I was involved in commissioning, debugging and running the Silicon detectors. Commissioning included setup and hardware installations as well as cabling in the target region. In the first runs we found the noise performance to be very bad, especially with the new electronics. After systematic tests, we could trace back the poor performance to the new repeater cards.

I did a first analysis of the detector data of the M2 beam time, to ensure the increased timing, noise and overall performance of the detector in contrast to the T11 results and to get a first impression of the performance in sparsified readout.

Acknowledgements

I thank my boss Prof. Stephan Paul for allowing me to spend one year with COMPASS to work on Silicon detectors and to learn how much work is necessary and how many details have to be considered to operate small particle detectors like Silicon microstrip detectors and to get a big experiment running.

Of course I'm also much obliged to my supervisor Michael Wiesmann for helping me getting into the subject and for his co-operation wherever possible. Over the months I felt more and more at home in the Silicon business. Thanks also to Rita de Masi and our technical students who made work more easy during the 2001 run at CERN, especially at times when nothing seemed to work at all.

But not only the Silicon crew, also E18 in general deserves acknowledgement: Igor Konorov for his patience and constant support. Roland Kuhn for being a likeable office-mate, for many discussions, and for his very valuable hint to start making cables in case you really are fed up with `C++`. I am also indebted to Boris Grube for the discussions in the final phase of this thesis. You all made life quite nice at E18. A special thanks to Lars Schmitt, Jörn Kersten and Jan Friedrich for proof-reading this manuscript.

Ciao Franco—I appreciate discussions with Frank Simon and him being kind of contact person whenever I was at CERN. Thanks to Bernhard Ketzer for also being a outpost there, whom we all too often asked for support. Thanks also to all COMPASS members, who made the weeks of the 2001 runs and the time at CERN quite a nice time, despite all the days and nights without much sleep.

I also want to mention Rudolf K. Bock, who more than promptly sent me copies of his two BriefBooks, which proved to be very helpful.

I thank the State of Bavaria for the financial support—Stipendium für besonders Begabte—throughout my studies.

Last, but of course not least, I want to thank my girl-friend Nina Nowak for her patience throughout the last year, for her motivation and support, and of course my parents, not only because they made my studies possible, but moreover for every support throughout the last 26 years.